

RUPRECHT-KARLS-UNIVERSITÄT HEIDELBERG



Philipp Chung-On Ranitzsch

Low Temperature Calorimeter with
Superconducting Particle Absorbers

Diploma Thesis

HD-KIP 09-39

KIRCHHOFF-INSTITUT FÜR PHYSIK

Faculty of Physics and Astronomy
University of Heidelberg

DIPLOMA THESIS

in Physics

submitted by

Philipp Chung-On Ranitzsch

born in Karlsruhe

2009

**Low Temperature Calorimeters
with Superconducting
Particle Absorbers**

This diploma thesis has been carried out by
Philipp Chung-On Ranitzsch
at the Kirchhoff Institute for Physics
under the supervision of
Professor Christian Enss

The small specific heat of superconducting materials at temperatures far below T_c makes them very attractive as particle absorbers of high-resolution low temperature micro-calorimeters. However, so far the successful use of superconductors for this application has been prevented by the complex thermalisation behaviour in the down conversion of the absorbed energy to thermal excitations.

In this work the thermalisation behaviour in two different superconductors was investigated experimentally. Two particle detectors based on the concept of metallic magnetic calorimeters were fabricated, one with an absorber made of high purity aluminium, the other one with an absorber made of Al:Mn_{2000 ppm}. Metallic magnetic calorimeters are low temperature detectors operated below 100 mK using a paramagnetic material in a small magnetic field as temperature sensor. A particle absorption heats up absorber and sensor and causes a change of magnetisation which is read out as magnetic flux change in a low-noise SQUID magnetometer.

The thermalisation behaviour was characterised at different operating temperatures and magnetic fields. The observed signal shapes suggest that Mn ions slow down the diffusion of heat in the absorber material. The very astonishing, previously observed effect, that at very low temperatures not all of the deposited energy seems to contribute in form of heat to the signal was also found for the detector with pure Al absorber. Instead, the detector with Al:Mn absorber, did not share this effect.

Further, the data analysis of the detector with Al:Mn absorber lead to the idea for a new type of sensor for low temperature calorimeters using a partially quenched superconductor in an inhomogeneous magnetic field. A detector prototype using hafnium as such a temperature sensor was developed, analysed and described in a first theoretical model.

Tieftemperaturkalorimeter mit supraleitendem Teilchenabsorber

Durch die geringe spezifische Wärme von supraleitenden Materialien bei Temperaturen weit unter der Sprungtemperatur T_c wären diese sehr geeignet für Teilchenabsorber für hochauflösende Tieftemperatur-Mikrokalorimeter. Ein erfolgreicher Einsatz eines Supraleiters für diesen Zweck wurde bisher jedoch durch das komplizierte Thermalisierungsverhalten der deponierter Energie verhindert.

In dieser Arbeit wurde das Thermalisierungsverhalten von zwei unterschiedlichen supraleitenden Materialien experimentell untersucht. Zwei Metallische magnetische Kalorimeter wurden aufgebaut. Eines mit einem Absorber aus hochreinem Aluminium, der andere mit einem Absorber hergestellt aus Al : Mn_{2000 ppm}. Metallische magnetische Kalorimeter sind Tieftemperaturdetektoren, die bei Temperaturen unter 100 mK betrieben werden und ein paramagnetisches Material in einem schwachen magnetischen Feld als Temperatursensor benutzen. Eine Teilchenabsorption erwärmt Absorber und Sensor und bewirkt eine Änderung der Magnetisierung die als magnetischer Flussänderung von einem rauscharmen SQUID Magnetometer ausgelesen wird.

Es wurden Charakterisierungsmessungen an beiden Detektoren durchgeführt. Die Datenanalyse des Detektors mit einem Absorber aus Al:Mn führte zu der Idee eines neuartigen Temperatursensor für Tieftemperaturkalorimeter. Dabei wird ein teilweise gequenchter Supraleiter in einem inhomogenen Magnetfeld genutzt. Ein Detektorprototyp mit Hafnium als ein solcher Temperatursensor wurde entwickelt, analysiert und in einem ersten theoretischen Modell beschrieben.

Contents

1	Introduction	1
2	Theoretical Background	3
2.1	Principles of Low Temperature Calorimeters	3
2.1.1	Principles of Metallic Magnetic Calorimeters	3
2.2	Sensor Material <u>Au:Er</u>	4
2.2.1	Basic Properties of <u>Au:Er</u>	4
2.2.2	Heat Capacity and Magnetisation	5
2.2.3	Detector Signal	7
2.2.4	Influence of Nuclear Spins	9
2.3	Superconductors	10
2.3.1	Basic Properties	10
2.3.2	Specific Heat	11
2.3.3	Critical Field	12
2.3.4	Energy Absorption and Down Conversion in a Superconductor	12
2.3.5	Importance of superconducting absorber materials	15
2.3.6	Previous Experiments	15
2.4	Detector Geometry	17
2.4.1	MMCs with meander-shaped pickup coil	18
2.4.2	Magnetic Field Distribution	19
2.5	Fundamental Limits on the Energy Resolution	20
2.5.1	Detector Response	21
2.5.2	Intrinsic Noise Contributions	22
2.5.3	Signal-to-Noise Ratio and Energy Resolution	26
3	Experimental Methods	29
3.1	Cryogenics	29

3.2	Superconducting Magnetometer	30
3.2.1	dc-SQUID	31
3.2.2	Two-stage Configuration	32
3.2.3	Readout Noise	34
3.3	Calibration ^{55}Fe Source	35
3.4	Detector Design	35
3.4.1	Meander with Integrated dc-SQUID	35
3.4.2	Detector Setup	37
3.4.3	Arrangement of the Wiring	38
3.4.4	Thermometry and Data Acquisition	39
4	Metallic Magnetic Calorimeters: Experimental Results	41
4.1	Magnetic Flux Noise at Low Temperatures	41
4.2	Magnetisation Measurements	43
4.3	Spectrum	44
4.4	Energy Resolution	46
4.5	$50\ \mu\text{m}$ Al detector	49
4.5.1	Signal Shape	49
4.5.2	Signal height and heat capacity	52
4.5.3	Thermal conductance to the bath	54
4.6	$50\ \mu\text{m}$ Al:Mn detector	56
4.6.1	Signal Shape	56
4.6.2	Pulse Heights	59
4.6.3	Pulses at High Temperatures	61
5	New Sensor Design	63
5.1	Principle of Magnetic Transition Edge Sensors	63
5.2	Superconductors suitable for the New Sensor Concept: The Case of Hafnium	64
5.3	Prototype Setup	64
5.4	Simulations for Magnetic Transition Edge Sensors	65

5.4.1	$B(H)$ relation	65
5.4.2	Flux change	66
5.4.3	Heat Capacity	68
5.4.4	Detector Signal	69
5.5	Experimental Results	70
5.5.1	Magnetic Flux Noise at Low Temperatures	70
5.5.2	Magnetic Flux Change	71
5.5.3	Signal Height and Heat Capacity	73
5.5.4	Signal Shape and Thermal Link	74
5.5.5	Energy resolution	76
6	Summary and Outlook	77
	Bibliography	79
	Acknowledgments	85

1. Introduction

Calorimeters (lat. calor = heat, warmth; metere = measuring) make use of the fact that heat is a form of energy. The use of calorimeters as particle detectors was first proposed by Pierre Curie and Albert Laborde, who recognised a slightly increased temperature in a radium sample and explained it with the radioactive decays in the sample [Cur03].

Contemporary applications reach from high-energy physics in large particle accelerators like the Large Hadron Collider (LHC) via various uses in chemistry and biology to micro-calorimeters, for the detection of single photons in the spectral range from visible light to γ -rays.

Franz Eugen Simon suggested in 1935 the use of lower temperatures to make the measurements of calorimeters more effective [Sim35]. This is because the specific heat of a material can be many orders of magnitude smaller at low temperatures than at room temperature.

Low temperature detectors have become more and more important in recent years. The development went from single detector prototypes to kilo-pixel arrays read out by various multiplexing techniques and being developed for all kinds of applications. Since these low temperature detectors are based on a calorimetric principle, it is important to minimise the heat capacity of the device. There are different ways to achieve that.

One of the first ideas was to use dielectrics as absorber material because of their low, purely phononic, specific heat. But because of the low thermal conductivity the signals become very slow, therefore lowering the achievable count rate of the detector to a non-practical value. An additional problem arises from the production of long-lived electron-hole pairs which often result in a degraded energy resolution.

In contrast to this, the thermalisation of energy in normal metals can be enormously fast even at milli Kelvin temperatures. This is also the reason why most of the presently used high resolution micro-calorimeter employ normal metal x-ray absorbers. Using normal metal absorbers works well for different energy ranges, since only the thickness, corresponding to the stopping power, needs to be adjusted. This ranges from thicknesses of a few micra for soft x-ray absorption to a few hundred micrs thick absorbers for hard x-ray or γ -ray measurements. Impressive results have been obtained with such devices. But normal metals show a comparably high specific heat, therefore limiting the lowest achievable heat capacity for a given stopping power and detection area.

A third option, and this one has been examined during this work, is the use of superconducting absorbers. Because of the forming of Cooper pairs the electronic specific heat behaves differently from that of normal metals and becomes negligible at temperatures that are far below the transition temperature. Superconducting absorbers are already widely used, mainly for high-energy applications, because the lower specific heat has a greater impact on larger absorber sizes. But there are a

number unresolved difficulties found in superconducting absorber materials.

First of all superconducting absorbers show much longer thermalisation times than comparable detectors with normal metal absorbers. This effect is thought to be related to the recombination of broken-up Cooper pairs, so-called quasiparticles. By doping superconductors with magnetic impurities the energy gap is reduced and therefore the recombination time might become faster.

Secondly, the integral over temperature pulses originating from absorbed ionising radiation compared with the integral of pulses of only thermal excitations of the same energy is different at very low temperatures. The “missing energy” in case of absorbed particles seems to be stored in some long-lived excitations, where the energy is released on long time scales, longer than several seconds.

In a previous work [Wel08] 500 μm thick absorbers made of aluminium and aluminium doped with 2000 ppm of manganese were examined. The same materials are used in this thesis but with a much smaller thickness of about 50 μm . This way two influences on the thermalisation can be investigated.

The first one is the impact on the thermalisation caused by the Mn ions in Al in comparison to the high purity Al absorber. Secondly, the effect of the small thickness of the absorber itself and the effect of a finite probability for photons to cross the absorber and to be absorbed in normal metal parts of the sensor that are underneath the absorber. This is possible for the 5.9 keV photons, which are used to characterise the detector since the absorption length is $\lambda = 32 \mu\text{m}$. Therefore, a probability of about 20 % is left for the 5.9 keV x-rays to cross the absorber and to not interact with the detector until the gold spacer layer underneath is reached.

Chapter 2 describes the theoretical background of low temperature calorimeters. The focus will be especially on metallic magnetic calorimeters (MMCs) which use a paramagnetic alloy of gold and the rare earth metal erbium in a small magnetic field as temperature sensor. In addition, some basic properties of superconductors will be summarised.

The experimental methods are presented in chapter 3, covering all necessary experimental environment to carry out the experiments. This includes cryogenics, the flux measurement devices called SQUIDs¹ and the actual detector setup used during this work.

Chapter 4 contains the experimental results obtained with the two detectors built and characterised during this work. Some of the observations during the analysis of the data led to the idea for the development of a new micro-calorimeter with a new type of sensor using a partially quenched superconductor in an inhomogeneous magnetic field.

This new sensor is described in chapter 5. This contains a theoretical description and numerical simulations, to determine the detector performance, a short description of the experimental setup and the experimental results obtained with the assembled prototype including a detailed comparison of the theoretical and the experimental results.

¹Superconducting Quantum Interference Device

2. Theoretical Background

2.1 Principles of Low Temperature Calorimeters

Calorimeters are detectors that make use of the fact that heat is a form of energy. The higher the deposited energy, the higher the temperature rise. On the other hand the heat capacity plays a major role in the development of calorimeters.

According to thermodynamics the increase of temperature ΔT is proportional to the amount of deposited energy ΔE :

$$\Delta T = \frac{\Delta E}{C_{\text{tot}}}, \quad (2.1)$$

with C_{tot} the total heat capacity of the device.

The parts used in a calorimeter are an absorber for the particles to be detected, a temperature sensor, a weak thermal conductance G between the sensor and a thermal bath at temperature T_0 . To record the signals a readout circuit is needed as well. The absorber is introduced because there can be geometrical restrictions to the sensor, which therefore does not meet the experimental requirements on detection area and probability to stop the measured particles, the so-called quantum efficiency. The absorber can provide the wanted detection area and the needed thickness to provide a high quantum efficiency.

The heart of a low temperature calorimeter is the temperature sensor which can be described as a solid state system in which one of the characteristic quantities is strongly dependent on temperature.

How these different parts are defined for Metallic Magnetic Calorimeters will be discussed below.

2.1.1 Principles of Metallic Magnetic Calorimeters

Metallic Magnetic Calorimeters are low temperature microcalorimeters that make use of a high sensitivity magnetic susceptibility thermometer. The identification of the right material to be used as thermal sensor is not easy since it should combine a strong dependence of the magnetisation on temperature with a low heat capacity C and a fast response.

Paramagnetic dielectrics offer comparably small heat capacity despite large spin concentration. But because the thermalisation happens through the slow spin-phonon interaction the relaxation times are rather long. Signal rise times of 40 ms and decay times in the order of 10 s were reported [Büh88], which are too long for most applications.

To overcome this obstacle metals or semimetals can be used as host materials for magnetic ions [Ban93]. Because of the electronic structure rare earths are the preferred magnetic ions in a diluted alloy in noble metals. An alloy of erbium and

gold has shown the best performance so far and is well understood in its properties.

A Metallic Magnetic Calorimeter consists of an absorber well coupled to a paramagnetic temperature sensor made of the rare earth metal erbium dissolved in gold positioned in an external magnetic field. The sensor is weakly coupled to a thermal bath and a coil is wound around the sensor to detect the magnetisation signal.

After a photon or a massive particle is stopped in the absorber the temperature of the detector increases as described by equation 2.1, where C_{tot} is the sum of the heat capacity of absorber and sensor. Due to the increase of temperature the magnetisation of the sensor changes by

$$\Delta M \simeq \frac{\partial M}{\partial T} \Delta T. \quad (2.2)$$

The pickup coil detects this change of magnetisation as a change of flux. In the end by measuring this change of flux the direct information on the absorbed energy is obtained according to the proportionality:

$$\Delta \Phi \propto \frac{\partial M}{\partial T} \frac{E}{C_{\text{tot}}}. \quad (2.3)$$

This change of flux is then coupled to a low noise dc-SQUID-magnetometer, which is a very sensitive flux-to-voltage transducer.

2.2 Sensor Material Au:Er

In the following an overview over the properties of Au:Er as temperature sensor is given. A more detailed description can for example be found in [Wel08] or [Fle03].

2.2.1 Basic Properties of Au:Er

At low concentrations erbium forms a solid solution in gold replacing gold atoms on the fcc lattice sites. The erbium yields three electrons to the free conduction electrons forming Er^{3+} ions with the electron configuration $[Kr]4d^{10}4f^{11}5s^25p^6$. The permanent magnetic moment arises from the electrons of the partially filled $4f$ shell. Figure 2.1 shows schematically an erbium ion in the gold host lattice. This illustrative sketch already suggests two advantage of the $4f$ rare earth series over the $3d$ and $4d$ transition metals. The $4f$ shell has a much smaller radius than the filled $5s$ and $5p$ shells and is therefore better shielded from the crystal field and shows smaller interaction with the conduction electrons than in the case for the $3d$ electrons of transition metals.

As the influence of the crystal field is small, the magnetic moment can be calculated according to Hund's rules. At room temperature, the paramagnetic behaviour of erbium in gold can be well described by an ensemble of these magnetic moments of free Er^{3+} ions. At lower temperatures the influence of the crystal field can not be neglected any more as it splits the sixteen fold degeneracy of the Er^{3+} ions into a series of multiplets. The lowest one is a Kramer's Γ_7 -doublet separated from the

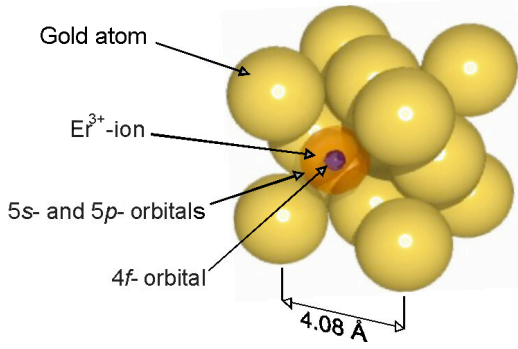


Figure 2.1 A schematic picture of a Er^{3+} ion replacing a Au^+ ion on its fcc lattice site. Noticeable are the radii of the $5s$ and $5p$ orbitals which are much larger than the radius of the $4f$ orbital. Therefore the outer orbitals shield the inner one from the crystal field.

next multiplet by an energy gap of $\Delta E \approx 17 \text{ K} \cdot k_{\text{B}}$, with the Boltzmann constant $k_{\text{B}} = 1.3806504 \cdot 10^{-23} \text{ J/K}$ [Hah92]. Since the working temperature of Metallic Magnetic Calorimeters is normally below 100 mK the next higher state will almost certainly not be excited and the erbium ions can be treated with effective spin $\tilde{S} = 1/2$ and an effective Landé factor of $\tilde{g} = 6.8$ for the ground state doublet. This theoretical value was confirmed in several ESR experiments (see i.e. [Tao71]).

2.2.2 Heat Capacity and Magnetisation

According to eq. 2.3 to describe the behaviour of an MMC it is important to know more about the heat capacity C_Z and the magnetisation M of the spin system of the sensor at temperatures below 100 mK. Under these circumstances Au:Er can be treated with an effective spin of $\tilde{S} = 1/2$ and an effective Landé factor of $\tilde{g} = 34/5$.

Let us consider the erbium ions in a gold host thermodynamically as N non-interacting magnetic moments in a homogeneous magnetic field B . This means that an energy splitting of

$$\Delta E = \tilde{g}\mu_{\text{B}}B \quad (2.4)$$

can be defined between the two spin orientations of the ground state. Starting from the thermodynamic potential, the Gibbs free energy, the well known Schottky expression for the specific heat can be derived [Ens05]:

$$C_Z = Nk_{\text{B}} \left(\frac{\Delta E}{k_{\text{B}}T} \right)^2 \frac{e^{\Delta E/k_{\text{B}}T}}{(e^{\Delta E/k_{\text{B}}T} + 1)^2}. \quad (2.5)$$

In a similar way the magnetisation can be calculated to:

$$M = \frac{N}{V} \tilde{g}\tilde{S}\mu_{\text{B}}\mathcal{B}_{\tilde{S}}(h), \quad (2.6)$$

with the volume V and the Brillouin function $\mathcal{B}_{\tilde{S}}$. For spin $\tilde{S} = 1/2$ this leads to the following expression for the magnetisation:

$$M = \frac{N}{V} \frac{1}{2} \tilde{g}\mu_{\text{B}} \tanh \left(\frac{\tilde{g}\mu_{\text{B}}B}{2k_{\text{B}}T} \right) \quad (2.7)$$

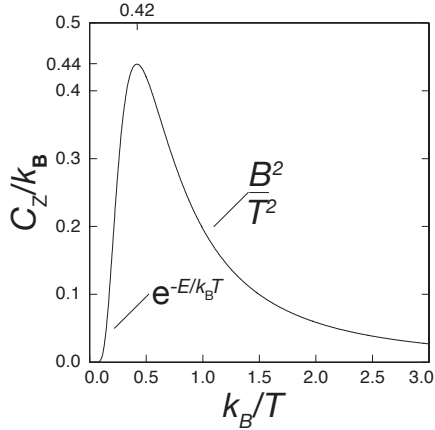


Figure 2.2 Schottky anomaly of the heat capacity for a two level system with the energy splitting $E = \tilde{g}\mu_B B$ plotted against the reduced temperature $k_B T/E$. The low and high temperature approximations are also given.

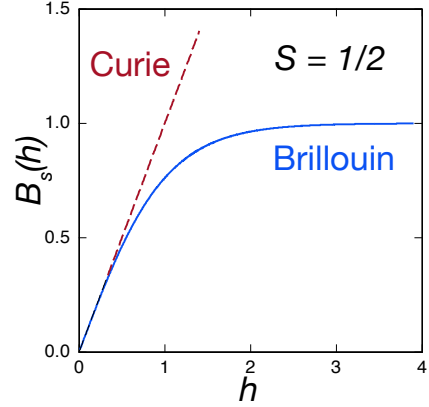


Figure 2.3 The Brillouin function $\mathcal{B}_{\tilde{S}}(h)$ showing the qualitative behaviour of the magnetisation of a non-interacting spin $\tilde{S} = 1/2$ system. Also depicted the linear Curie approximation for high temperatures.

Figure 2.2 shows the contribution of one two-level-system with energy splitting E to the heat capacity together with the approximations for high temperatures, $C_Z \sim B^2/T^2$, and for low temperatures, $C_Z \sim e^{-\Delta E/k_B T}$. The maximum of this Schottky anomaly is found at the temperature $T \approx 0.42\Delta E/k_B$. Figure 2.3 shows the theoretical behaviour of the magnetisation of a $\tilde{S} = 1/2$ system following equation 2.7. For small h (high temperature/small magnetic fields) the linear approximation of Curie's law $M = C \cdot H/T$, with the material dependent Curie constant C , can be seen, as well as the saturation behaviour $h \gg 1$ (low temperatures/large magnetic fields) of the Brillouin function.

While the thermodynamic properties in this approximation of non-interacting spins can easily be calculated and describe the behaviour of Au:Er-alloys qualitatively very well, it is not accurate enough to describe the behaviour quantitatively. To do this properly, interactions between the magnetic moments need to be considered.

First the magnetic dipole-dipole interaction is necessary and second the indirect interaction mediated by the conduction electrons named RKKY-interaction (after the contributing physicists M. A. Ruderman and C. Kittel [Rud54], T. Kasuya [Kas56] and K. Yosida [Yos57]).

To include these interactions, numerical calculations need to be implemented either using mean-field theory [Hor99] or using numerical diagonalisation of the Hamiltonian of a cluster of randomly distributed erbium ions [Sch00, Fle03].

The results for the numerical diagonalisation for a Au:Er sample with an erbium concentration of 300 ppm are shown in figure 2.4. The solid lines represent results of calculations done for different magnetic fields ranging from 0.87 mT to 12.8 mT, while the symbols depict measured data. The features mentioned earlier, like the Curie law and the saturation of the magnetisation (figure 2.4 (right) compared to figure 2.2)

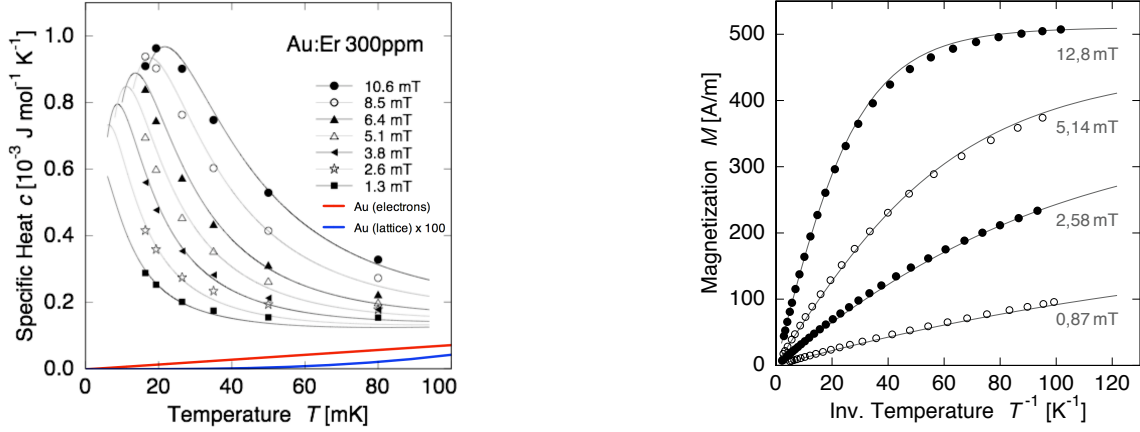


Figure 2.4 The results of the numerical calculations following [Sch00, Fle03] for a $\text{Au:Er}_{300\text{ppm}}$ sample (solid lines) in comparison with experimental data (symbols) at different magnetic fields. On the left side the specific heat of the Zeeman system is shown. At the bottom of the graphic the specific heat contributions of gold are shown for comparison. On the right the magnetisation is depicted.

and the maximum in the specific heat (figure 2.4 (left) compared to figure 2.3) can be seen.

Since the calculated curves and the measured data sets agree very well, the thermodynamic properties of the sensor material Au:Er seem to be understood and the calculated data can be used for further analysis of measured data. Furthermore, the calculated data can also be used while designing new detectors for specific applications in order to achieve optimal detector performance.

2.2.3 Detector Signal

The energy released in an MMC is read out as a change of magnetic flux Φ that is directly proportional to the change of magnetisation $\partial M/\partial T$ of the sensor (eq. 2.3). To understand the dependence of the detector signal on temperature and magnetic field, it is more instructive to consider the change of magnetic moment in the sensor, because the magnetic moment

$$\Delta m = V \Delta M \quad (2.8)$$

is independent of the detector geometry, rather than the magnetisation, since the value of the latter strongly depends on the detector size.

In the following the erbium ions are described as non-interacting magnetic moments and no other heat capacity is assumed to be present in the detector. The whole deposited energy E will be used to induce ΔN spin flips. As an energy $\Delta E = \tilde{g}\mu_B B$ is needed per spin flip, this leads to a change of magnetic moment of the sensor of

$$\Delta m = \tilde{g}\mu_B \Delta N = \tilde{g}\mu_B \frac{E}{\tilde{g}\mu_B B} = \frac{E}{B} . \quad (2.9)$$

This means the signal size is only dependent on and inverse proportional to the applied magnetic field B . The larger the magnetic field the larger is the Zeeman splitting and the more energy is needed for a spin flip. Therefore in larger fields the same amount of deposited energy can cause less spin flips, which results in a smaller signal.

But the description of an MMC only as a thermodynamic spin system does not reproduce the real behavior. To describe the signal size more realistically, the detector needs to be considered as consisting of different thermal systems with the corresponding heat capacities. The deposited energy divides up according to the relative value of each subsystem's heat capacity. These are the electronic and phononic heat capacities of both sensor and absorber. Therefore the fraction of energy going in the spin system is given by:

$$E_S = \frac{C_S}{C_S + C_e + C_{ph}} E \quad (2.10)$$

Since all heat capacities, except for the spin system, are all magnetic field independent, the properties to be looked at for a qualitative analysis are the specific heat of the magnetic moments (eq. 2.5) and the change of magnetic moment (eq. 2.9). For weak magnetic fields ($\tilde{g}\mu_B B \ll k_B T$) the heat capacity C_S rises proportional to B^2 , while the number of inverted magnetic moments always drops proportional to B^{-1} , which means the signal size grows linearly with B . Going to higher magnetic fields the spin heat capacity C_S becomes the dominant heat capacity ($C_S \gg C_e + C_{ph}$) and approximately all energy flows into the spin system showing the B^{-1} -dependency of equation 2.9 in the signal size. In the limit of high magnetic fields ($\tilde{g}\mu_B B \gg k_B T$) the signal size drops faster with increasing field because the heat capacity C_S crosses its maximum value and drops exponentially.

Figure 2.5 shows the magnetic field dependency of the signal size for 5.9 keV at $T = 30$ mK and $T = 50$ mK for a detector consisting of a $200 \times 200 \times 5 \mu\text{m}^3$ Au:Er sensor with a concentration of 600 ppm and a gold absorber of the same volume.

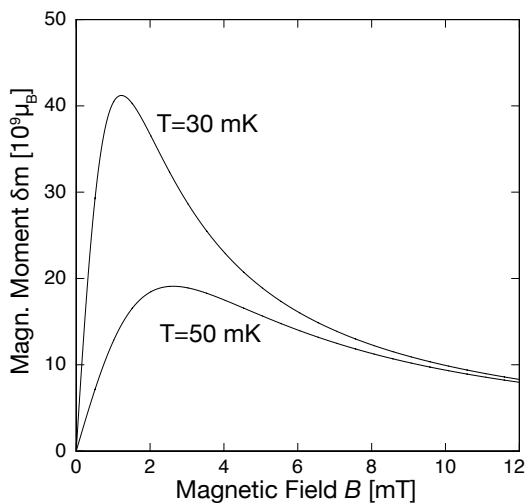


Figure 2.5 The expected signal size in units of magnetic moment for 5.9 keV plotted against the applied magnetic field for two different temperatures. The assumed detector consists of a Au:Er sensor and a gold absorber both of the same volume ($200 \times 200 \times 5 \mu\text{m}^3$). The erbium ions were treated as non-interacting spins in this calculation.

As described, the signal size shows a maximum with regard to the magnetic field at a certain field $B_{\max}(T)$. In first order this maximum is reached if

$$C_S(B_{\max}, T) = C_e(T) + C_{\text{ph}}(T) \quad (2.11)$$

applies. As the phononic and the electronic contribution of the heat capacity rises with temperature the magnetic field where the maximal signal size is found is larger, the higher the temperature as can be seen in figure 2.5.

2.2.4 Influence of Nuclear Spins

Until now the erbium ions in gold were treated as interacting two-level systems at the working temperatures of MMCs. This a good approximation for all natural isotopes of Er except for ^{167}Er because it shows a nuclear spin of $I = 7/2$ and has a natural isotope abundance of 23 %.

The presence of nuclear spin ^{167}Er will influence both the heat capacity and the magnetisation of the sensors because of the hyperfine interaction with the $4f$ -shell electrons and the interaction with an external magnetic field. Figure 2.6 shows the level scheme of the lowest Kramers- Γ_7 doublet of ^{167}Er plotted against the applied magnetic field. The eigenstates divide up in two families with total angular momentum $F = 3$ and $F = 4$ showing an energy gap of $\Delta E = 140 \text{ mK} \cdot k_B$ in zero field and in an applied field a lifted degeneracy of 7 and 9 eigenstates respectively.

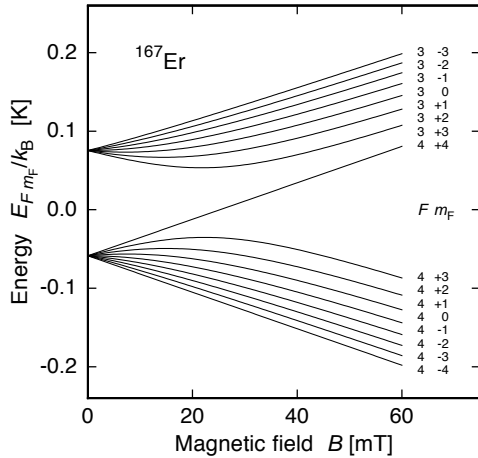


Figure 2.6 The energy eigenstates of ^{167}Er plotted against the applied magnetic field. Special respect should be given to large zero field energy gap of $\Delta E = 140 \text{ mK} \cdot k_B$

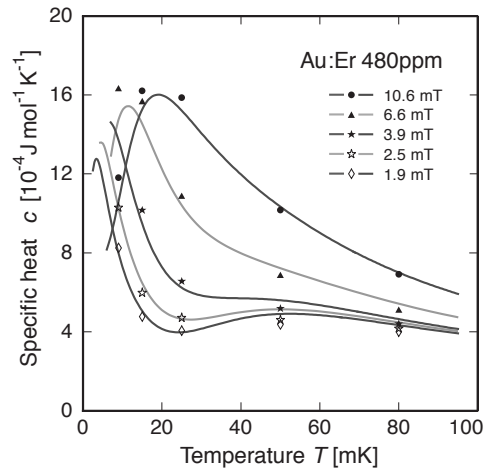


Figure 2.7 The specific heat of Au:Er with 480 ppm of natural composed erbium plotted against the temperature for different magnetic fields. Solid lines represent simulated data while the spots are measured points.

Since in this level scheme transitions without change of magnetic moment are possible between the states with $F = 3$ and $F = 4$, the detector signal size gets reduced. The specific heat is influenced as well, as shown in figure 2.7 for a sample with

480 ppm erbium with the natural isotope abundance. It shows a maximum at low temperatures with a strong magnetic field dependency representing the transitions within the states with $F = 4$ and the ions without nuclear spin. A similar maximum was shown in figure 2.4 where data of a Au:Er sample with a reduced amount of ^{167}Er was depicted, thus only showing the transitions of ions without nuclear spin. The second maximum at $\sim 55\text{ mK}$ can not be found in figure 2.4. It represents the transitions between states with $F = 4$ and $F = 3$. In this temperature region this magnetic field independent maximum is the dominating contribution to the specific heat and a significant part of the underlying transitions will not change the magnetic moment. Thus the total signal size will be greatly reduced in the presence of ^{167}Er in the Au:Er sensor. This leads to the conclusion that it would be best to get rid of ^{167}Er -ions for high sensitivity measurements.

During this work a Au:Er-sputtering target with the natural isotope abundance of erbium was used anyway for the sputter deposited sensors, as a sputtering target with isotopically enriched Er had not been available yet.

2.3 Superconductors

In 1911 Kamerlingh Onnes was investigating the electrical resistance of mercury at low temperatures. He expected some behaviour like

$$\rho = \rho_0 + \rho_{\text{ph}}(T) \quad (2.12)$$

$$\rho_{\text{ph}}(T) \propto T^5 \quad \text{at low temperatures,} \quad (2.13)$$

with ρ_0 a temperature independent contribution due to lattice defects within the crystal and $\rho_{\text{ph}}(T)$ the phononic contribution to the resistance. Instead he saw the electrical resistance dropping to zero below 4.2 K and in this way he discovered superconductivity [Onn11].

2.3.1 Basic Properties

The best known property of superconductors is the sudden drop of the electrical resistivity to zero at a material dependent characteristic critical temperature T_c . On the other hand superconductors show perfect diamagnetism, as first found by Meissner and Ochsenfeld in 1933 [Mei33]. This is at least true for type I superconductors, while type II superconductors show the same electrical behaviour, but a more complex magnetic behaviour. The descriptions in this thesis will only discuss type I superconductors.

There are different theoretical works on the macroscopic and microscopic behaviour of superconductors. After the Meissner-Ochsenfeld effect was found in 1933 the brothers Fritz and Heinz London originated the London equations [Lon35] to describe the penetration of a static external magnetic field into a superconductor.

The London equations were put into a larger context within the phenomenological Ginzburg-Landau theory in 1950 [Gin50], which used an order parameter

to describe superconductivity. During the same year the so called *isotope effect* was discussed theoretically by H. Fröhlich [Frö50] and was experimentally shown by Maxwell [Max50] and Reynolds [Rey50]. It says that the transition temperature T_c is inversely proportional to the average isotopic mass of the superconductor.

This supported the idea of an electron-phonon interaction being important in the microscopic explanation of superconductivity. This theoretical explanation was provided by J. Bardeen, L. Cooper, and J.R. Schrieffer in 1957 in their famous paper on the 'Theory of Superconductivity' [Bar57], which was later called the BCS theory after their originators. In this theory it is assumed that an attractive interaction provided by phonons exists between electrons and that the current is not carried by single electrons any more, but by pairs of electrons, Cooper pairs.

2.3.2 Specific Heat

The specific heat of the detector is a crucial point for the signal size. Therefore it is important to investigate this quantity and its temperature dependence with the aim of getting a good understanding of the device.

Every degree of freedom within the material counts as a contribution to its specific heat. For normal metals the main contributions are:

- electronic specific heat c_e
- phononic specific heat c_{ph} ,

but there can be other contributions, like nuclear moments or degrees of freedom within the spin system. In the case of superconductors one needs to take into account the breaking of Cooper pairs and the resulting quasiparticles¹ and the phase transition from the superconducting to the normal conducting state.

In the normal conducting state (nc) and for the low temperature limit

$$T \ll \Theta_D \quad (2.14)$$

with Θ_D being the Debye temperature the following expressions for the specific heat exist:

$$C_{nc} = \gamma T + \frac{12\pi^4}{5} R \left(\frac{T}{\Theta_D} \right)^3 \quad (2.15)$$

where the first term represents the electronic specific heat and the second term the phononic specific heat. Often at very low temperatures the phononic specific heat can be neglected, since it is orders of magnitude smaller than the electronic contribution.

In the superconducting state electronic specific heat undergoes a change, since the electrons start building Cooper pairs. The BCS theory predicts an exponential behaviour for $T \ll T_c$:

$$C_e = 9.17 \cdot \gamma T_c \cdot \exp\left(-\frac{1.5T_c}{T}\right) \quad (2.16)$$

¹free electrons within a superconductor

and a jump of the specific heat at T_c of

$$\frac{C_e - \gamma T_c}{\gamma T_c} = 1.43. \quad (2.17)$$

Both of these theoretical results fit very well to the experimental observations of quite some superconductors. Just below the critical temperature, $T \lesssim T_c$, the expression

$$C_{sc}(T) = C_{nc}(T) + 2 \frac{B_c(0)^2}{\mu_0} \cdot \left(\frac{T}{T_c} \right) \left[3 \frac{T^2}{T_c^2} - 1 \right], \quad (2.18)$$

as derived in thermodynamic treatment based on empirical description of $B_C(T)$ in eq. 2.20 fit the experimental data better.

The additional term changes its sign at $T_c/\sqrt{3}$, which means that the specific heat of a superconductor is lower than the one of a normal conductor from this point on, which suggests the use of superconductors as components in low temperature calorimeters far below T_c .

2.3.3 Critical Field

In chapter 2.3.1 it was mentioned that superconductors are perfect diamagnets and therefore expell all external magnetic fields. But this is only true up to a certain value of the magnetic field, the so-called critical magnetic field B_c . If a magnetic field exceeding the critical one is applied, the superconductivity breaks down and the material becomes normal conducting.

For type I superconductors the critical magnetic field at $T = 0$ can be thermodynamically calculated:

$$B_c(T = 0) = \frac{\Phi_0}{2\sqrt{2}\pi\lambda\xi} \quad (2.19)$$

with $\Phi_0 = h/2e = 2.07 \cdot 10^{-15} \text{ V} \cdot \text{s}$ the magnetic flux quantum, the London penetration depth λ and the coherence length ξ . And the following temperature dependence was found empirically:

$$B_c(T) = B_c(0) \cdot \left(1 - \frac{T^2}{T_c^2} \right) [\text{Poo95}]. \quad (2.20)$$

2.3.4 Energy Absorption and Down Conversion in a Superconductor

In the application as particle absorber, superconductors show major differences to normal metal absorbers. As already discussed in chapter 2.3.5 and 2.3.2 the electronic heat capacity becomes very small at temperatures far below the transition temperature, making them very attractive as particle absorbers of low temperature detectors. However, the thermalisation within a superconductor shows peculiar behavior compared to the one in normal metal absorbers. This is mainly because of

the weakly bound Cooper pairs, which can be easily broken, forming quasiparticles² that store the binding energy until their recombination to Cooper pairs.

In the following, a theoretical model will be described for the energy down conversion in a superconductor following [Koz00a, Koz00b].

When an x-ray photon is absorbed in a superconductor it is most likely that initially a single photo electron is produced. The electron loses its kinetic energy very fast via secondary ionisation and plasmon emission. Within picoseconds the initial energy is mainly carried by electrons with an average energy in the order of a characteristic energy E_1 . E_1 is defined as the energy where the scattering rate of electron-electron interaction $\tau_{ee}^{-1}(\epsilon)$ is of the same size as the one of the electron-phonon interaction rate $\tau_s^{-1}(\epsilon)$.

From this point on the electrons start to emit a cascade of high-energy phonons with energies of about the Debye energy Ω_D . The phonons with energy Ω_D exist long enough, so that they carry nearly all energy and form a so-called phonon bubble. Further thermalisation happens mainly through breaking Cooper pairs, releasing two high-energy quasiparticles, which by emitting lower energy phonons, relax down to the superconducting edge. Thus the energy in the phonon system stays mainly constant and the number of quasiparticles raises linear in time:

$$N_{\text{qp}} \approx \frac{E_{\text{ph}}(0)}{\Omega_D} (1 + 2\lambda_1 \Omega_1 t) \quad (2.21)$$

This behaviour is valid until another characteristic average energy Ω_1 is reached which is defined where the quasiparticle scattering with phonon emission becomes as probable as the Cooper pair breaking ($\tau_s(\Omega_1) = \tau_B(\Omega_1)$).

Subsequently the number of quasiparticles behaves differently due to the other interaction probabilities:

$$N_{\text{qp}} = \frac{E_x}{\Omega_1} \left(\frac{t}{\tau_s(\Omega_1)} \right)^{1/3} \Gamma \left(\frac{2}{3} \right) \quad (2.22)$$

with E_x being the initial photon energy. The energy stored in the phonon system decreases rapidly:

$$E_{\text{ph}} = \frac{E_x}{6} \left(\frac{t}{\tau_s(\Omega_1)} \right)^{-2/3} \Gamma \left(\frac{2}{3} \right) \quad (2.23)$$

When the average particle energy is $E_2 = 3\Delta$, with 2Δ being the superconducting energy gap, nearly all energy is carried by quasiparticles and the quasiparticles left with an energy smaller than E_2 can not break any Cooper pairs and can only relax to the superconducting edge by emitting low energetic phonons and recombine to Cooper pairs. This part can be described by an equilibrium theory [Kap76].

²single, unbound electrons within a superconductor

The time for the relaxation to the energy gap $E = \Delta$ is:

$$\frac{\tau_0}{\tau_s}(\Delta, T) \simeq \Gamma \left(\frac{7}{2} \right) \zeta \left(\frac{7}{2} \right) \left(\frac{k_B T_c}{2\Delta(0)} \right)^{\frac{1}{2}} \left(\frac{T}{T_c} \right)^{\frac{7}{2}}, \quad (2.24)$$

while the recombination to $E = 0$ takes the following time:

$$\frac{\tau_0}{\tau_r}(\Delta, T) \simeq (\pi)^{\frac{1}{2}} \left(\frac{2\Delta(0)}{k_B T_c} \right)^{\frac{5}{2}} \left(\frac{T}{T_c} \right)^{\frac{1}{2}} e^{-\frac{\Delta(0)}{k_B T}} \quad (2.25)$$

In the previous two expressions a material dependent timescale τ_0 is used:

$$\tau_0 = \frac{Z_1(0)\hbar}{2\pi b(k_B T_c)} \quad (2.26)$$

In the different publications [Koz00b, Kap76] calculated timescales for the different phases of the down conversion can be found. The values for aluminium at 50 mK are:

$$t_I = 140 \text{ ps} \quad (\Omega_D \rightarrow \Omega_1) \quad (2.27)$$

$$t_{II} = 1.3 \text{ ns} \quad (\Omega_1 \rightarrow E_2) \quad (2.28)$$

$$\tau_s = 16 \text{ ms} \quad (E_2 \rightarrow \Delta) \quad (2.29)$$

$$\tau_r = 8 \cdot 10^9 \text{ s} \quad (\Delta \rightarrow 0). \quad (2.30)$$

While t_I and t_{II} happen on such short time scales that can not be discriminated by MMCs, τ_s is in the order of the typical signal decay times. τ_r on the other hand is much too long to be seen. The described theory might however not fit perfectly to the scenario in x-ray detectors. On the one hand [Kap76] assumes an infinitely large perfect single crystal on the other hand an equilibrium theory is used while the quasiparticle density after a x-ray absorption is much higher than in equilibrium.

But even if the realistic time scales are orders of magnitude faster than the calculated τ_r the quasiparticle recombination time is a good candidate for the longest decay time within a detector with superconducting absorber. That is because all other transport processes within the detector are predicted to be in the 2-digit millisecond range or faster at temperatures around 50 mK. This includes electronic and phononic heat transfer between absorber and sensor ($\tau < 1 \mu\text{s}$) and through the weak thermal link to the bath (about $\tau = 10 \text{ ms}$). Other experiments done with normal conducting absorbers agree very well with the predictions. And the major difference between normal conducting and superconducting materials is the existence of Cooper pairs.

Therefore a further investigation of the time scales of relaxation processes as well as finding ways to influence these time scales are of interest for the use of superconducting absorber materials in micro-calorimeters.

2.3.5 Importance of superconducting absorber materials

Superconductors can be very useful as absorber material. Since the specific heat becomes very small for $T \ll T_c$ the absorber heat capacity becomes negligible (chapter 2.3.2). In the soft x-ray region and especially in the hard x-ray or γ -ray region, the discrepancy between normal metal absorber and superconducting absorber can be impressive as seen in the following example.

A detector for 100 keV x-rays operated at 50 mK, with 1 mm² detection area and 99 % stopping power at using gold and superconducting rhenium as absorber material will be compared. The required thicknesses are about 300 μm for gold and 310 μm for rhenium [Hub96], this corresponds to a heat capacity of 1000 pJ/K for gold (eq. 2.15) and 0.11 pJ/K for superconducting rhenium (eq. 2.16).

Another reason to use superconducting absorber materials is found in a particular application, i.e. in experiments using micro-calorimeters to search for the neutrino mass. The β -decay of ¹⁸⁷Re shows the lowest known Q -value, being 2.47 keV, and is predestinated to determine the electron anti-neutrino mass. Low temperature detectors with Re-based absorbers are promising tools for this experiment because of their good energy resolution. The use of natural rhenium can be in principle an optimal choice since it can provide relatively high activity per pixel together with a low heat capacity. Rhenium is superconducting at temperatures below $T_c = 1.7$ K and will therefore be well below T_C at the working temperatures of the detectors.

Using an absorber of bulk superconducting rhenium has the advantage that absorber and source are combined since ¹⁸⁷Re has a natural isotope abundance of about 62.6 % and by varying the size of the absorber the activity can be adjusted without changing the heat capacity very much.

The optimisation of the single pixel and the production of thousands of pixels, to reach the right sensitivity on the neutrino mass is the aim of an international collaboration named MARE³ [Mon06].

2.3.6 Previous Experiments

Prior to the work discussed here, quite a number of experiments with superconducting particle absorbers were carried out in order to understand the thermalisation of energy. The results of those suggested new experiments, some of which were done during this work.

The first experiments to be mentioned were discussed in 1993 by E. Cosulich et al. [Cos93], who used a germanium thermistor to measure the temperature pulses in different superconducting materials under two different conditions. The signals generated by a short thermal pulse produced by a resistor were compared to the signals originating from absorbed α -particles. Major differences between the pulse shapes were found below $T^* = 2 \cdot 10^{-4} \Theta_D$ and, because of the difference in area between thermal pulses and α -pulses corresponding to the same energy, it seemed, that energy was lost for the pulses originated by the α -particles. The observations

³Microcalorimeter Array for a Rhenium Experiment

agreed for different superconducting absorber materials but could not be explained by a theoretical model.

Another experiment was presented in 1994 by C. K. Stahle et al. [Sta94] comparing x-ray absorption in Sn and in a layer of silver-filled epoxy on top. This was read out by a silicon thermistor. In addition the effect of cooling down through the superconducting transition of tin in an applied magnetic field was investigated. The events presumably absorbed in the Ag, and down converted to excitations of thermal energy there, showed a larger pulse height and a faster thermalisation than the ones absorbed in tin. The integral under the pulses, which corresponds to the deposited energy, was larger for the Ag events as well. This difference was attributed to the different thermalisation behaviour of the systems most notably the quasiparticle thermalisation within the tin. After cooling in an applied magnetic field the differences could not be distinguished any more which was explained by the increased quasiparticle density due to trapped flux. After cooling once more without field the original behaviour was restored again.

Presently bulk tin absorbers are developed for 256-pixel TES⁴-arrays for energies up to 200 keV [Dor08]. The application is mainly in the high energy γ -ray measurement for example in the characterisation of radioactive materials. An energy resolutions of 25 eV FWHM at 103 keV was obtained for a single pixel of a 14-pixel prototype array.

As mentioned, another very interesting superconducting absorber material is rhenium. Due to its high stopping power it can be used as γ -ray absorber, but presently the main interest is in its use for micro-calorimeters in the MARE project. Different experiments have already been done with superconducting rhenium absorbers.

In our group at the Kirchhoff-Institute for Physics, Metallic Magnetic Calorimeters are being developed coupled to superconducting absorbers. The starting point was a contribution to the MARE project, using MMCs with superconducting rhenium absorbers. The first approach used a foil of bulk Au:Er, a gold foil as spacer layer and a rhenium crystal, every layer glued on top of each other, and the stack glued on a MagCal Nr. 14 (further description in chapter 2.4) with epoxy glue⁵ suitable for low temperatures [Hau06]. It was shown that MMCs can in principle be used with superconducting absorbers despite the magnetic field used to polarise the spins in the sensor. Further on the spacer and sensor layer were sputter deposited directly onto the rhenium crystal to provide a better thermal conductivity between the different layers and this sensor/absorber-system was glued on a MagCal Nr. 14 [Por07]. As expected the rise times became much faster because of the stronger coupling of sensor and absorber. The thermalisation behaviour of a similar device was studied more extensively [Höh08]. The next step will be to use a micro-fabricated detector using diffusion welding to fix the rhenium absorber on the micro-fabricated device [Kir10]. This will allow to study the real time constants of the detector, being free from any systematic contribution due to the presence of the layer of glue defining

⁴Transition Edge Sensor which measure the strongly temperature dependent electrical resistance of a superconductor in the superconducting transition

⁵STYCAST 2850 FT or STYCAST 1266 by Emerson & Cuming

the thermal link to the bath.

In order to better understand the thermalisation of energy in superconducting absorbers it is important to compare the behavior of different superconducting materials and also under different conditions.

A very important preliminary work was conducted by Richard Weldle in 2008 [Wel08], who examined the effect of magnetic impurities in a superconducting absorber on the thermalisation of energy. By doping superconductors with small concentrations of magnetic impurities, intermediate states in the superconducting energy gap can be introduced. Because of the enhanced scattering of electrons at the magnetic impurities the attractive interaction between the electrons that leads to the forming of Cooper pairs is weakened. The macroscopic effects can be the effective reduction of the superconducting energy gap and a drop of transition temperature. Therefore this should lead to shorter recombination times of the quasiparticles (see chapter 2.3.4), who are most likely to be the cause of the long thermalisation times in superconducting absorber materials.

For that matter two detectors were built with $500\ \mu\text{m}$ thick absorbers made of aluminium and aluminium doped with 2000 ppm of manganese. The doping caused the transition temperature T_c to drop from 1.12 K to about 300 mK and to reduce the energy gap to approximately zero.

Unfortunately the proposed effect was not shown, probably because aluminium doped with manganese forms a Kondo system. But the pulses showed other differences on a shorter time scale, i.e in the rise time of the signals. On the other hand the observations in [Cos93] were confirmed, because the pulse shape changed drastically at a temperature of were found above $T^* < 2 \cdot 10^{-4} \Theta_D$. The missing energy was not confirmed since only x-rays from a ^{55}Fe were used and no comparison with calibrated heat pulses was available.

This led to the idea to study the difference of x-ray absorption in the superconductor and the sensor or spacer layer underneath, which was implemented by using a thinner absorber of about $50\ \mu\text{m}$ with a finite probability of about 20 % for 6 keV x-rays not to be absorbed until they reach the spacer layer underneath the absorber. The photon energy of those events should down convert in the normal metal parts of the detector and reach the superconducting absorber as thermal pulses, as was the case in experiments with resistive heater.

2.4 Detector Geometry

So far all calculations considering the detector signal were done without taking the geometry into account. But to get a quantitative understanding the coupling and the geometry of the detector need to be considered. The best results so far – an energy resolution of 2.7 eV – were obtained with a cylindric geometry using a small circular loop as pickup coil with a large wire wound coil creating a homogeneous magnetic field [Lin07]. But for certain applications a cylindrical geometry is not very well suited.

For example the 100 keV photon detector described in section 2.3.5 at 50 mK

with a 1 mm^2 rhenium absorber and a heat capacity of 0.11 pJ/K could be used in a cylindrical geometry. Following optimisation calculations conducted A. Fleischmann et al. [Fle05] the sensor would need a radius of $5 \mu\text{m}$ for optimal performance. This setups would be mechanically quite unstable and possibly hard to fabricate. This gets even harder if one aims for re-produceable detectors for detector arrays. Additionally the optimal magnetic field for such a detector is 15 mT , which is quite high and very close to the critical field of rhenium of 20 mT and can compromise the superconductivity, spoiling the advantages of superconducting absorbers.

For many applications a meander-shaped pickup coil geometry is better suited.

2.4.1 MMCs with meander-shaped pickup coil

Following the term meander (from the river “*Μαίανδρος*” or “Meander” in today’s Turkey) for a sinuously bent river a pickup loop can be designed (see figure 2.8). Figure 2.9 shows the cross section of two stripes of a meander-shaped pickup coil. It shows two neighbouring meander stripes, made of niobium, covered by a thin layer of insulation material, SiO_2 , on a solid substrate made of silicon. On top is a thin glue layer to fix the sensor and the absorber.

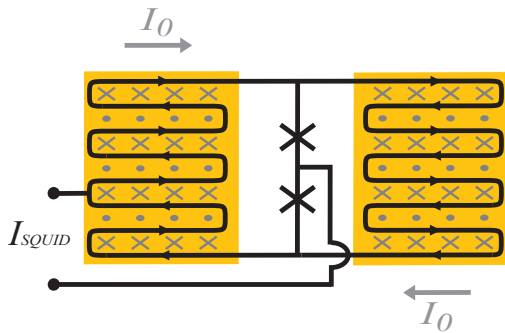


Figure 2.8 A possible read out scheme for an MMC with a gradiometric meander-shaped pickup coil. The structures carry the magnetic field generating persistent current I_0 and the detector SQUID is directly integrated into the setup.

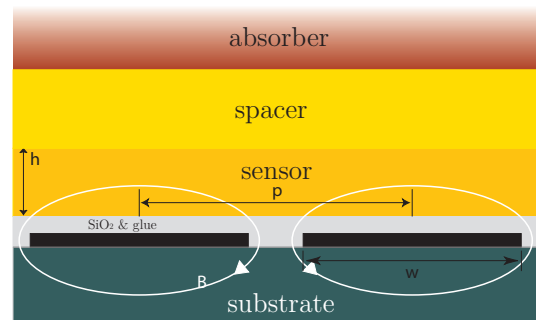


Figure 2.9 Cross-sectional view of two neighbouring meander stripes. On top the glue layer, the sensor with height h and the absorber are shown.

In a closed superconducting loop containing the meander-shaped pickup coil a persistent current can be frozen (see chapter 3.4.1) to use the pickup loop also to create a magnetic field. The resulting magnetic field is indicated in figure 2.9 as well and will further be described in section 2.4.2. The highly inhomogeneous magnetic field is more difficult to calculate (see section 2.4.2) but has the advantage that it decays exponentially with the distance z from the meander [Fle05] and therefore allows the use of superconducting absorbers in close distance without compromising superconductivity [Hau06].

In addition the meander geometry can be more sensitive than a cylindrical geometry because the pickup coil stripes are in average closer to each volume element

of the sensor and therefore the coupling of the spins to the pickup loop is better.

The signal of an MMC with meander-shaped pickup coil is the flux change within the area of the meander. Because of the inhomogeneous field and the different coupling the change of flux $\Delta\Phi$ caused by a change of magnetisation ΔM is dependent on the position \vec{r} of the volume element. Combining these considerations leads to

$$d(\Delta\Phi) = \mu_0 \frac{G(\vec{r}/p)}{p} \Delta M(\vec{r}) dV \quad (2.31)$$

with a dimensionless geometrical coupling factor $G(\vec{r}/p)$ which describes the coupling between the spins in the sensor and the meander-shaped pickup coil..

$G(\vec{r}/p)$ satisfies a simple relation to the field generating current I_0 and the created magnetic field $B(\vec{r})$ [Bur04]:

$$B(\vec{r}) = \mu_0 G(\vec{r}/p) \frac{I_0}{p}. \quad (2.32)$$

By combining the last two equations with equation 2.3 and integrating over the sensor volume one obtains for the flux change upon the deposition of an energy ΔE :

$$\Delta\Phi = \frac{\Delta E}{C_a + \int_V c_s(\vec{r}) dV} \mu_0 \int_V \frac{G(\vec{r}/p)}{p} \frac{\partial M[B(\vec{r}, T)]}{\partial T} dV. \quad (2.33)$$

Calculating $\Delta\Phi$ with this volume integral is possible but not very efficient in terms of computing time. But introducing a weighted average over ξ of a quantity A as

$$\langle A \rangle_\xi = \int P(\xi) A(\xi) d\xi, \quad (2.34)$$

the integration in eq. 2.33 can be replaced by an integration over G leading to

$$\frac{\Delta\Phi}{\Delta E} = \frac{V}{C_a + V \langle c_s \rangle_G} \mu_0 \left\langle \frac{G}{p} \frac{\partial M}{\partial T} \right\rangle_G \quad (2.35)$$

and this integration can be determined with somewhat reduced computing time using the distribution of the absolute value of magnetic field within the sensor volume as determined by finite element simulations for the magnetic field distribution described in the next section.

2.4.2 Magnetic Field Distribution

The magnetic field distribution originating from a current carrying meander structure is highly inhomogeneous. To get a quantitative estimate of the detector response the knowledge of the distribution of B in the sensor volume is necessary. Since an analytical solution to this problem is highly demanding it is useful to use numerical simulations which can be conducted e.g. with the finite element program FEMM⁶.

⁶Finite Element Methods Magnetics. Freeware written by David Meeker; <http://femm.berlios.de>

For the simulations the geometry of the detector needs to be known. This includes the width $w = 20 \mu\text{m}$ and the pitch $p = 25 \mu\text{m}$ and the height of 400 nm of the used meander structure, the height of the insulating and glue layer of about $1.5 \mu\text{m}$ and the sensor height of $h = 3 \mu\text{m}$. For the use of superconducting absorbers an additional gold spacer layer of $4 \mu\text{m}$ is added above the sensor.

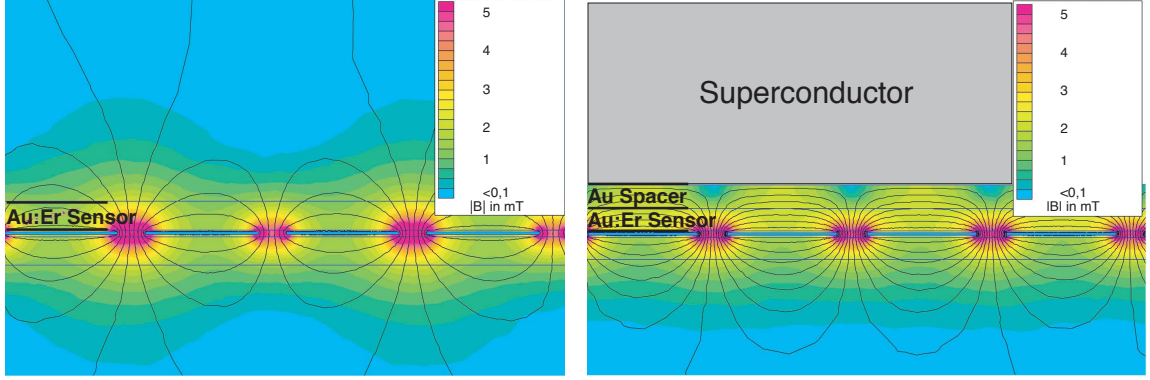


Figure 2.10 The magnetic field distribution of the meander of a MagCal Nr. 15 simulated with FEMM. On the left without superconducting absorber and on the right the altered distribution with a superconductor above. With the superconductor the field lines are squeezed and the field becomes larger below the superconductor and therefore within the sensor.

In figure 2.10 the results of a simulation with an persistent current of $I = 100 \text{ mA}$ running through the meander stripes is shown. On the left the result without a superconductor is shown assuming the meander stripes made of niobium to be perfectly diamagnetic ($\chi = -1$) and the paramagnetic sensor not influencing the magnetic field distribution, which is a reasonable approximation, because of the small magnetic susceptibility ($\chi < 0.15$) for the used erbium concentrations in the relevant temperature range.

The results change very strongly if a plane with a homogeneous Dirichlet boundary condition ($\vec{\nabla} \times \vec{A} = 0$) is introduced above the gold spacer depicted in figure 2.10 (right) to simulate a superconductor with no magnetic flux penetration. The field gets “squeezed” by the superconductor increasing the mean field within the sensor volume for the same persistent current I and therefore increasing the detector’s signal size since the optimal field B_{opt} can not be reached in this setup.

The absolute value of the magnetic field B can now be assessed at several thousand randomly distributed points within the sensor and the probability $P(B)dB$ to find a certain value of B within the interval $[B, B + dB]$ can be evaluated.

2.5 Fundamental Limits on the Energy Resolution

The performance and in particular the energy resolution of a detector depend on many different influences. It seems obvious, that one wants to maximise the signal size while minimising the noise in order to achieve best signal-to-noise and therefore

the best energy resolution. Some sources of noise (such as vibrations, external electromagnetic radiation or temperature fluctuations of the setup) can be reduced or eliminated by a careful experimental setup. On the other hand there are some intrinsic influences or noise contributions, which depend on the detection principle and on the total experimental set up, those can be reduced but not completely eliminated.

To get a better theoretical understanding and to predict the detector performance it is useful to know the different intrinsic noise contributions as well as the predicted signal (from chapter 2.2 and 5.4).

2.5.1 Detector Response

In a simple model a calorimeter consists of three parts. An absorber strongly connected to a thermometer, which are considered as a system of heat capacity C_{tot} at the temperature T_t and a weak thermal link to a thermal bath at a fixed temperature T_0 , with a thermal conductivity G_{tb} . With an external power input

$$\dot{Q}(t) = E\delta(t) \quad (2.36)$$

with the deposited energy E and the Dirac delta function $\delta(t)$ as approximation for a particle hitting the absorber, this setup leads to the following differential equation:

$$C_{\text{tot}}\dot{T}_t = G_{\text{tb}}(T_t - T_0) + \dot{Q}(t) \quad (2.37)$$

and the following solution:

$$T_t(t) = T_0 + \frac{E}{C_t}e^{-t/\tau}, \quad (2.38)$$

with

$$\tau = \frac{C_{\text{tot}}}{G_{\text{tb}}} \quad (2.39)$$

being the characteristic time constant of the system to return to equilibrium conditions.

In reality absorber and thermometer are not thermalising instantly and at the same time. To take this into account one can split absorber and thermometer in two sub-systems. In the case of MMCs, the electronic heat capacity typically dominates the heat capacity of the absorber and equilibrates very fast with the electrons of the sensor. Therefore, we want to treat them as one thermal system with heat capacity C_e . The thermometer instead is represented by the magnetic moments, having a heat capacity C_s , which have a finite thermal link G_{es} to C_e and no direct thermal link to the bath. In figure 2.11 the two systems are strongly coupled by the thermal conductance G_{es} while only the electron system is connected to the bath. The energy is deposited into the electron subsystem. The new differential equations are now:

$$C_e\dot{T}_e = -G_{\text{es}}(T_e - T_s) - G_{\text{eb}}(T_e - T_0) + \dot{Q}(t) \quad (2.40)$$

$$C_s\dot{T}_s = -G_{\text{es}}(T_s - T_e), \quad (2.41)$$

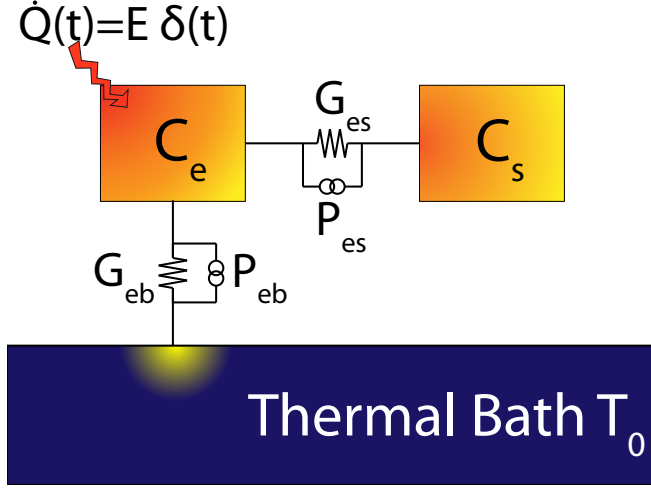


Figure 2.11 The model of a calorimeter as canonical ensemble with two different subsystems.

leading to the solution for the spin temperature T_s :

$$\Delta T(t) = T_s(t) - T_0 = \frac{E}{C_s + C_e} (-e^{-t/\tau_0} + e^{-t/\tau_1}) \quad (2.42)$$

where τ_0 and τ_1 are the characteristic rise and decay times of the thermometer system with the following analytical solution:

$$\frac{1}{\tau_0} = \frac{1}{2C_e C_s} \left[C_s(G_{eb} + G_{es}) + C_e G_{es} + \sqrt{(C_s(G_{eb} + G_{es}) - C_e G_{es})^2 + 4C_e C_s G_{es}^2} \right] \quad (2.43)$$

$$\frac{1}{\tau_1} = \frac{1}{2C_e C_s} \left[C_s(G_{eb} + G_{es}) + C_e G_{es} - \sqrt{(C_s(G_{eb} + G_{es}) - C_e G_{es})^2 + 4C_e C_s G_{es}^2} \right] \quad (2.44)$$

2.5.2 Intrinsic Noise Contributions

Magnetic Johnson Noise

The thermal Johnson noise can be interpreted as a generalisation of the Brownian motion [Bro28] to the charge carriers within a conductor, which results in a voltage noise over the conductor. This effect was firstly shown experimentally by J. B. Johnson in 1928 [Joh28] and quantified theoretically by H. Nyquist [Nyg28] in a gedankenexperiment in the same year.

The noise only depends on the resistance R , the temperature T and the frequency ν , which are combined in the Nyquist expression for the spectral power density S_U

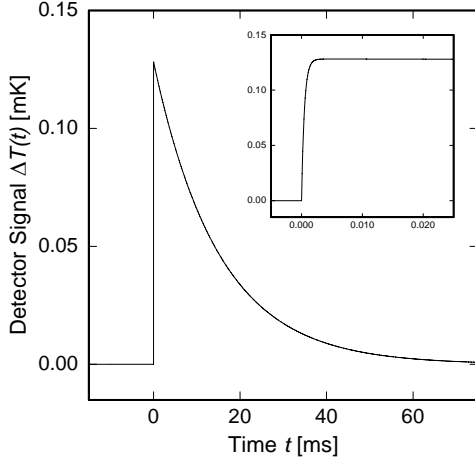


Figure 2.12 The detector signal $\Delta T(t)$ following equation 2.42 for $C_e = 0.5$ pJ/K, $C_s = 7$ pJ/K, $G_{es} = 1$ μ W/K and $G_{eb} = 0.5$ nW/K resulting in $\tau_0 = 0.5$ μ s and $\tau_1 = 15$ ms. The deposited energy is $E = 6$ keV. The inset shows the beginning of the response in a short time window.

of voltage noise

$$S_U = \frac{\langle U \rangle}{\Delta\nu} = 4k_B T R. \quad (2.45)$$

It is worth to mention that the value of S_U is independent of any other material properties or geometry, which was shown in Johnson's experiments as well.

If one shorts the electrical conductor with an ideal conductor the resulting voltage noise can be expressed in spectral power density of current noise

$$S_I = \frac{\langle I^2 \rangle}{\Delta\nu} = \frac{4k_B T}{R}. \quad (2.46)$$

Every current induces a magnetic field, which means the current noise generates a magnetic flux noise as well. This kind of flux noise is called magnetic Johnson noise.

Since the investigated detectors use electrical conductors as sensor and absorber material coupled to a SQUID (see chapter 2.4) the magnetic Johnson noise needs to be considered as noise contribution. The spectrum is independent of frequency (so-called white noise) until it cuts off like a low pass at high frequencies, typically in the MHz range, due to the skin effect. For the same quantity of conducting material the magnetic Johnson noise contribution depends on the coupling scheme to the SQUID. For example a meander shaped pick-up coil (see chapter 2.4.1) can help to reduce the effect of magnetic Johnson noise.

Thermodynamic Fluctuation Noise

Every impedance between thermodynamic subsystems can be treated as noise source represented by P_{es} and P_{eb} in figure 2.11 with the spectral power density:

$$S_{P_{es/eb}} = 4k_B T^2 G_{es/eb}. \quad (2.47)$$

Inserting the thermodynamic fluctuation noise in the differential equations 2.40-2.41 and setting the power input $\dot{Q}(t) = 0$ results in:

$$C_e \dot{T}_e = -G_{es}(T_e - T_s) - G_{eb}(T_e - T_0) + P_{es}(t) - P_{eb}(t) \quad (2.48)$$

$$C_s \dot{T}_s = -G_{es}(T_s - T_e) - P_{es}(t). \quad (2.49)$$

Solving and transforming the equations into frequency space one gets the spectral power density of the energy fluctuations within the spin system:

$$S_{E_s}(\nu) = k_B T^2 C_s \left(\frac{4\alpha_0 \tau_0}{1 + (2\pi\tau_0\nu)^2} + \frac{4\alpha_1 \tau_1}{1 + (2\pi\tau_1\nu)^2} \right), \quad (2.50)$$

with the characteristic time constants τ_0 and τ_1 and the dimensionless parameters α_0 and α_1 satisfying the relation $\alpha_0 + \alpha_1 = 1$ and depending on the heat capacities and the time constants. Furthermore, the approximations $\alpha_0 \approx 1 - \beta$ and $\alpha_1 \approx \beta$ can be made in case of the typical conditions $C_s \approx C_e$, $\tau_0 \ll \tau_1$ with $\beta = C_s/(C_s + C_e)$ being the relative heat capacity of the spin subsystem.

Readout noise

The read out circuit is contributing to the overall noise as well. This contribution consists of the SQUID⁷ noise of the detector SQUID $S_{\Phi, \text{det}}$ and amplifier SQUID $S_{\Phi, \text{amp}}$ and noise of the room temperature readout electronics $S_{U, \text{el}}$. Further noise contributions from the used preamplifiers or the digitalisation noise of the analogue-to-digital converter are not discussed, since the impact on the measurement is in this work negligible in comparison to the contributions mentioned before.

As for the description of these noise contributions basic knowledge of SQUIDs and their readout is required the detailed discussion will be postponed to chapter 3.2.3 after SQUIDs are introduced.

Therefore only the typical values for the used SQUIDs will be mentioned, consisting of $\sqrt{S_{\Phi, \text{SQ}, w}} \approx 1 \mu\Phi_0/\sqrt{\text{Hz}}$ white noise level and a $1/f$ -dependent noise contribution of $\sqrt{S_{\Phi, \text{SQ}, 1/f}|_{1 \text{ Hz}}} \approx 7 \mu\Phi_0/\sqrt{\text{Hz}}$ at 1 Hz.

Intrinsic $1/f$ Noise of the Au:Er sensor

In the case of MMCs an additional noise contribution can be observed. The microscopic origin of this noise is not understood so far. Investigations during the last years characterised the contribution extensively and we think that we can describe it now at least on an empirical level.

The origin seems to be related to the erbium-ions in the sensor material. This was tested in [Dan05] by using two gradiometrically connected pick up coils with a different number of sensors at 4.2 K. In figure 2.13 the different results can be seen. Without a sensor a frequency independent -white- and a $1/f$ part can be observed, as expected for a SQUID (see chapter 3.2.3). By adding one sensor in one of the pick-up

⁷Superconducting Quantum Interference Device, for further information on SQUIDs see chapter 3.2

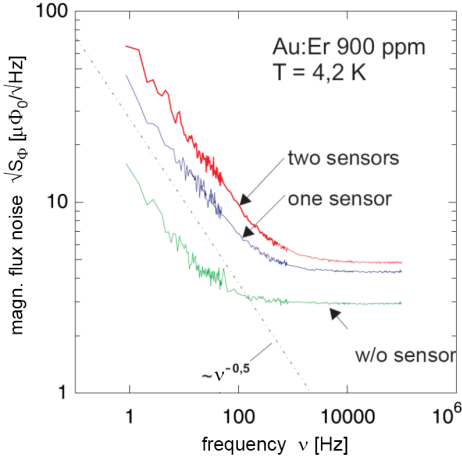


Figure 2.13 Different flux noise spectra of the same gradiometric calorimeter with zero, one or two sensors

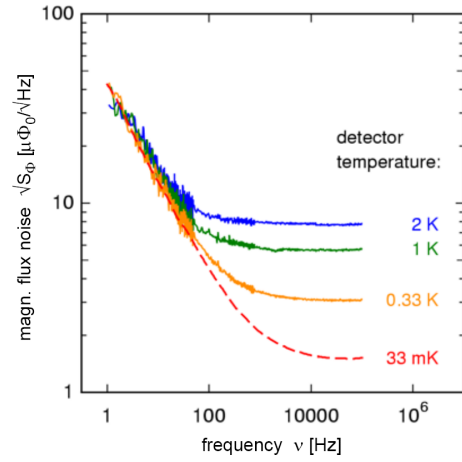


Figure 2.14 Different flux noise spectra of a magnetic calorimeter at different temperatures

loops both the white noise, due to the magnetic Johnson noise of the sensor, and the $1/f$ part increased. After adding the second identical sensor to the second loop the contributions increased further by a factor of $\sqrt{2}$. The same measurements were done with sensors having an erbium concentration of 300 ppm. The result showed that the $1/f$ noise depends on the erbium concentration, too.

Another remarkable observation is that no temperature dependency over two orders of magnitude was seen for the $1/f$ noise [Fle03]. While the white noise level in figure 2.14 increases with temperature the $1/f$ contribution stays the same.

The contribution can be quantitatively described for a meander-shaped pickup coil as:

$$S_{\Phi, \text{Er}}(\nu) = \frac{\mu_0 \langle G \rangle}{p} S_m(\nu) N_{\text{Er}} N_{\text{sens}}, \quad (2.51)$$

with $\langle G \rangle$ the effective geometry factor of the detector geometry, p the pitch of the meander geometry, $S_m(\nu)$ the frequency dependent noise of a single erbium-ion, N_{Er} the number of erbium ions and N_{sens} the number of sensors (1,2). By analysing the noise of high-resolution detectors $S_m(\nu)$ was determined to be:

$$S_m(\nu)|_{1 \text{ Hz}} = 0.12 \mu_{\text{B}}^2 / \text{Hz}. \quad (2.52)$$

Recent examinations (e.g. [Pab08]) suggest that the frequency dependency is not strictly $1/f$, but depends on the fabrication process or the geometry of the sensor as well. While [Dan05] and [Fle03] used rolled foils out of bulk Au:Er in [Pab08] the sensor was sputter deposited and the noise contribution showed a frequency behaviour like $1/f^\alpha$ with $\alpha = 0.85$. Other works, like this thesis, with sputter deposited sensors show other exponents with $\alpha < 1$.

A possible explanation for the erbium noise might be spin-spin-fluctuations, which appear in spin-glasses and show typically a $1/f$ -dependency. But the temper-

atures during the measurements are one to two orders of magnitude higher than the expected spin-glas transition for the used Au:Er-alloys. On the other hand the noise should show a very strong temperature dependency. In [Bur08] it was shown that the origin of the noise is not the interaction between erbium ions and the quadrupole moments of the gold nuclei. The noise spectra of two similar detectors, one using Au:Er and the other one using Ag:Er as sensor material, were compared and showed the same $1/f$ noise contribution per spin. Since natural Ag has a nuclear spin of $I = 1/2$ it has no quadrupole moment and this interaction can not be the underlying cause of this noise contribution.

2.5.3 Signal-to-Noise Ratio and Energy Resolution

The determination of the Signal-to-Noise ratio is best done in frequency space. All noise contributions are already stated in frequency space, but the signal needs still to be transformed. The detector response (out of equation 2.42) transformed under the limitations $\beta \approx 0.5$, $\tau_0 \ll \tau_1$ and only for positive frequencies results in:

$$|\tilde{p}(\nu)| \approx \frac{2\tau_1\beta}{\sqrt{1 + (2\pi\tau_0\nu)^2}\sqrt{1 + (2\pi\tau_1\nu)^2}} \quad (2.53)$$

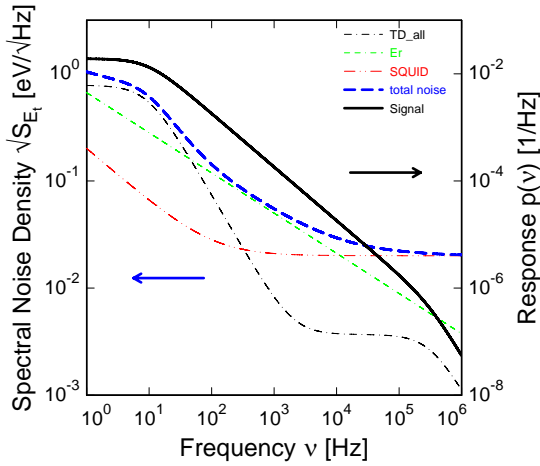


Figure 2.15 Plotted to the left axis the different intrinsic noise contributions and the total noise, and to the right axis the detector response in frequency space following equation 2.53.

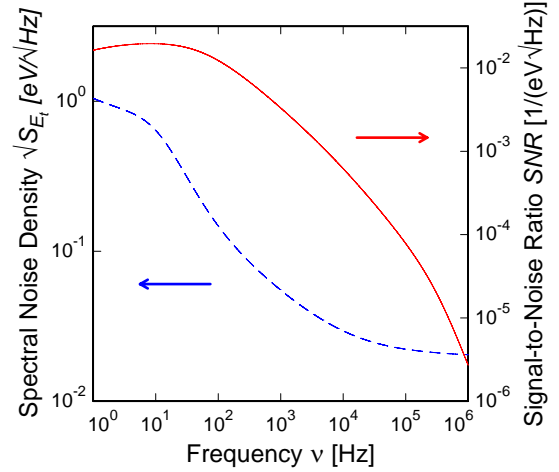


Figure 2.16 To the left axis the total noise in comparison with the signal-to-noise ratio SNR plotted to the right axis.

To get to the energy resolution in the end it is useful to look at the noise not in flux as done in chapter 2.5.2, but directly in the energy contained in the spin subsystem.

$$S_{E_s, \text{tot}}(\nu) = \beta \frac{dE}{d\Phi} S_{\Phi, \text{tot}}(\nu) \quad (2.54)$$

$$= \beta \frac{dE}{d\Phi} (S_{\Phi, E_s}(\nu) + S_{\Phi, \text{Er}}(\nu) + S_{\Phi, \text{Johnson}} + S_{\Phi, \text{SQ}, w} + S_{\Phi, \text{SQ}, 1/f}(\nu)). \quad (2.55)$$

Now the signal-to-noise ratio SNR is defined as follows:

$$SNR(\nu) = \frac{\tilde{p}(\nu)}{\sqrt{S_{E_s, \text{tot}}(\nu)}} \quad (2.56)$$

and integrating over the whole frequency range leads to the energy resolution:

$$\Delta E_{\text{FWHM}} = \frac{2\sqrt{(2 \ln(2))}}{\sqrt{\int_0^{\infty} (SNR(\nu))^2 d\nu}}. \quad (2.57)$$

In figure 2.15 the detector response, the noise contributions and the over all noise are shown for an exemplary MMC. Figure 2.16 displays the SNR in comparison with the total noise as a function of frequency.

3. Experimental Methods

3.1 Cryogenics

The working temperature of MMCs is typically between 20 mK and 100 mK. To reach such low temperatures some effort is necessary and there are presently two well established techniques to achieve this. Dilution refrigerators and Adiabatic Demagnetisation Refrigerators (ADR). The experiments conducted during this thesis were mainly done in an ADR and the properties of this cryostat will be described briefly in the following section.

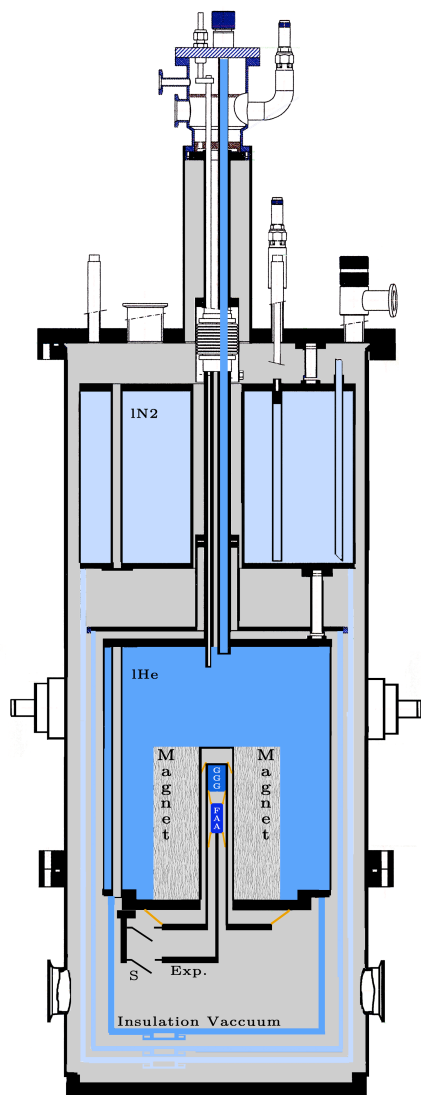


Figure 3.1 A schematic cross-section of the used adiabatic demagnetisation refrigerator. Grey shows the insulation vacuum while the different cooling stages are shown in different shades of blue—light blue is the warmest, dark blue the lowest temperature. Further information on the different stages and other parts in the text.

In figure 3.1 a cross section of the used ADR cryostat is shown. There are different temperature stages all separated by insulation vacuum. The first cold stage from room temperature (300 K) is the liquid nitrogen bath at 77 K followed by the liquid helium bath at 4.2 K. Connected to the helium bath there is an experimental plate. In addition it is possible to pump the helium bath to a few mbar to lower the temperature of the He bath to about 1.5 K.

The next cooling stages are achieved by adiabatic demagnetisation of two paramagnetic salt pills with individual experimental platforms which are fixed to the 4 K plate only by Kevlar strings with very low thermal conductivity. The first one is made of Gadolinium Gallium Garnet¹ (GGG) and serves as additional heat sink for the lowest temperature salt pill made of Ferric Ammonium Alum² (FAA).

The pills are in the bore of a superconducting magnet which can be loaded to a maximum current of about 36 A creating a field of about 6 T. The degenerate magnetic moments of the paramagnetic pills undergo a Zeeman splitting in the magnetic field. When the Zeeman splitting becomes larger than the thermal energy, $g\mu_B B > k_B T$, the lower states become more favourable therefore reducing the entropy S of the system. The release of heat can be absorbed by the He bath through a thermal link connecting the pills to the bath provided by a mechanical heat switch.

After thermal equilibrium is reached again, the pills are disconnected from the bath and the current from the magnet can be ramped down slowly keeping the demagnetisation adiabatic³. The Zeeman splitting becomes smaller, more states become available and are occupied taking energy out of the phonon system therefore reducing the temperature.

The lowest base temperatures with the cryostat used in this work are about 250 mK for the GGG and 21 mK for the FAA pill.

Magnetic cooling is not continuous, therefore, once the lowest temperature is reached the cryostat starts to warm up until a new cooling cycle from He bath temperature is started again. The temperature can be manipulated by changing the current in the superconducting coil. By regulating this current the temperature of the experimental plate can be kept constant at the level of $2 \mu\text{K}$.

3.2 Superconducting Magnetometer

The signal created in an MMC is a change of magnetic flux. Therefore a highly sensitive device for measuring flux is necessary and SQUIDS fulfil these conditions in the best known way nowadays. SQUIDS make use of quantisation of magnetic flux in closed superconducting loops in multiples of the magnetic flux quantum Φ_0 [Bar57] in combination with the Josephson-effect [Jos62]. There are two types, rf(radio frequency)-SQUIDS and dc(direct current)-SQUIDS. In the following sections the operation of dc-SQUIDS as used in this work will be further described.

¹Gd₃Ga₅O₁₂

²Fe₂(SO₄)₃(NH₄)₂SO₄ · 24H₂O

³therefore always keeping the Zeeman and the phonon system of the pills in thermal equilibrium

3.2.1 dc-SQUID

A dc-SQUID consists of a superconducting loop with thin insulating barriers (so-called Josephson junctions) at two points of the loop. Additionally there are two so-called shunt resistors in parallel to the junctions which prevent hysteretic behaviour of the device (figure 3.2). If a bias current I_b is flowing through a SQUID the current carrying Cooper pairs can tunnel through the Josephson junctions (Josephson effect [Jos62]) without losing their coherence until a critical current I_c is reached. If I_c is exceeded the SQUID enters the so-called resistive mode and quasiparticles (single electrons) start tunnelling through the barriers and a voltage drop starts to appear over the SQUID.

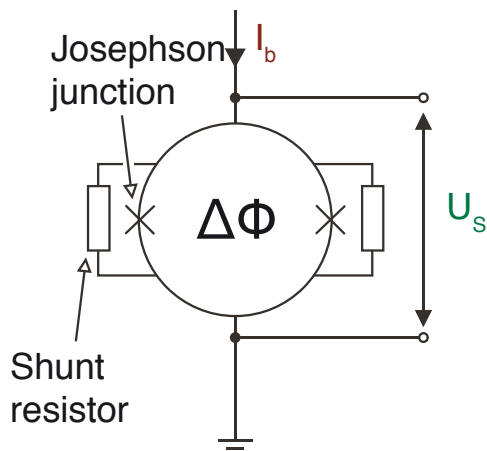


Figure 3.2 Schematic of a dc-SQUID showing the Josephson junctions and the parallel shunt resistors. The magnetic flux Φ , the bias current I_b and the measured voltage drop U_s are shown as well.

If a magnetic flux is applied to a SQUID, it can penetrate into the SQUID through the Josephson junctions. Since magnetic flux is quantised to even multiples of the magnetic flux quantum Φ_0 in superconducting loops, the applied flux influences the voltage drop in the resistive regime. It is also due to the quantisation condition that the magnetic flux dependency of the voltage drop is periodic with Φ_0 .

This periodic behavior of the voltage-to-flux characteristic is shown in figure 3.3 as well as the voltage drop plotted against the injected bias current I_b for the type of SQUIDs used in this thesis [Por07].

As can be seen in figure 3.3 the $U - \Phi$ characteristic is highly non-linear and can only be accounted as linear for about $0.25 \cdot \Phi_0$. There are efforts to build SQUIDs with a linear regime of about $0.72 \cdot \Phi_0$ [Bey09], but in order to have a longer linear range flux feedback to the SQUID loop is used. This consist in trying to keep the flux in the SQUID at a constant value. The schematic of the so-called flux-locked-loop circuit is shown in figure 3.4. The voltage drop U_s over the SQUID is compared to a reference voltage U_b that defines the working point of the SQUID and should be selected in the steepest regime of the $U - \Phi$ curve. If U_s differs from U_b the amplifier sends a voltage signal proportional to the difference to an integrator. The voltage output of the integrator is applied on a feedback resistor R_{fb} and the resulting current is sent through a feedback coil on the SQUID chip and therefore compensates the initial flux change. Furthermore the voltage output of the integrator across the

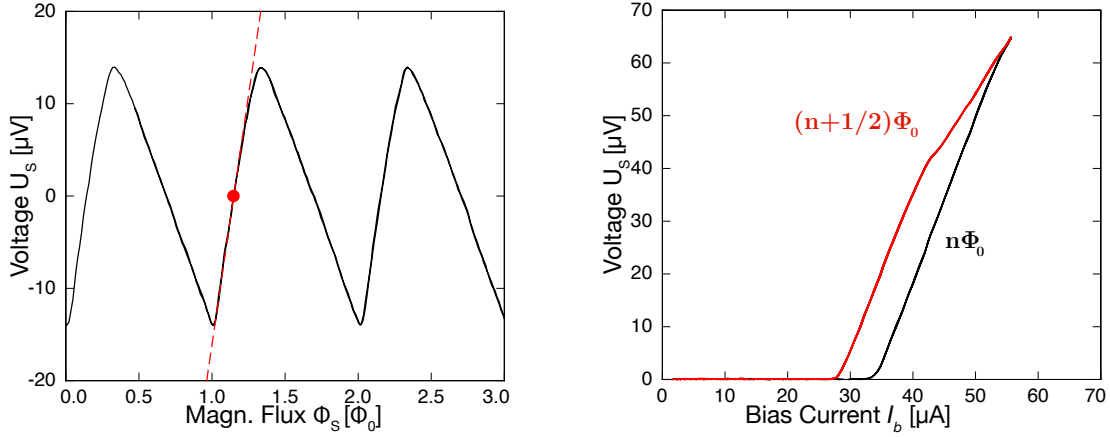


Figure 3.3 The measured characteristics of a MagCal SQUID [Por07]. On the left the $U - \Phi$ characteristic and on the right the $U - I$ characteristic.

feedback resistor is measured and can be calculated back to the initial flux change using the feedback resistance R_{fb} and the mutual inductance M_{fb} of the feedback loop:

$$\Delta\Phi = U_{out} \frac{M_{fb}}{R_{fb}} \quad (3.1)$$

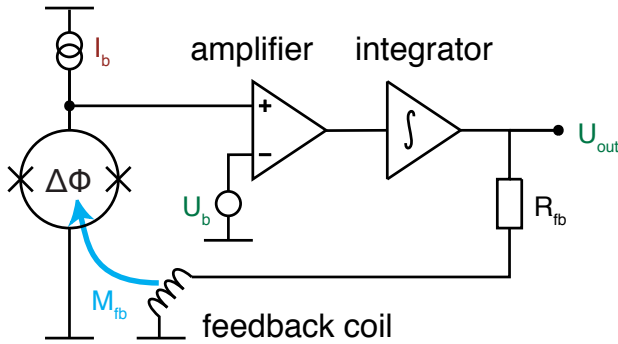


Figure 3.4 Schematic of the single stage flux locked loop setup.

3.2.2 Two-stage Configuration

In the previous section the single stage configuration of a SQUID read out was described. But using a second SQUID or SQUID array as a low-noise amplifier offers some advantages, e.g. lower noise due to the room temperature amplifiers and readout electronics and lower power dissipation on the detector SQUID as will be described in the following.

Figure 3.5 shows a schematic of a two-stage SQUID setup. On the left the detector SQUID is shown in series with the input coil of the second SQUID. Both together are connected in parallel to a small gain resistor R_g therefore acting as a current divider for the bias current I_b with the dynamic resistance R_1 of the detector

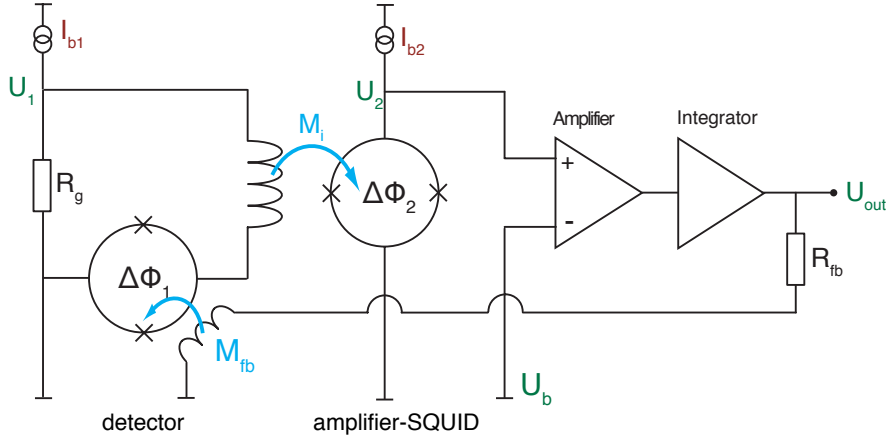


Figure 3.5 Schematic of the two-stage flux locked loop setup.

SQUID, providing a voltage bias rather than a current bias for the first stage SQUID. Since the secondary SQUID acts as a current detector for the current flowing through the primary SQUID, the gain resistor R_g should be chosen in the order of the dynamic SQUID resistance R_1 or smaller, so that the current changes

$$\delta I_1(\delta\Phi_1) = I_b \left(1 + \frac{R_1(\delta\Phi_1)}{R_g} \right)^{-1}. \quad (3.2)$$

are maximised. This results in a flux change $\Delta\Phi_2$ in the amplifier SQUID:

$$\delta\Phi_2 = \delta I_1 M_i \quad (3.3)$$

with the mutual inductance M_i between the secondary SQUID and its input coil. The amplifier SQUID is now operated in the flux-locked-loop mode as described in the previous section except that the feedback current $I_{fb} = U_{out}/R_{fb}$ is injected into the feedback coil with the mutual inductance M_{fb} to the first stage SQUID and is now compensating the change of flux in this first stage or detector SQUID.

Another important quantity that should be defined is the flux-to-flux amplification:

$$G_\Phi = \frac{\partial\Phi_2}{\partial\Phi_1} = M_i \left(\frac{\partial I_1}{\partial\Phi_1} \right)_{R_g, I_b}. \quad (3.4)$$

G_Φ strongly influences the noise contribution of the secondary SQUID, possibly being dominated by the room temperature electronics and if $G_\Phi > 1$ this contribution to the detector SQUID noise becomes lower. On the other hand the use of a two-stage configuration can influence the power dissipation on the silicon chip carrying the detector SQUID and the experiment and therefore allowing the sensor to stay at a lower temperature since the experiment is located on the used SQUID chip itself.

The used detector SQUID MagCal Nr. 15 is further described in chapter 3.4. The used amplifier SQUID is a 16 SQUID array⁴ connected in series, where the voltages add up coherently, which leads to a slope at the working point of about $1 \text{ mV}/\Phi_0$. The gain resistor R_g and the input coil of the amplifier SQUID are micro-structured directly on the chip resulting in a input coupling of about $1/M_i = 17.4 \mu\text{A}/\Phi_0$ and an intrinsic flux noise of $0.5 \mu\Phi_0/\sqrt{\text{Hz}}$.

3.2.3 Readout Noise

In this chapter the noise contributions of the read out circuit are discussed. This includes SQUID noise of detector $S_{\Phi,\text{det}}$ and amplifier SQUID $S_{\Phi,\text{amp}}$ and the effect of the room temperature readout electronics $S_{U,\text{el}}$

The origin of the intrinsic SQUID noise is the Johnson noise of the shunt resistors R in parallel to the Josephson junctions. The noise shows a temperature dependency and since Johnson noise is current noise, it is transformed into flux noise via the self inductance L_S of the SQUID.

Claudia D. Tesche conducted numerical calculations [Tes77] for intrinsic flux noise of optimised dc-SQUIDs and found the following approximate expression for the white noise level:

$$\sqrt{S_{\Phi}^{\text{SQUID}}} = \frac{\partial\Phi}{\partial U} \sqrt{S_U^{\text{SQUID}}} \simeq L_S \sqrt{16k_B \frac{T}{R}}, \quad (3.5)$$

where $\partial\Phi/\partial U$ is the slope of the voltage-to-flux characteristic.

Adding up all the white noise contributions in a two-stage SQUID setup, the apparent flux noise referred to the detector SQUID is:

$$S_{\Phi,w} = S_{\Phi,\text{det}} + \frac{4k_B T}{R_g} \left(\frac{M_i}{G_{\Phi}} \right)^2 + \frac{S_{\Phi,\text{amp}}}{G_{\Phi}^2} + \frac{S_{U,\text{el}}}{(\partial U_{\text{amp}}/\partial\Phi_{\text{amp}})^2 G_{\Phi}^2}, \quad (3.6)$$

with M_i the mutual inductance between the input coil of the second stage SQUID and the second stage SQUID itself, G_{Φ} the flux-to-flux amplification between the two SQUIDs. The first and third term show the contribution of the intrinsic noise of detector and amplifier SQUID, respectively, while the second term is caused by the Johnson noise of the gain resistor R_g and the fourth term describes the influence of the room temperature SQUID-electronics.

In addition to the white noise, SQUIDs show a $1/f$ -dependency in the intrinsic noise spectrum [Cla04]. Defects within the SQUID material seem to be the reason for this noise. First, thermal movement of trapped flux lines of vortices within the SQUID circuits, second, trapping and de-trapping of electrons within the Josephson junctions can cause variations of the critical current and can cause $1/f$ -noise. Third tunnelling systems in the dielectric layers can be a reason for $1/f$ -noise as well.

Typical values for the used SQUIDs are $\sqrt{S_{\Phi,\text{SQ},w}} \approx 1 \mu\Phi_0/\sqrt{\text{Hz}}$ white noise level and $\sqrt{S_{\Phi,\text{SQ},1/f}}|_{1\text{Hz}} \approx 7 \mu\Phi_0/\sqrt{\text{Hz}}$ for the $1/f$ contribution at 1 Hz.

⁴Type: C503E15 CX16FL designed by the Physikalisch-Technische Bundesanstalt (PTB), Berlin.

3.3 Calibration ^{55}Fe Source

For the characterisation of a detector it is useful to define its response upon a known deposition of energy to constrain the free parameters in the characterisation. One parameter is the energy that can be constrained by using an x-ray source with narrow spectral lines at known energies. In this work a ^{55}Fe source was used for this purpose.

^{55}Fe has a half-life of 2.75 a and undergoes an electron capture process to ^{55}Mn . The captured electrons originate mainly from the K -shell (88 %) while about 10 % come from the L -shell and the rest of about 2 % from the higher $M + N$ -shells. The resulting electron vacancies can be filled by higher shell electrons either by radiative x-ray or by Auger electron emission. The resulting electron and x-ray emission spectra are quite complex but well known.

The most intense x-ray lines are the K_α and K_β lines at mean energies of 5.895 keV and 6.505 keV respectively. The emission probabilities, relative to the total activity, are 25.4 % for the K_α and 1.99 % for the K_β transition. Additionally these lines show a fine structure extensively investigated by crystal spectroscopy e.g. in [Höl97].

Since the used sources are sealed in a stainless steel casing with a beryllium window about 200 μm thick the Auger electrons and the lower energy x-ray events are absorbed in the casing. The K_α and K_β x-ray events are the only expected emission lines, because the absorption length for 6 keV photons is about $\lambda = 2.4$ mm in beryllium.

3.4 Detector Design

3.4.1 Meander with Integrated dc-SQUID

The used detector SQUID is a MagCal Nr. 15⁵ shown schematically and microscopically photographed in figure 3.6. The SQUID combines a gradiometric meander geometry with the elements of a SQUID.

On a 2.5×2.5 mm² silicon chip four of these SQUIDs are located even though only one had been used at a time for an experiment. One SQUID consists of two gradiometrically coupled meander structures each consisting of 8 niobium stripes with 20 μm width and a 5 μm gap in between neighbouring stripes. Each meander covers an area of about 200×200 μm . In the middle between the two meanders are the two Josephson junctions located with the shunt resistors in parallel. The feed lines of the SQUID are connected in between the Josephson junctions and at one of the meanders. The feedback line is guided gradiometrically around the meander structures. Each supply line ends at the edge of the silicon chip in a bond pad to be connected via ultrasonic wedge bonding of 25 μm Al:Si wires to a circuit board (see following section).

In addition the double meander structure forms a closed superconducting loop and can therefore be prepared to carry a persistent current. For this purpose an

⁵Designed by V. Zakosarenko, R. Stolz and H. G. Meyer at the Institut für physikalische Hochtechnologie (IPHT), Jena.

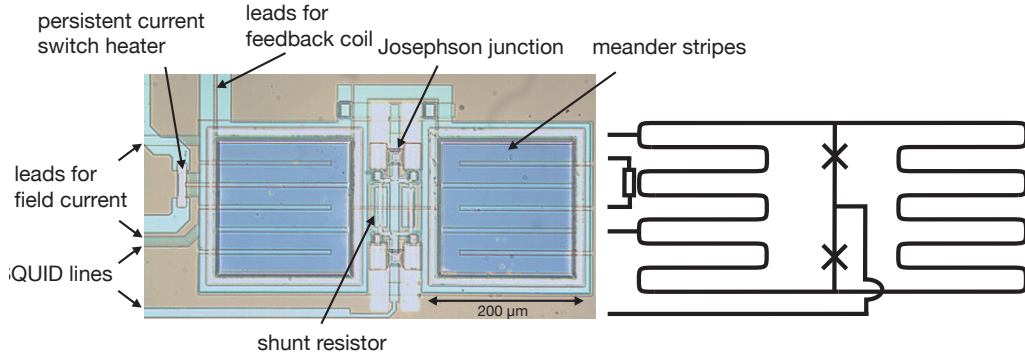


Figure 3.6 On the left a photo of a MagCal Nr. 15 SQUID and a schematic on the right without shunt resistors and feedback coil.

additional line is connected to one meander used to carry the field current together with one feed line of the SQUID, meeting two purposes. Secondly, a heater is needed to drive a part of the meander into the normal conducting state as can be seen in the schematic in figure 3.7.

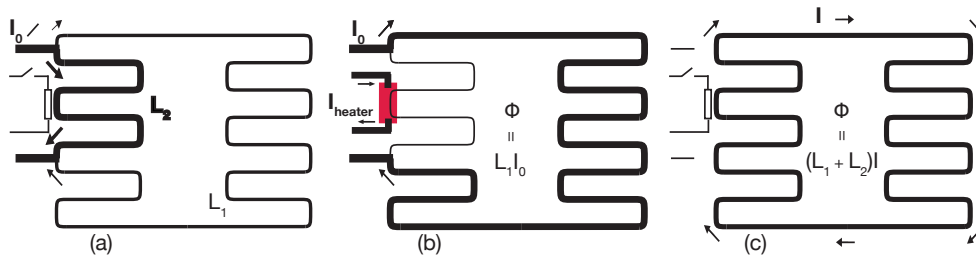


Figure 3.7 Schematic of the process of freezing a persistent current into a MagCal Nr. 15 meander in three steps described in the text.

In figure 3.7(a) the field current is driven through the field lines dividing accordingly to the inductance L_1 and L_2 therefore mainly flowing through L_2 according to flux conservation rules. In the second step (3.7(b)) a current is driven through the heater driving a part of L_2 normal conducting. Since L_2 has now a non-zero resistance the field current will flow through L_1 and the flux can penetrate the loop as it is not a closed superconducting any more. As the heater is switched off again (3.7(c)) L_2 becomes superconducting again closing the meander loop and the current will “permanently” flow through the loop. Because of flux conservation in closed superconducting loops the current in the loop will become a little smaller than the injected current I_a after switching of the external current supply, according to the now higher inductance leading to a finally stored persistent current I

$$L_1 I_0 = \Phi = (L_1 + L_2) I \quad (3.7)$$

$$\Leftrightarrow I = \frac{L_1}{L_1 + L_2} I_0. \quad (3.8)$$

This fact needs to be kept in mind if experimental data is compared with theory.

Comparing the size of L_1 and L_2 leads to the estimate

$$L_1 \approx 3 \cdot L_2 \Rightarrow I \approx \frac{3}{4} I_0. \quad (3.9)$$

3.4.2 Detector Setup

During this thesis two nearly identical detectors were examined. The difference is the material of the $50 \mu\text{m}$ thick superconducting absorbers. One made of high purity aluminium the other made of aluminium doped with 2000 ppm of manganese. To create the Al:Mn alloy the metals were melted in the desired ratio and subsequently annealed just below the melting point to assure a homogeneous distribution of the manganese atoms. Afterwards the alloy was quickly quenched to keep the homogeneous, purely statistical distribution of the manganese atoms within the aluminium [Boa64].

For preparing the absorbers both materials, Al and Al:Mn, were rolled into a thin foil of about $50 \mu\text{m}$ thickness and subsequently etched in NaOH to clean it from any contamination. Afterwards a sticking layer of 50 nm copper was sputter deposited on top of one side of the foil to enhance gold adhesion. The next step was the deposition of $4 \mu\text{m}$ of gold as spacer layer followed by a sensor layer of $3 \mu\text{m}$ of Au:Er. The sensor consisted of Au:Er with a concentration of 780 ppm erbium ions in the natural isotope abundance.

The prepared foils were cut in squares of about $200 \times 200 \mu\text{m}$ with a razor blade and glued onto the one of the two meanders that does not contain the persistent current switch heater of a MagCal Nr. 15 with a low temperature suitable two component epoxy glue⁶. The absorber was mechanically pressed on the meander with a ceramic indenter to ensure the lowest possible distance between sensor and meander.

The complete experimental setup can be seen in figure 3.8. The chip is glued on a $12 \times 30 \text{ mm}$ brass experimental holder next to a circuit board with copper lines designed for the feed lines of the chip. The connections between the two are established by $25 \mu\text{m}$ thick Al:Si bonding wires. Since the field and heater lines need to carry rather large currents, up to 150 mA, the conductors in the cold part should be completely superconducting to minimise parasitic heating. Therefore $100 \mu\text{m}$ thick Nb:Ti multi-filament wires in a Cu:Ni matrix are led through in a hole in the experimental holder and fixed with epoxy glue⁷. The endings are filed and the cross

⁶STYCAST 1266 A/B by Emerson & Cuming

⁷STYCAST 2850 by Emerson & Cuming

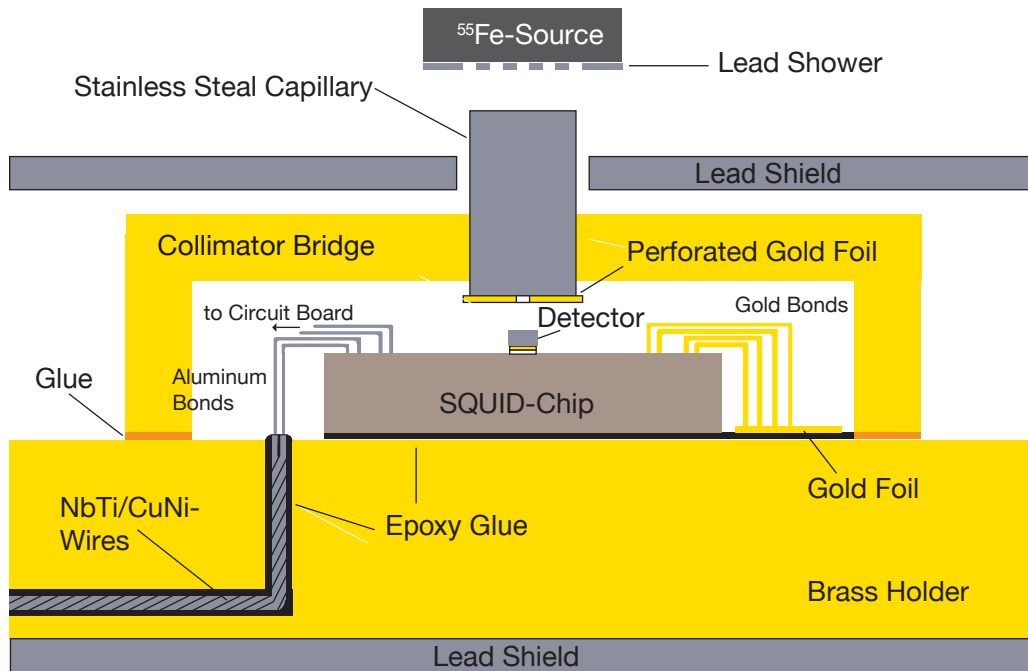


Figure 3.8 A cross section of the complete setup. The different parts are further described in the text.

sections can therefore be used as bond pads. Using aluminium bonding wires which become superconducting at 1.15 K a completely superconducting connection can be established.

To enhance the thermal conductivity from the chip to the brass holder additional gold wires were wedge bonded from unused bond pads on the chip to the brass holder. This way the chip temperature, that is normally higher than the bath temperature because of the SQUID's power dissipation, can be greatly reduced.

To make sure that the photons only hit the absorber and not the substrate a collimator consisting of a "bridge" made of brass, a stainless steel capillary and a gold foil with a hole of about $100\ \mu\text{m}$ in diameter was glued⁸ to the brass holder and fixed above the setup.

The complete setup was put into a lead casing which becomes superconducting at a temperature of 7.2 K and therefore protects the detector from fluctuating external magnetic fields.

Above the stainless steel capillary the ^{55}Fe source is positioned to irradiate the detector with x-rays. Because of the high activity of the source a part of it was covered to adjust the rate of x-rays reaching the detector.

3.4.3 Arrangement of the Wiring

To minimise the parasitic heat load to the experimental platform and to get a better understanding of the experimental setup it can be helpful to investigate the wiring

⁸The coil varnish GE Varnish 7031 was used.

further. Because of their good conduction properties the wires from room temperature to the 4 K plate are made of copper. They provide very good electrical conductance but thermal conductance as well. Therefore the wires are attached to the different temperature stages, LN_2 at 77 K, an additional radiation shield at about 20 K and ^4He at about 2 K, as heat sink. At the 4 K plate the wires are changed to Nb:Ti wires in Cu:Ni matrix which become superconducting at 9.8 K and therefore have perfect electrical conductivity and the thermal conductivity is reduced. The superconducting wires are linked to the heat sink again at the intermediate GGG stage at about 300 mK and then led to the amplifier and detector SQUIDs at the lowest temperature on the experimental platform at the FAA plate.

The wires are prepared as twisted triples for the 3-wire-measurement of the SQUIDs and as twisted pairs for the other operational currents to minimise parasitic interference of external magnetic fields.

3.4.4 Thermometry and Data Acquisition

To properly characterise a detector the performance should be tested at different temperatures and therefore it is necessary to know them precisely. Therefore resistance thermometers are installed at every temperature stage of the cryostat. The thermometers are read out by an AVS-47⁹ resistance bridge. The most important one, since it is used to measure and stabilise the temperature of the experiments, is a RuO thermometer installed at the FAA experimental platform with a $d \log(R)/d \log(T)$ of about -1.5 at 30 mK and a measurement uncertainty of about $2 \mu\text{K}$.

The voltage drop over the amplifier SQUID is measured, amplified and linearised by a SQUID electronic¹⁰. The signal is split into two channels and further amplified by low noise preamplifiers¹¹ acting also as filters. One channel acts as trigger channel. In this channel the signal is heavily filtered in order to precisely detect the starting of the signal. When a voltage value, higher than a preset value, is measured in the trigger channel, the data set coming from the second channel, which has a limited filtering, is recorded by the acquisition program.

This is obtained using an analogue-to-digital converter oscilloscope card¹² with 16384 samples and 12 bit resolution.. Normally a quarter of the samples is recorded prior to the trigger to have information on the baseline prior to the pulse. After a fast on-line analysis done by the acquisition program, important to directly understand the quality of the measurement, the data is stored in files and will be used for more refined off-line analysis.

⁹Manufactured by Pico-Watt Electronica, Finland <http://www.picowatt.fi>.

¹⁰Manufactured by MagniCON, Germany <http://www.magnicon.com/>.

¹¹SRS-560 by Stanford Research Systems, USA <http://www.thinksrs.com/>.

¹²GAGESCOPE 8012A, manufactured by GaGe, USA <http://www.gage-applied.com/>.

4. Metallic Magnetic Calorimeters: Experimental Results

In this chapter the experimental results obtained with the two MMC experiments will be described. One with a $50\ \mu\text{m}$ thick high purity aluminium absorber the other one with a $50\ \mu\text{m}$ thick absorber made of aluminium doped with 2000 ppm manganese.

First the results of the same type of measurements done for both detectors are described together, followed by sections describing observations made at one of the detectors, starting with the Al detector followed by the Al:Mn detector.

4.1 Magnetic Flux Noise at Low Temperatures

In chapter 2.5.2 the expected noise contributions for a MMC were explained. In the following the expectations described there will be compared with the observations during these measurements.

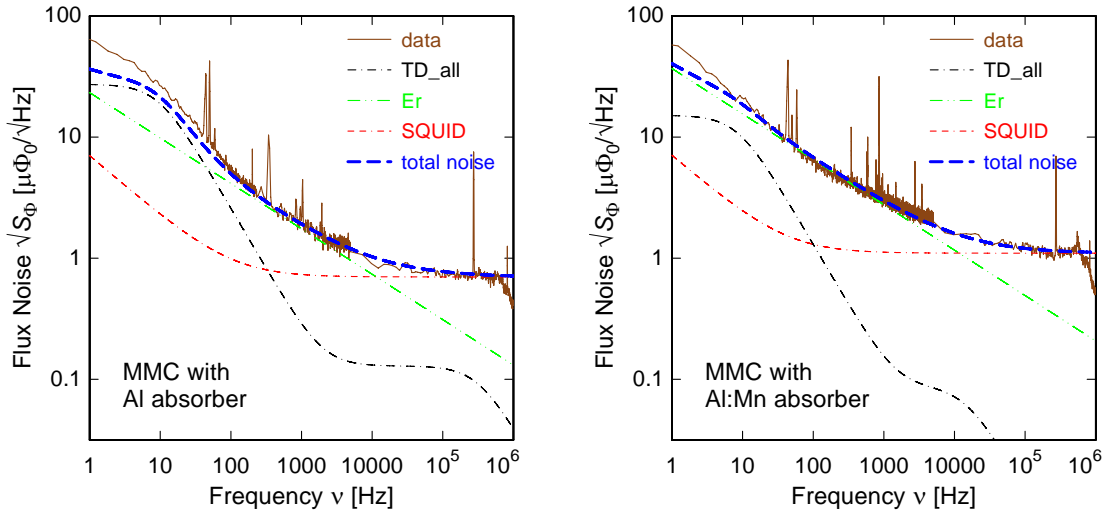


Figure 4.1 Left: A Noise spectrum of the Al detector with a field current of $I = 100\ \text{mA}$ at $T = 37\ \text{mK}$.

Right: A Noise spectrum of the Al:Mn detector with a field current of $I = 35\ \text{mA}$ at $T = 32\ \text{mK}$.

The theoretically expected noise contributions are shown in different kinds of dashed lines. The contributions are further described in the text.

Figure 4.1 shows spectra of the measured flux noise in the detector SQUID of the Al and the Al:Mn detector at low temperatures. The spectra were obtained by a Fourier transformation of digitised time windows of the detector signal in the absence of x-ray events, e.g. in between triggered signals, so-called baselines. For each spectrum three different time-windows lengths – $0.4\ \text{ms}$, $80\ \text{ms}$ and $1.6\ \text{s}$ – were

recorded covering a frequency range from about 1 Hz to 1 MHz. Using these baselines for creating a noise spectrum is very useful because it is possible to do an off-line rejection of not perfect baselines and baseline tracks, when small pulses are present. This rejection should be done since pulses are influencing strongly the low frequency part of a noise spectrum. Without pulse rejection it would normally be impossible to do a proper analysis of the low frequency noise, when an x-ray source is installed in the cryostat, irradiating the detector.

The three time windows are necessary to cover the whole frequency range. This is because the lowest frequency to be obtained by Fourier transform is limited by the length of the time window Δt resulting in $\nu_{\min} = 1/\Delta t$. The the highest frequency is limited by the Nyquist–Shannon sampling theorem [Sha49] resulting in $\nu_{\max} = 16384/(2\Delta t)$ if 16384 points are sampled within the time window.

Starting from high frequencies a white noise level can be seen with a value of $\sqrt{S_{\Phi}} = 0.7 \mu\Phi_0/\sqrt{\text{Hz}}$ for Al and $\sqrt{S_{\Phi}} = 1.1 \mu\Phi_0/\sqrt{\text{Hz}}$ for Al:Mn with a cut-off frequency of about 1 MHz which is the achieved bandwidth of the used read-out scheme. With the observed bandwidth the time resolution is limited to $\tau = (2\pi\nu_{\text{cut}})^{-1} \approx 160 \text{ ns}$ which is faster than all observed rise times.

At frequencies below 10 kHz the other contributions become dominant. First the contributions of the erbium ions calculated with eq. 2.51. In the configuration of the experiments a different frequency dependence $S_{\Phi, \text{Er}}(\nu) \propto \nu^{-0.75}$ and a smaller contribution of $S_{\Phi, \text{Er}}(1 \text{ Hz}) = S_{\Phi, \text{Er, theo}}(1 \text{ Hz})/2.5$ for the Al detector was observed while the level at 1 Hz is the same as calculated for the Al:Mn detector. The different frequency dependency was observed earlier [Pab08, Bur08, Pie08] while the lowered noise level shows once more that this particular noise contribution is not well understood (see chapter 2.5.2). Additional confusion is caused by the fact that the noise of the similar processed detectors with Al and Al:Mn absorber show different noise levels. An explanation can be the glue layer between meander structure and sensor (see chapter 3.4.2). Since the thickness is not well defined the distance between meander and sensor can deviate slightly. Therefore, the magnetic field distribution within the sensor might be different causing in turn a different coupling of the magnetic moments to the meander.

At frequencies below 100 Hz the thermodynamic fluctuations become dominant. The contributions were calculated using eq. 2.50 inserting the experimentally observed main rise and decay time of $\tau_{\text{rise, Al}} = 0.5 \mu\text{s}$ and $\tau_{\text{decay, Al}} = 16.8 \text{ ms}$ for the Al and $\tau_{\text{rise, Al:Mn}} = 11 \mu\text{s}$ and $\tau_{\text{decay, Al:Mn}} = 18.5 \text{ ms}$ for the Al:Mn detector.

The last low frequency contribution, the $1/f$ part of the read out noise of about $\sqrt{S_{\Phi, \text{SQUID}}|_{1 \text{ Hz}}} = 7 \mu\Phi_0/\sqrt{\text{Hz}}$ needs to be mentioned but has not much influence since the earlier mentioned contributions of the erbium ions and the thermodynamic fluctuations are much higher.

As can be seen in figure 4.1 the incoherent sum of the described noise contributions fits very well to the measured spectrum with a few exceptions. There are some peaks for example at 50 Hz that are originating from external noise sources like the power supply system or other external sources coupling magnetically to the setup.

Another slight deviation can be seen at frequencies below about 10 Hz which

might be explained by slightly higher thermodynamic fluctuations due to infrared radiation to the detector or an additional noise contribution with the spectral shape $S_\Phi \sim 1/f$.

4.2 Magnetisation Measurements

To characterise both detectors three different currents were injected and frozen into the meander structure, 50 mA, 100 mA, 150 mA. The freezing of the field was followed by a measurement of the magnetisation change with temperature from about 1.8 K to 23 mK. The data obtained in these measurements are shown in figure 4.2.

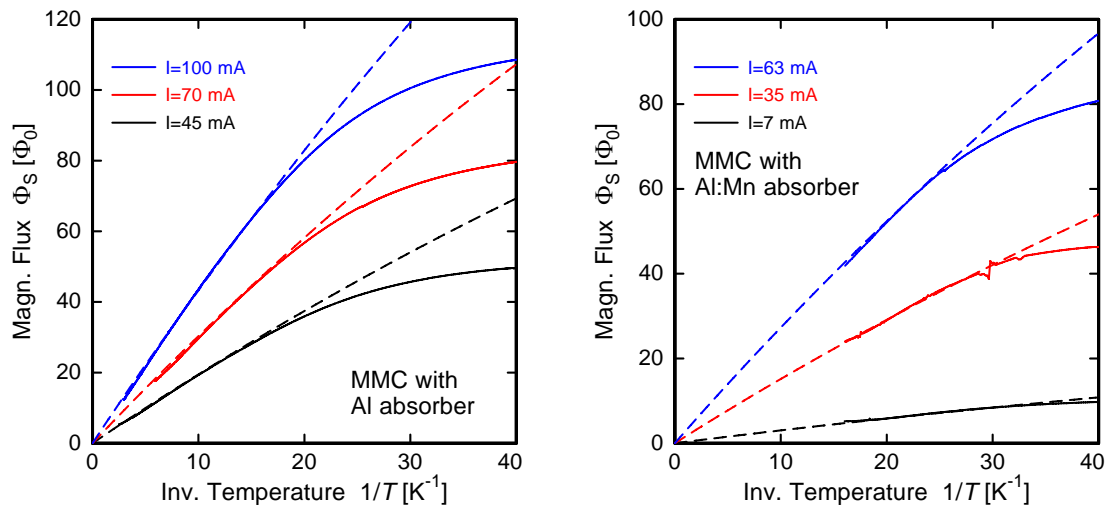


Figure 4.2 The magnetisation measurement (solid lines) plotted against the inverse bath temperature $1/T$ compared with theory (dashed lines) for three different currents for the Al (left) and Al:Mn (right) detector.

By fitting the experimental data to the calculated magnetisation for different persistent currents it is possible to get a better estimate of the actual frozen current since this is previously just estimated with $0.75 \cdot I_0$ (see chapter 3.4.1). The following correspondences were found for the Al detector: 50 mA \rightarrow 45 mA, 100 mA \rightarrow 70 mA and 150 mA \rightarrow 100 mA. The freezing of $I_0 = 150$ mA did not work for the Al:Mn detector and only a residual field was present and still enough to measure some magnetisation change. The following frozen currents were identified: 50 mA \rightarrow 35 mA, 100 mA \rightarrow 63 mA, 150 mA \rightarrow 7 mA.

But this fitting is only possible in the higher temperature range above about 100 mK, as the experimental data and theory agree very well in this range. At lower temperatures the measurement differs from theory (fig. 4.2). This is because of the SQUID's power dissipation, which keeps the chip and therefore the sensor warmer than the bath. Using the theory it is possible to estimate the sensor temperature from the magnetisation measurement and therefore a temperature correction curve

can be extracted like in figure 4.3 by plotting the bath temperature against the sensor temperature.

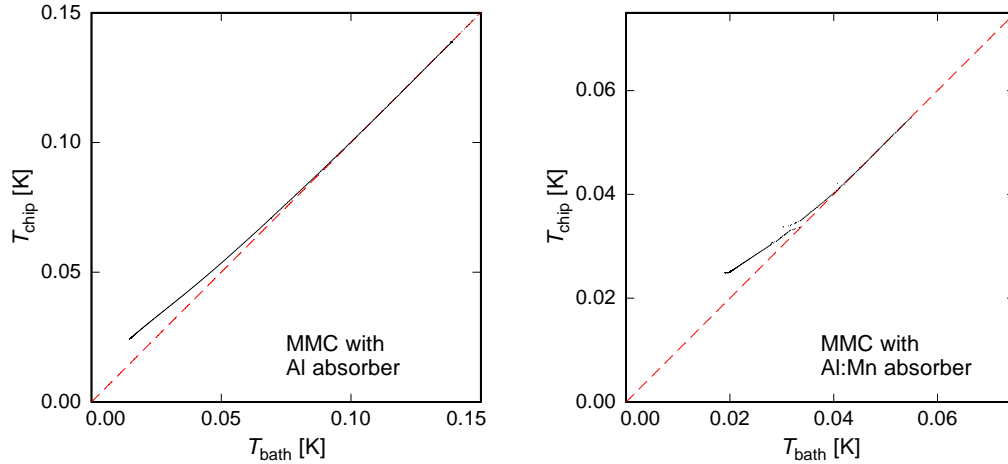


Figure 4.3 The temperature correction curves obtained from the measured magnetisation for the Al (left) and AlMn (right) detector.

This temperature correction can become very important when analysing properties which depend on the sensor temperature, since the difference can be as large as 25 % at lowest bath temperatures.

4.3 Spectrum

In order to characterise the detector response upon the absorption of ionising radiation, both detectors were irradiated with x-rays of an ^{55}Fe source as described in section 3.4.2. In a simple thermodynamic model as for example described in chapter 2.5.1 all recorded signals of a detector should show the same qualitative time evolution, independent of the deposited energy. Therefore it should be possible to find a reference pulse $r(t)$ and every recorded pulse $s(t)$ could be fitted to that reference pulse by stretching by an amplitude A and adding a constant offset A_0 . This way the sum of quadratic deviations $\chi^2 = \sum_i (s(t_i) - A \cdot r(t_i) + A_0)^2$ can be defined for a finite number of samples i . The χ^2 provides a quantity that shows how similar two pulses are.

Figure 4.4 shows the χ^2 of each recorded event plotted against its amplitude A . The events at low amplitudes are most likely to be substrate events, where x-ray photons hit the silicon substrate and not the aluminium absorber due to imperfect collimation. Another interesting group of data points is found at amplitudes around $A = 1$ where four different “isles” of data points can be seen. The events with $\chi^2 < 1 \cdot 10^{-4}$ and $A \simeq 1$ were used as reference pulse and were identified as K_α events of the ^{55}Fe source with an energy of $E = 5.9 \text{ keV}$ absorbed in the superconducting aluminium absorber. They can be discriminated by looking at the ratio of total number of events in the different isles. Centred around $A = 1.1$ are the K_β events

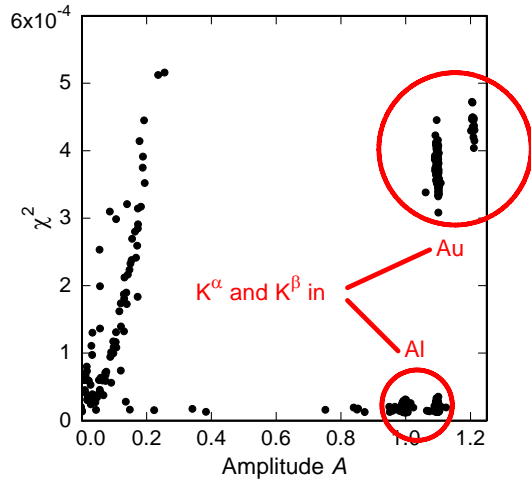


Figure 4.4 The χ^2 plotted against the amplitude A for acquired pulses obtained with the Al detector with $I = 100$ mA at $T = 37$ mK. An average of the K_α pulses absorbed in the aluminium absorber were used as reference pulse $r(t)$. Of special interest are the four different kinds of pulses, K_α and K_β absorbed in aluminium and gold respectively which are marked by the two circles.

with an energy of $E = 6.5$ keV. At a slightly higher χ^2 of about $4 \cdot 10^{-4}$ and at amplitudes around $A = 1.1$ and $A = 1.2$ two additional “isles” can be seen that can be identified with the K_α and K_β events absorbed in the gold spacer layer below the aluminium absorber.

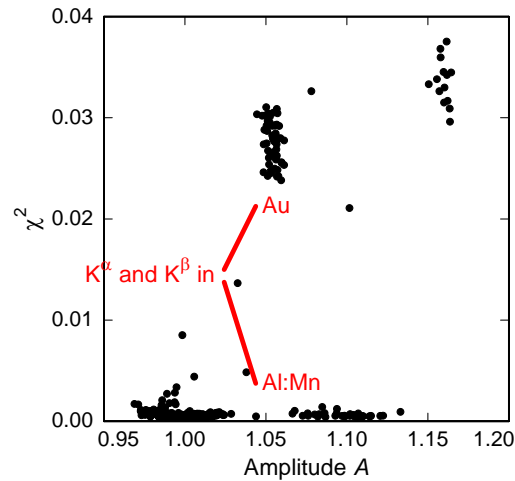


Figure 4.5 The χ^2 plotted against the amplitude A for acquired pulses obtained with the Al:Mn detector with $I = 35$ mA at $T = 32$ mK.

Figure 4.5 shows the χ^2 versus amplitude plot for K_α and K_β events in the detector with Al:Mn absorber. We can find exactly the same features except that the χ^2 of the events absorbed in the gold layer are higher for the Al:Mn detector than for the Al detector. The reason for this difference will become obvious in section 4.6.1 when the shape of the corresponding detector signals on short time scales will be discussed.

4.4 Energy Resolution

One of the most important properties of a detector is its energy resolution defined as the full width at half of the maximum (FWHM) of a measured mono-energetic line. Even though the experiments in this work did not aim for the best energy resolution possible, it is interesting to discuss the lower limit of energy resolution achieved in this work using MMCs with superconducting absorber.

Taking into account the heat capacity of the detector as discussed in section 4.5.2, the working temperature and the theoretically expected detector noise from section 4.1, the expected energy resolution can be calculated to be $\Delta E_{\text{FWHM}} = 4.8 \text{ eV}$ at its best for the Al detector.

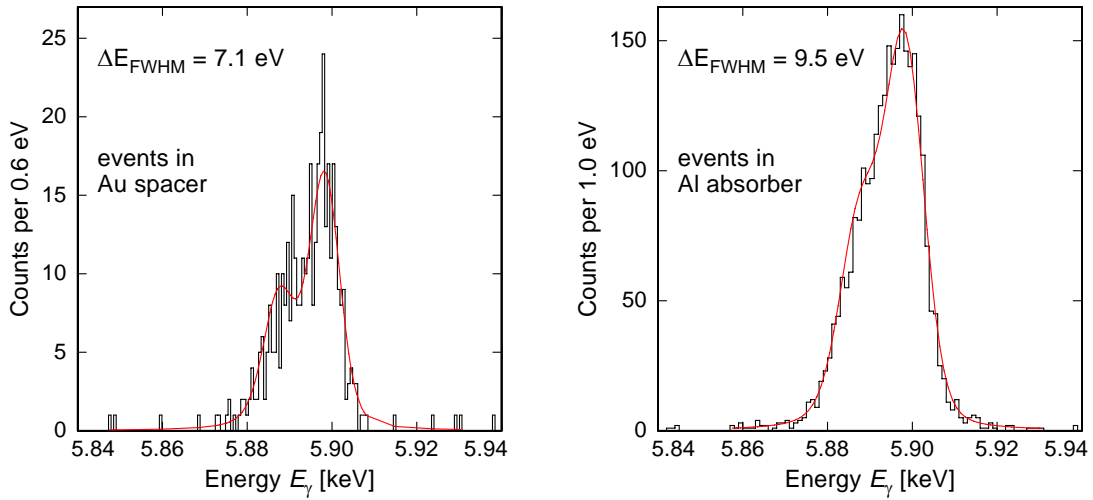


Figure 4.6 Measured line shape of the K_α line of ^{55}Mn (histogram) as derived from events absorbed in the Au spacer (left) and the superconducting Al absorber (right). The smooth solid line in both plots represents a fit to the data, being a convolution of the natural line shape and a Gaussian distribution of width $\Delta E_{\text{FWHM,Au}} = 7.1 \text{ eV}$ (Au events) and $\Delta E_{\text{FWHM,Al}} = 9.5 \text{ eV}$ (Al events), respectively.

In case of the Al detector there are three types of events or detector signals from which an energy spectrum and therefore an energy resolution can be derived. These in turn can be compared to the expected one: The line-width of the 5.9 keV K_α photons absorbed in aluminium and gold respectively, and the distribution of energies around zero that can be obtained by applying the analysis algorithm to untriggered detector signals, so-called baselines.

Figure 4.6 shows the two K_α lines extracted from the measured events that are absorbed in the Al absorber and the gold spacer respectively. The spectrum was taken at a bath temperature of $T = 30 \text{ mK}$, which corresponds to a chip temperature of about $T_{\text{chip}} = 37 \text{ mK}$, and with a frozen current of $I = 100 \text{ mA}$. The temperature was stabilised with a PID controller.

The K_α line of ^{55}Mn shows a finite line-width of about 2.5 eV and a fine structure

splitting of 12 eV. In order to derive the energy resolution of the detector from the measured line shape, it was fitted by a convolution the natural line shape with a Gaussian distribution with variable line-width. The result of this fit represents the line width of the detector.

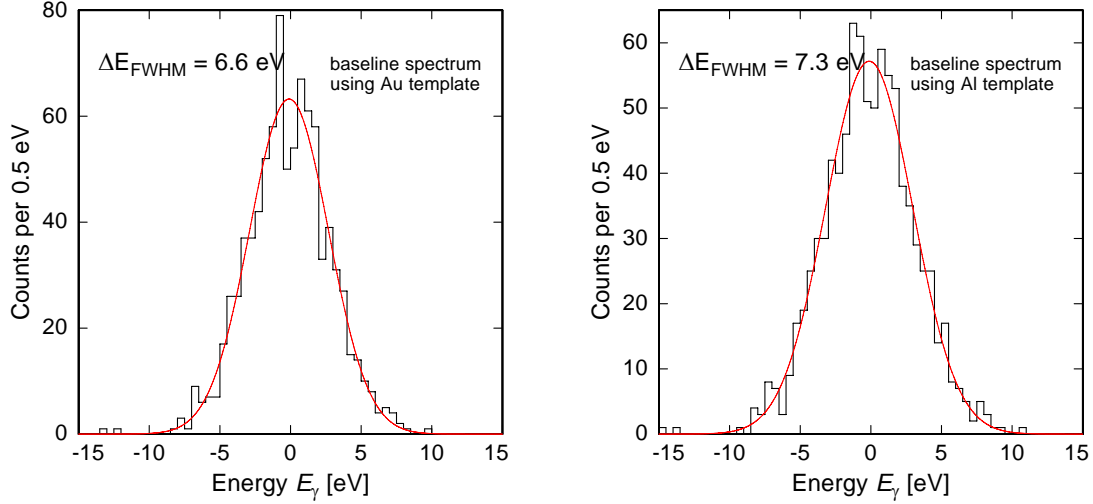


Figure 4.7 The baselines extracted from the measured spectrum. The resulting line shape depends slightly on the averaged pulse used to fit the spectrum. Therefore the baseline distribution using the gold pulse for fitting is shown on the left with an energy resolution of $\Delta E_{\text{FWHM}} = 6.6 \text{ eV}$. The right plot shows the result of $\Delta E_{\text{FWHM}} = 7.3 \text{ eV}$ obtained using the pulses absorbed in aluminium as average.

Before discussing the observed energy resolution at 5.9 keV photon energy, we look at the measured energy resolution at 0 keV photon energy as derived from untriggered detector signals. The baselines were analysed in two ways, using the average of the K_α events in Al and in the Au spacer, respectively, because the resulting energy spectrum depends slightly on the averaged pulse used for the fitting routines. Therefore figure 4.7 shows the baseline distribution obtained using K_α pulses absorbed in both aluminium and gold for the fit.

The obtained energy resolutions for 5.9 keV photons are $\Delta E_{\text{FWHM,Au}} = 7.1 \text{ eV}$ for the events absorbed in gold and $\Delta E_{\text{FWHM,Al}} = 9.5 \text{ eV}$ for the events absorbed in aluminium. It is interesting to compare the corresponding baseline width of $\Delta E_{\text{FWHM,Base,Au}} = 6.6 \text{ eV}$ using the gold average and $\Delta E_{\text{FWHM,Base,Al}} = 7.3 \text{ eV}$. The difference between the two baseline widths can be accounted to the slightly different shape of the pulses absorbed in aluminium and gold.

For the events absorbed in the Au spacer the resolution of the baselines and for 5.9 keV photons both values are quite similar and the difference can be accounted for example to not enough statistic for the gold events or a possible low energy tail due to the escape of high energy phonons to the substrate. Higher statistics would give more certainty to the obtained value but it is hard to achieve since only less than 20 % of the total K_α events pass the aluminium and are absorbed in the gold.

The deviation to the theoretically expected value of 4.8 eV can for example be due to additional lines in the noise spectrum at discrete frequencies (see section 4.1) or the finite temperature stability of the experimental platform and the sensor.

The linewidth for 5.9 keV photons in aluminium is broadened significantly compared to the energy resolution at 0 keV. The possible reasons for the broadening can be for example dependence of the signal size on the position of the absorption within the Al absorber due to different thermal diffusion times, a statistical uncertainty of the number of broken Cooper pairs and therefore created quasiparticles or the reasons mentioned in the discussion of the gold events.

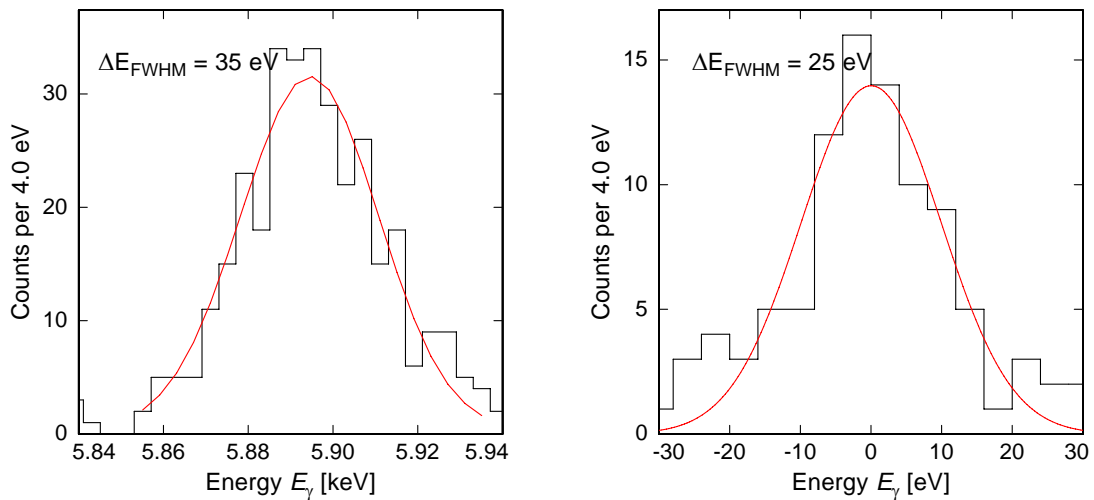


Figure 4.8 Spectra of the K_α line of ^{55}Mn as measured with the Al:Mn detector showing a resolution of $\Delta E_{\text{FWHM,Al:Mn}} = 35$ eV for the events absorbed in the absorber (left) and $\Delta E_{\text{FWHM,Base}} = 25$ eV for the baselines (right).

As the energy resolution of the Al:Mn detector was found to be significantly worse than the one of the Al detector no spectrum with high statistics was recorded. But taking one of the characterisation measurements for determining the energy resolution the spectrum shown in figure 4.8 was obtained. It was measured at $T = 32$ mK with a frozen current of $I = 32$ mK. The estimated energy resolution was $\Delta E_{\text{FWHM}} = 11$ eV while the measured one was $\Delta E_{\text{FWHM,Al:Mn}} = 35$ eV for the events absorbed in the Al:Mn absorber and $\Delta E_{\text{FWHM,Base}} = 25$ eV for the baselines. The resolution of the events absorbed in gold was not determined because of much too low statistics.

4.5 50 μm Al detector

4.5.1 Signal Shape

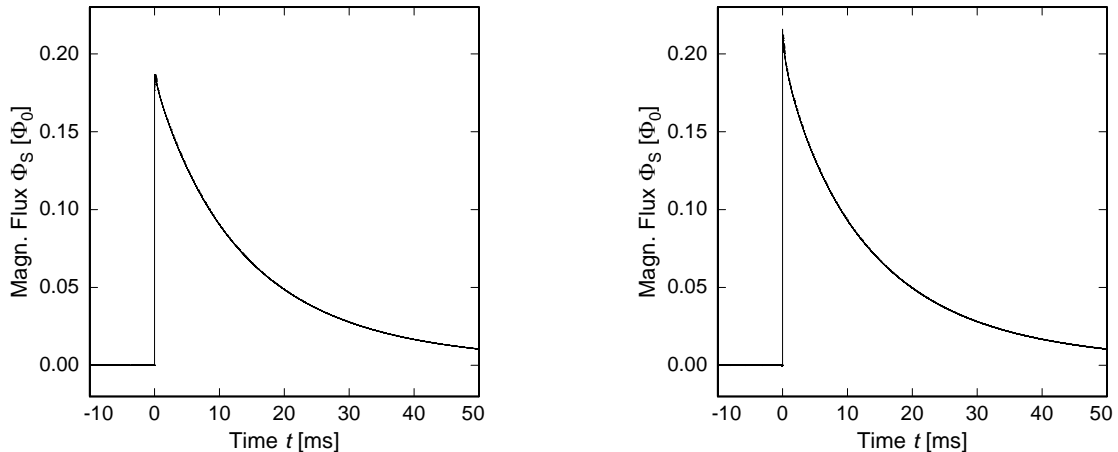


Figure 4.9 Averaged pulses following an interaction of a 5.9 keV x-ray photon absorbed in aluminum (left) and in gold (right). The pulses were recorded at a temperature of $T = 37$ mK with a persistent current of $I = 100$ mA

In figure 4.9 the two different pulse shapes, corresponding to 5.9 keV photons absorbed in the Al absorber and in the Au spacer, are shown. While on a longer time-scale the events look very similar, the beginning looks quite different. Since the events in the gold spacer are absorbed closer to the sensor they show a slightly faster rise time. A second major difference is a fastest decay time of about $\tau = 0.5$ ms due to the presence of the system of the quadrupole moments of the gold nuclei. A further description of the effect of the quadrupole moments of gold can for example be found in [Ens00].

Both kinds of pulses can be quantitatively described by a sum of exponential functions:

$$s(t) = \sum_{I=0}^n A_i \exp(-t/\tau_i), \quad (4.1)$$

with amplitudes $A_i < 0$ for the rise of the pulse, amplitudes $A_i > 0$ for the decay of the pulse and the corresponding time constants τ_i . A maximum of $n = 7$ time constants was used to better fit the pulse.

Both kinds of pulses, those absorbed in aluminium and in gold, can be described by the same time constants for the decay, but not for the rise. However, the amplitudes A_i are different, as shown in table 4.1 for the two pulses depicted in figure 4.9. This leads to the conclusion that the same thermodynamic subsystems are observed independently of the position where the photon is absorbed but that the energy fractions flowing into the subsystems are different.

Rise times:

i	$\tau_{\text{Al},i}$ [μs]	$a_{\text{Al},i}$ [$\text{m}\Phi_0$]	$\tau_{\text{Au},i}$ [μs]	$a_{\text{Au},i}$ [$\text{m}\Phi_0$]
0	0.536	-195	0.387	-242
1	27.2	-13.7	56.9	-0.59

Decay times:

i	τ_i [ms]	$a_{\text{Al},i}$ [$\text{m}\Phi_0$]	$a_{\text{Au},i}$ [$\text{m}\Phi_0$]
2	0.458	5.77	16.2
3	4.30	15.0	24.8
4	13.6	135	139
5	29.7	32.1	32.0
6	220	1.37	1.32

Table 4.1 The rise times, decay times and the corresponding amplitudes of the pulses absorbed in aluminium and gold at $T = 37$ mK with a field current of $I = 100$ mA. The data was obtained by a non-linear-least-square fit of eq. 4.1 to the pulses shown in figure 4.9

Besides the time pattern of the two temperature pulses, the major and more interesting difference is the fact that the area under the pulses for events in superconducting Al is, especially at lower temperature, smaller than the one under the pulses for events in Au. In principle this fact can look unphysical since the area of temperature pulses is defined by the thermal conductance G_{sb} between the temperature sensor and the bath, according to:

$$\int \Delta T dt = \frac{E}{G_{\text{sb}}}. \quad (4.2)$$

Therefore, it should be the same for events that deposit the same energy deposition. In reality this observation was expected since the missing area for events in superconducting absorbers was already discussed in [Cos93]. In this work the temperature dependence of the detector response was investigated, leading to an empirical law for which the missing area was present only at temperatures $T < 2 \cdot 10^{-4} \Theta_{\text{D}}$.

As already said, the difference between the pulses absorbed in aluminium and the ones absorbed in gold is more evident on short time scale. To gain a better understanding the range of time where particular processes in the superconductor lead to the missing area, it is useful to analyse the time pattern obtained by subtracting the pulses for events in Al from the pulses for events in Au. This calculated time pattern, obtained by subtracting two averaged pulses, has still the shape of a pulse and it is shown in figure 4.10 for different temperatures up to $T = 110$ mK for a persistent current of $I = 100$ mA.

The first thing to notice is the sharp peak in the first $2 \mu\text{s}$. This is due to the slightly faster rise time for the Au events. Secondly, and a very important observation is that the difference drops to zero much faster than the original pulses, e.g. with a time constant $\tau = 8.8$ ms at 37 mK.

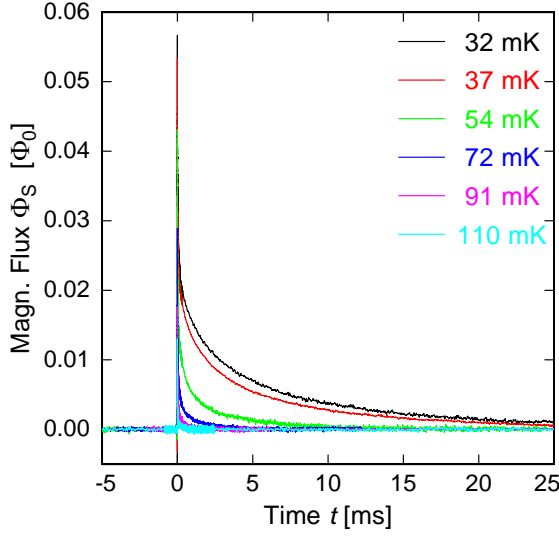


Figure 4.10 The difference $s_{\text{gold}}(t) - s_{\text{alu}}(t)$ at different temperatures for a persistent current of $I = 100$ mA.

On the other hand, the area under this curve represents the discussed missing area. Since, due to the described detector setup, there is only one thermal link to the bath, this missing area should be understood as a missing measured energy. But this relative area difference decreases significantly above about 100 mK. Knowing that the Debye temperature for Al is $\Theta_D = 420$ K [Poo95], this observation is in good agreement with the empirical law presented in [Cos93]. In fact for Al the critical temperature above which there is no evidence of missing area is $T^* = 2 \cdot 10^{-4} \Theta_D \approx 84$ mK.

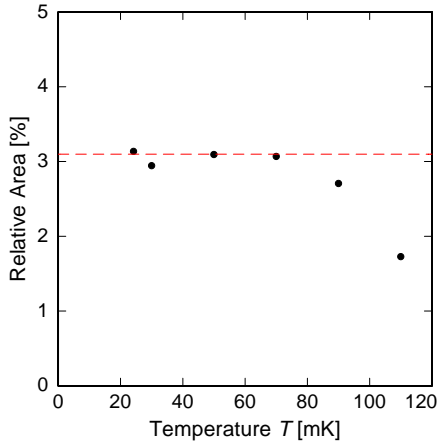


Figure 4.11 The relative area difference between Au and Al pulses $\int (\Delta\Phi_{\text{Au}} - \Delta\Phi_{\text{Al}}) dt / \int \Delta\Phi_{\text{Au}} dt$ plotted against the temperature. The dashed line is just a guide for the eye.

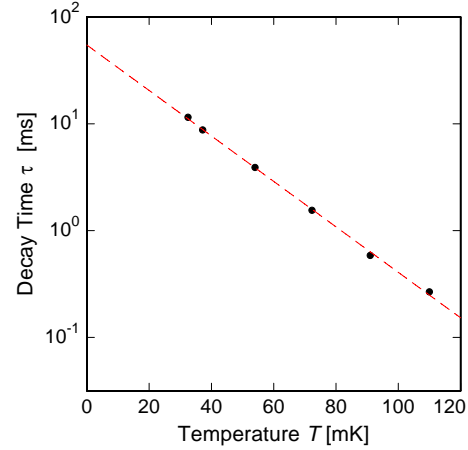


Figure 4.12 The longest and main decay time of the pulses from figure 4.10 plotted against the temperature in semi-logarithmic scale. The dashed line is just a guide for the eye.

In fig. 4.11 the ratio of the area corresponding to the difference to the area of the

events in gold is plotted versus the temperature. In this depiction the good agreement with the evidence presented in [Cos93] is even more convincing. The relative area, which is proportional to the lost energy stays constant up to a temperature of about $T = 80$ mK and is slowly decreasing to higher temperatures. In order to get more reliable data and understanding on this area difference, particularly the temperature dependency, another more careful measurement of the present detector and more experiments with different superconducting absorbers need to be done.

In the same way an other important observation was obtained in this work. In fig. 4.12 the main decay time of the difference-curve is plotted versus increasing temperature in a semi-logarithmic curve. An exponential decay $\sim \exp(-T/T_0)$ describes how this time constant disappears with increasing temperature. The corresponding temperature is $T_0 = 20$ mK. This time constant could be interpreted as the appropriate time in which different processes happening, when a particle interacts in a superconducting absorber, take place. At the moment a clear correlation of this time constant with the ones described in [Koz00a, Koz00b] is not found. Although in this case experiments with different superconducting absorbers will help to better interpret this behaviour.

4.5.2 Signal height and heat capacity

In the following the 5.9 keV x-ray events in aluminium and gold will be discussed further.

For characterising the detector spectra, several hundred pulses were taken with three different persistent currents at different temperatures up to 240 mK. Qualitatively the pulses behave as expected, becoming smaller to higher temperatures because of the increasing heat capacity. A faster decay to higher temperatures is expected additionally, because of the increased thermal conductance to the bath. Both effects can be observed in figure 4.13(left). On the other hand the pulses become larger for higher field currents, i.e. higher mean magnetic fields within the sensor, shown in figure 4.13(right), as the magnetic field $B_{\max}(T)$ causing the maximum signal height, as described in chapter 2.2.3, is not reached for this particular detector setup.

But a more quantitative analysis shows a not perfect agreement with the predicted behavior. From the value of the maximum of the pulse given in magnetic flux $\Delta\Phi$, the temperature rise ΔT and therefore the total heat capacity C_{tot} of the device can be derived by

$$C_{\text{tot}} = \frac{E}{\Delta T} = \frac{E}{\Delta\Phi} \frac{\partial\Phi}{\partial T} \quad (4.3)$$

with the change of flux with temperature $\partial\Phi/\partial T$ as derived from the magnetisation measurements. The pulse heights and the measured heat capacity can now be compared to the theoretical predictions from chapter 2.4 (pulse heights) and chapter 2.2.2 and 2.3.2 (heat capacity), respectively.

Figure 4.14 shows the theoretically predicted pulse heights as solid lines and the measured ones as symbols. As one can see, the measured pulse heights are always

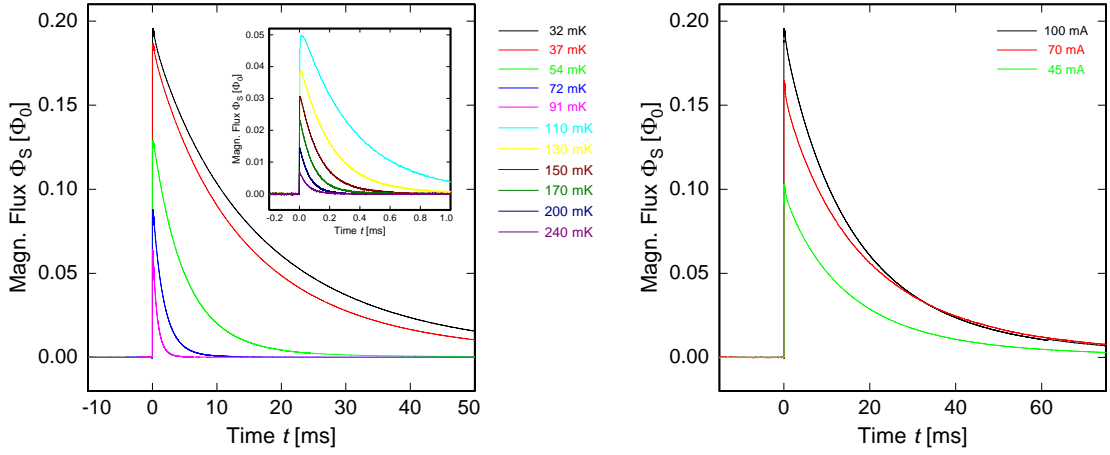


Figure 4.13 Averaged pulses, averaged over more than 100 pulses, upon the absorption of a 5.9 keV x-ray photon in the aluminum absorber. On the left plotted for a persistent current of $I = 100$ mA at different temperatures. While the main plot shows temperatures up to $T = 91$ mK, the inset shows the temperatures above $T = 110$ mK on a shorter timescale. On the right, pulses at $T = 32$ mK are shown for different frozen currents.

smaller than predicted, both for x-rays absorbed in aluminium and gold. Since the magnetisation measurements fit well to the theory (chapter 4.2) and the energy of the photons of the ^{55}Fe source are well known the only free parameter is the heat capacity C_{tot} .

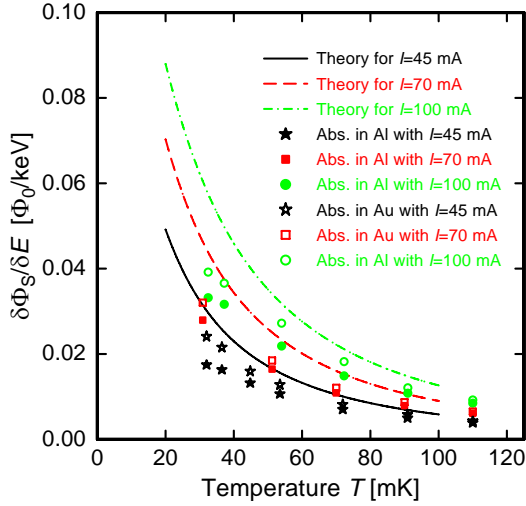


Figure 4.14 Comparison of measured pulse heights (symbols) and theory (lines).

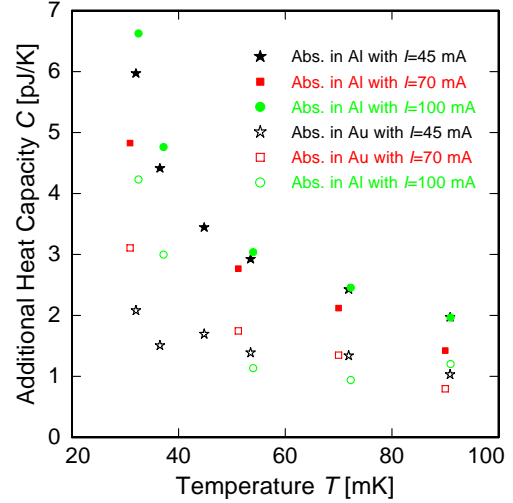


Figure 4.15 Additional heat capacity for the aluminium detector.

Figure 4.15 shows the additional heat capacity that needs to be added to the theoretically expected one in order to achieve the measured value. It seems to be rather independent of magnetic field. While the additional heat capacity corresponding to

the pulses absorbed in gold is not influenced by the temperature very much the one derived from the aluminium pulses shows a quite strong temperature dependence. Other thesis' have shown that the amount of additional heat capacity is proportional to the absolute amount of sputter deposited gold, within sputtered Au:Er sensors and absorbers [Ble09]. The mean value of the additional heat capacity of about $C_{\text{add}} \approx 1.6 \text{ pJ/K}$ is a little smaller than expected from [Ble09] but agrees reasonably well.

On the contrary the values determined from the events absorbed in the aluminium absorber show a strong temperature dependence. Therefore, this heat capacity change with temperature seems to be connected to the presence of the superconducting absorber and is not due to the sputtered gold films.

4.5.3 Thermal conductance to the bath

One of the central points of a calorimeter is the weak thermal link between sensor and heat bath. It is important that no other part of the detector, except for the sensor, is connected to the thermal bath, otherwise this could lead to the fact that not all of the deposited energy will be detected by the sensor. The thermal conductance G can be calculated with the integral over the thermal pulse detected:

$$G = \frac{E}{\int \Delta T dt} = \frac{E}{\int \Delta \Phi dt} \frac{\partial \Phi}{\partial T} \quad (4.4)$$

with the deposited energy E . A T^3 dependency is expected from the Kapitza resistance [Swa89] because the Au:Er sensor is glued to a silicon chip. The observation of this dependency, together with the comparison of the pre-factor with the already measured ones [Wel08], lead to the conclusion that the Kapitza resistance between sensor and bath is the dominant connection in the thermalisation process. Other interfaces, e.g. between spacer and absorber or between chip and brass experimental holder, seem not to contribute significantly.

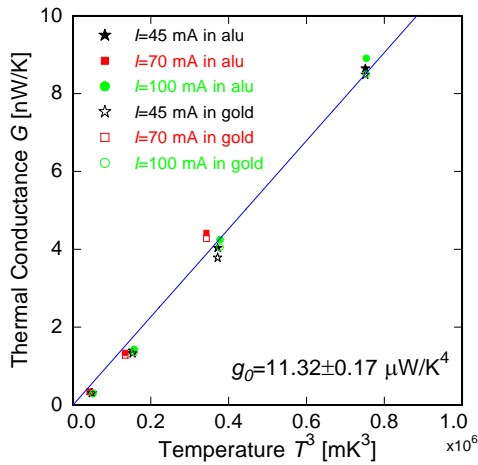


Figure 4.16 The thermal conductivities calculated from the pulse areas of the events absorbed in aluminium and gold.

To calculate the G it was integrated both the area under the Au pulses and under

the Al pulses in order to compare the resulting curves. In fig. 4.16 one can see how there is no systematic difference between the thermal conductivity calculated from pulses due to the interaction of x-rays in Al and the one generated from interaction in Au. This is due to the fact that the difference of area between the two families of pulses is a small fraction, less than 5 %, of the total area of the pulses.

Still fig. 4.16 shows the results of the calculation following eq. 4.4 plotted against T^3 . Except for some small deviations, the data follows a T^3 dependency, as expected, with a slope of $g_0 = 11.32 \pm 0.17 \mu\text{W}/\text{K}^4$. Since the Kapitza resistance scales with the contact area, which is about $A = 200 \times 200 \mu\text{m}^2$ for the used detector, it is useful to introduce an area independent parameter $g_0/A = 283 \text{WK}^{-4}\text{m}^{-2}$. Comparing this parameter to earlier observations it is found that the measured value differs by about 15 % compared to the values $g_0/A = 325 \text{WK}^{-4}\text{m}^{-2}$ and $g_0/A = 328 \text{WK}^{-4}\text{m}^{-2}$ found for the two experiments described in [Wel08]. The discrepancy can be explained by a slight uncertainty of about 10 μm for the side length of the sensor and by possible difference in the amount of used glue.

Since the thermal conductance G follows a T^3 dependency, the conclusion that the whole deposited energy is measured within the signal, at least for the events absorbed in the Au spacer, and no energy is lost in this case can be drawn. These observations are consistent with earlier observations of MMCs with superconducting absorbers [Por07, Höh08, Wel08].

4.6 50 μm Al:Mn detector

4.6.1 Signal Shape

In the case of the detector with Al:Mn absorber it is possible to distinguish K_α and K_β events in the superconducting absorber from K_α and K_β events in the Au spacer. As already done for the aluminium detector only the K_α events at 5.9 keV will be further described since more statistics can be collected due to the fact that the K_β events are only 1/9 as probable as the K_α events.

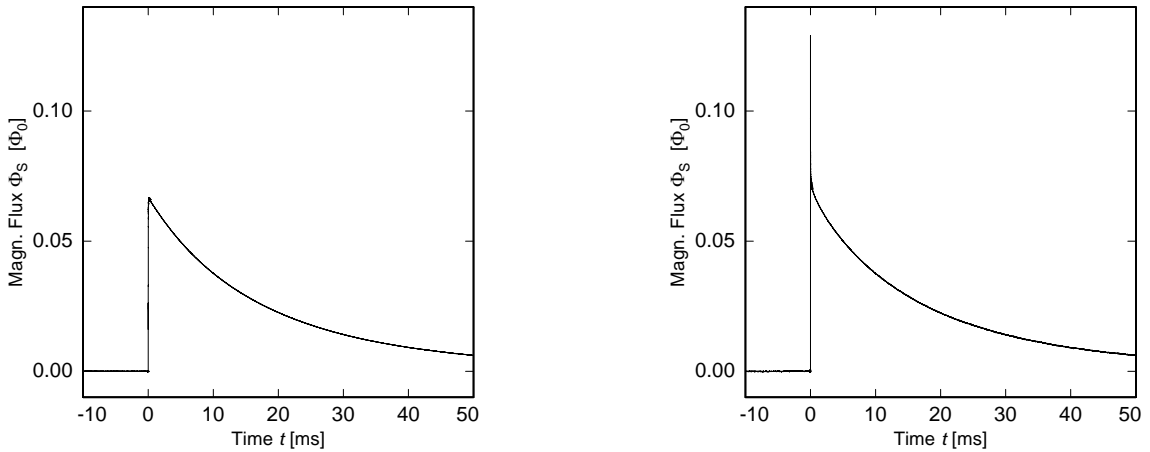


Figure 4.17 Averaged pulses following an interaction of a 5.9 keV x-ray photon absorbed in the Al:Mn absorber (left) and in the Au spacer (right). The pulses were recorded at a temperature of $T = 32$ mK with a persistent current of $I = 35$ mA.

Figure 4.17 shows two characteristic averaged pulses of the detector. On the left a pulse caused by the interaction of a K_α x-ray in Al:Mn and on the right a pulse following the interaction in gold are displayed. They were acquired at a sensor temperature of about 32 mK and a persistent current of $I = 35$ mA. The most prominent feature and the most evident difference occur again in the beginning time interval of the pulse. In fact it is evident the sharp overshoot present in the pulse caused by the photon absorption in Au. A possible interpretation of this initial pulse shape can be found in a fast diffusion of the heat from the Au to the $\underline{\text{Au}}:\text{Er}$ sensor and therefore the height of this peak should correspond to $E/(C_{\text{Au}} + C_{\underline{\text{Au}}:\text{Er}})$. At a later but still very short time the heat is diffused into the Al:Mn absorber and the total system (Al:Mn+Au+ $\underline{\text{Au}}:\text{Er}$) reaches equilibrium, showing the same behaviour as for events in Al:Mn.

In fact, as already seen for the Al detector, the decay of the pulse can be described by a sum of exponentials with the same time constants for both pulses, absorbed in the superconducting Al:Mn and in the gold spacer underneath. The time constants for the pulses in figure 4.17 are shown in table 4.2. Again the fastest decay shows the largest difference in amplitude while for the longer time constants of $i = 1 \dots 3$ the amplitudes are more similar.

i	τ_i [ms]	$a_{\text{Al:Mn},i}$ [$\text{m}\Phi_0$]	$a_{\text{Au},i}$ [$\text{m}\Phi_0$]
0	1.13	0.542	7.48
1	10.8	24.9	23.1
2	23.7	40.3	41.1
3	132	1.54	1.40

Table 4.2 Decay times and the corresponding amplitudes of the pulses absorbed in Al:Mn and Au at a temperature of $T = 32$ mK with a field current of $I = 35$ mA. The data was obtained by a non-linear-least-square fit of eq. 4.1 to the pulses displayed in figure 4.17.

Difference between Au and Al:Mn Pulses

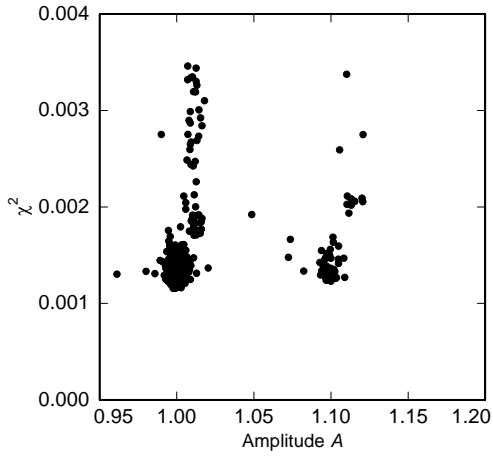


Figure 4.18 χ^2 versus amplitude plot of events measured at a temperature of $T = 32$ mK with a persistent current of $I = 35$ mA. The record length was $\Delta t = 320$ ms.

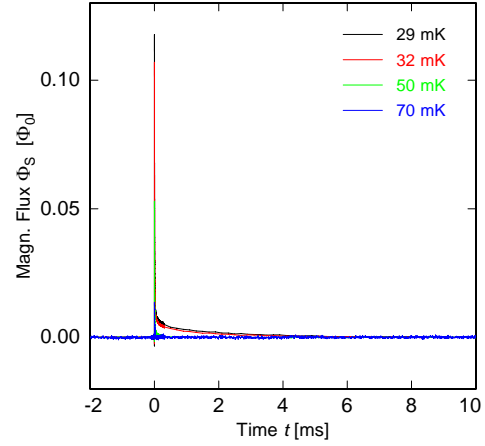


Figure 4.19 The difference of pulses following the absorption of 5.9 keV in Au and Al:Mn up to temperatures of $T = 70$ mK with a persistent current of $I = 35$ mA.

The difference between Au and Al:Mn pulses can be worth some investigation in case of the Al:Mn detector, too. The development of the χ^2 is the first evidence. While figure 4.5 was obtained by a short time window with a record length of $\Delta t = 0.4$ ms, figure 4.18 shows a χ^2 versus amplitude plot, recorded at the same temperature $T = 32$ mK and with the same frozen current of $I = 35$ mA, but with a record length of $\Delta t = 320$ ms. The average χ^2 for the pulses originating from absorption in gold is $\chi^2 = 0.003$ and therefore about an order of magnitude smaller than the one from the smallest time window and the different pulse types can not be discriminated as easily.

Figure 4.19 shows the subject under a quantitative point of view. The pulse differences at temperatures up to $T = 70$ mK are depicted. The first thing to notice is that the pulses show a very short main decay time of $\tau(30 \text{ mK}) = 1.6$ ms. Secondly, and as important, is the observation that the difference gets below $\Phi_S = 0$ and reaches zero again with a rather long time constant, e.g. $\tau = 160$ ms at a temperature of 30 mK, and therefore can compensate the area difference caused in the first few

milliseconds. The relative area difference is depicted in figure 4.20 and as can be seen clearly, the differences scatter around zero leading to the conclusion that the area of Au and Al:Mn pulses is equal within the noise and therefore no energy is “lost” unlike within the detector with Al absorber.

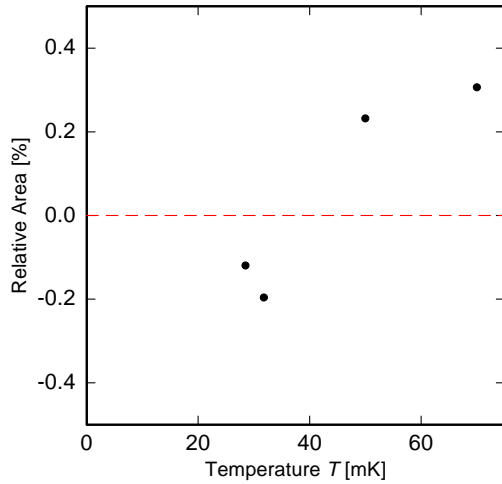


Figure 4.20 The relative area difference between Au and Al:Mn pulses $\int(\Delta\Phi_{\text{Au}} - \Delta\Phi_{\text{Al}}) dt / \int \Delta\Phi_{\text{Au}} dt$. The dashed line is a guide for the eye.

As the Debye temperature of pure Al and Al doped with 2000 ppm of Mn should be very similar, the absence of a clear observation of missing energy must be interpreted as a violation of the empirical law $T^* = 2 \cdot 10^{-4}\Theta_D$ given in [Cos93], presumably caused by the presence of Mn ions.

Pulse Development on Short Time Scales

Looking at the signal rise closer, as it is done in figure 4.21, it turns out that there is a sharp rise followed by a fast decay before the main rise can be seen in the Al:Mn pulse (left). Photons absorbed in the Au spacer (fig. 4.21 right) produce a much faster signal rise, followed by a still very fast first decay.

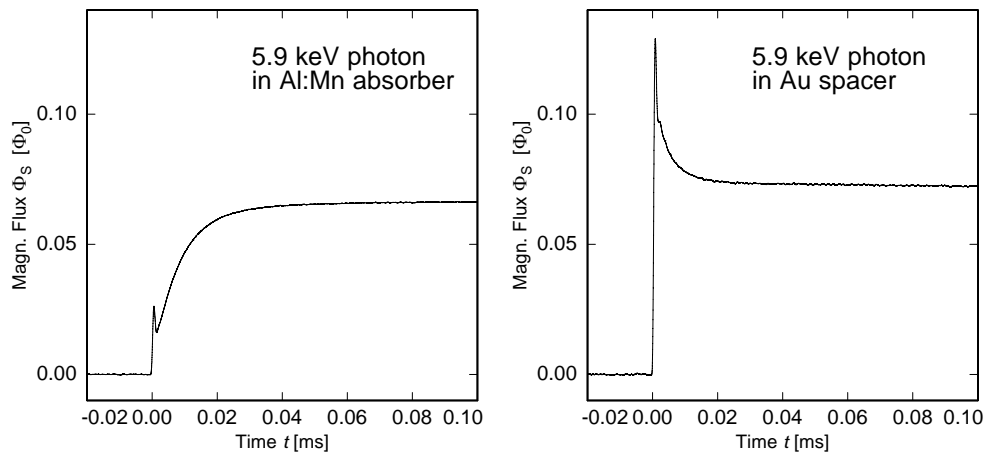


Figure 4.21 The first 0.1 ms of the pulses shown in figure 4.17.

A qualitative explanation of such pulse shapes is quite hard in a thermodynamic model. The fast rise of the pulses absorbed in gold (right) could be explained by the good thermal coupling between the Au spacer and the Au:Er sensor. The first decay of those signals might, however, be caused by the Al:Mn absorber which thermalises with the sensor and spacer a little delayed. Therefore, the signal would drop again corresponding to the total heat capacity.

The behavior of the pulses absorbed in the Al:Mn absorber could be explained similarly. A few fast, athermal excitations, e.g. ballistic phonons, could get through to the absorber warming up sensor and spacer. Again this little amount of heat thermalises with the Al:Mn absorber causing the signal to drop again. Most of the deposited energy would, however, be transported in comparably slow thermal diffusion processes being responsible for the slow rise ($\tau = 8 \mu\text{s}$) in figure 4.21(left). In the Al:Mn absorber most transport processes are almost completely thermal because the athermal processes are stopped at the additional scatter centres offered by the magnetic impurities [Wel08].

A problem, nevertheless, are the relative values of the heat capacity which will be quantitatively analysed in the following chapter 4.6.2. On the contrary, there is a far easier, and more plausible explanation by introducing a second, opposite signal contribution as discussed in section 4.6.3.

4.6.2 Pulse Heights

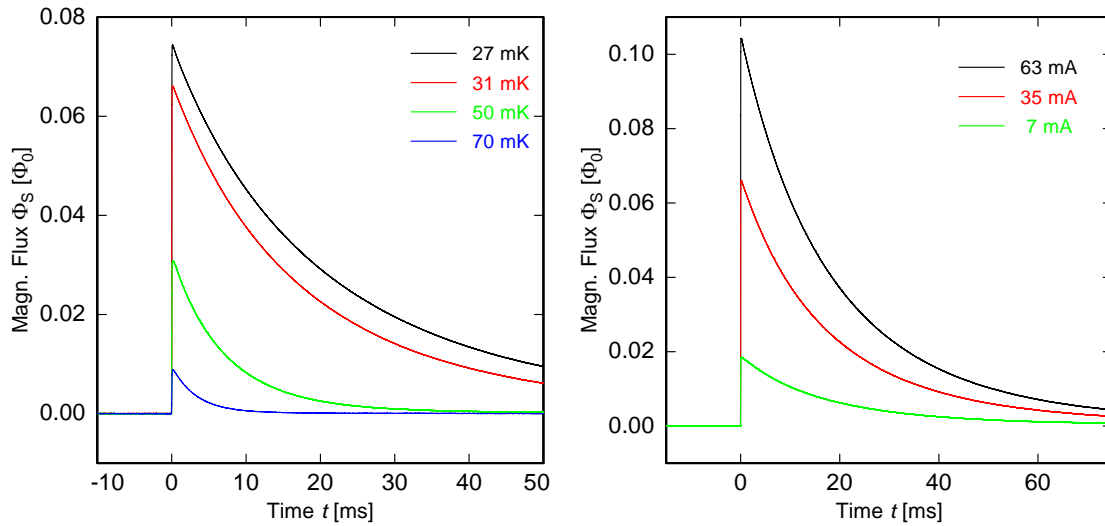


Figure 4.22 Pulses upon the absorption of a $\text{K}\alpha$ x-ray in the Al:Mn absorber. On the left shown with a persistent current of $I = 35 \text{ mA}$ at different temperatures; on the right for a fixed temperature of $T = 32 \text{ mK}$ for different persistent currents.

Even though the signal shape of the Al:Mn detector behaves quite unexpected one might still get some useful information out of the observed pulse heights.

The development of pulses upon the absorption of 5.9 keV photons in the Al:Mn absorber with temperature T is displayed in figure 4.22 (left) for a persistent current

of $I = 35$ mA. On the right the dependency on magnetic field is shown at a fixed temperature $T = 32$ mK for different persistent currents. The pulses behave qualitatively as expected since they become smaller for higher temperatures and larger for higher currents.

A more quantitative analysis is shown in figure 4.23. As already seen for the Al detector in figure 4.14, the x-rays absorbed in gold show just a slight deviation from the estimated theoretical signal height, but the pulses originating from the absorption in Al:Mn are much smaller than expected. This observation supports the assumption that the detector without superconducting absorber behaves as expected and the presence of the superconductor is responsible for all unexpected effects. This assumes again, that the energy absorbed in gold first thermalises within the gold spacer and the Au:Er sensor before thermalising with the superconducting absorber a little delayed.

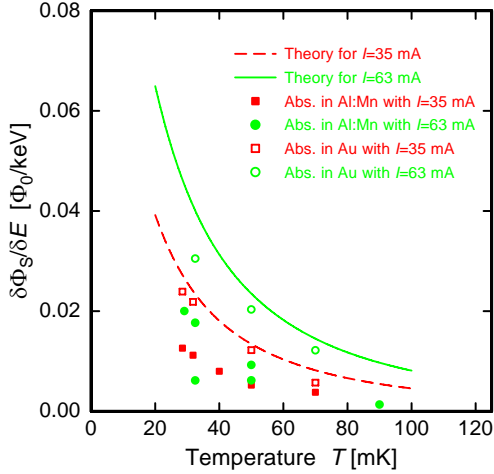


Figure 4.23 The measured pulse heights (symbols) of the Al:Mn detector in comparison with the theoretically estimated ones (lines).

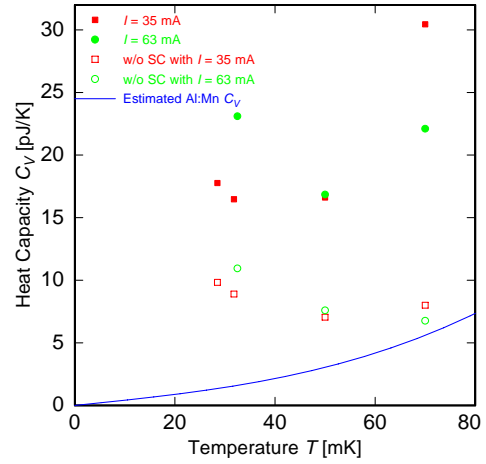


Figure 4.24 Calculated heat capacities estimated from the gold pulses of the Al:Mn detector. The open symbols show the result from the sharp peak in the beginning, while the solid symbols show the up to 4 times larger total heat capacity. The solid line shows a theoretical estimate of the Al:Mn absorber's heat capacity.

This way the heat capacity, that is needed to explain the first very fast decay shown in figure 4.21 can be quantitatively determined. Because of the cleaner, thermodynamically easier explainable, pulse shape this calculation uses only the data of pulses originating from the absorption in gold (see fig. 4.21 right). The result is shown in figure 4.24. As can be seen, the total heat capacity is up to four times larger than the one expected from the peak of the gold pulses. Even taking into account the heat capacity of a completely superconducting Al:Mn absorber calculated with

eq. 2.18¹ shows that the total heat capacity would still be up to twice as high as expected.

This means that there is still an unexpected contribution to the heat capacity. A possible contribution can be normal conducting regions within the superconducting absorber which have a much higher heat capacity. An easier solution can be provided by introducing an additional opposite signal contribution as described in the following chapter 4.6.3.

4.6.3 Pulses at High Temperatures

In chapter 4.6.2 only the temperature evolution up to $T = 70$ mK was discussed unlike the Al detector (chapter 4.5.2) where pulses up to $T = 240$ mK were shown. This is due to the different behavior of the pulses at higher temperatures which will be discussed in the following.

If one looks at the high temperature pulses shown in figure 4.25 the behavior is the exact opposite as pulse height gets larger towards higher temperatures and changes direction relative to the pulses acquired at low temperatures.

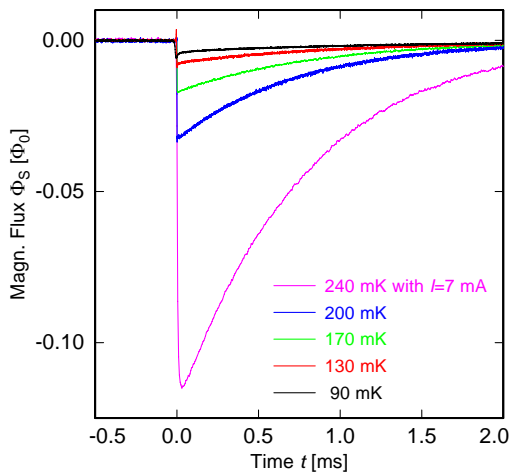


Figure 4.25 Averaged pulses in residual field at high temperatures and within the transition. The pulses were measured with a persistent current of $I = 35$ mA except for the one at $T = 240$ mK which was measured with the residual field, corresponding to $I = 7$ mA.

At the first glance this behavior seems unusual and somehow wrong but by looking at the high temperature part of the magnetisation shown in figure 4.26 which was not shown in figure 4.2 it can be understood in a different way. The temperature dependency of the magnetic flux changes direction at a temperature of about $T^{-1} \approx 12.5 \text{ K}^{-1} \Leftrightarrow T = 80$ mK and becomes very steep and stays this way up to about $T = 300$ mK which is the estimated transition temperature T_c for Al:Mn with the used concentration of about 2000 ppm Mn [Boa66].

An interesting effect can be seen in figure 4.27, which shows the beginning of a pulse acquired in the mentioned intermediate range at $T = 90$ mK. Judging from the magnetisation measurement approximately no signal would be expected, but actually the signal bipolar and the two different contributions nearly cancel each

¹For the calculation a Sommerfeld coefficient of $\gamma = \gamma_{\text{Al}} = 1.4 \text{ mJ}/(\text{mole K}^2)$, a transition temperature of $T_c = 300$ mK and a critical field of $B_0 = 2.6$ mT were assumed.

other out. The sharp peak in positive flux goes in the direction of the low temperature pulses while the main pulse goes into the direction of the high temperature pulses. This means the signal contribution responsible for the low temperature pulses – the Au:Er – is generated faster by the deposited energy but is slightly smaller than the contribution of the new flux change.

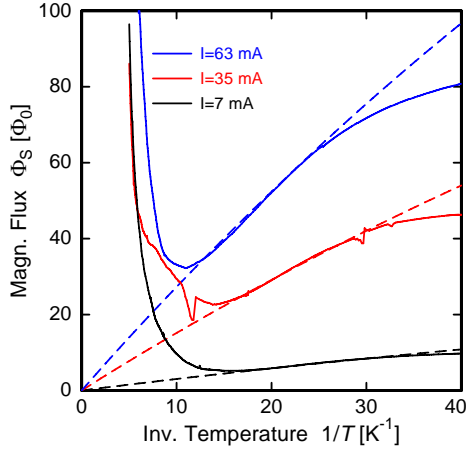


Figure 4.26 The complete magnetisation measurement for three different persistent currents I of the Al:Mn detector. The jumps in the $I = 35$ mA are artefacts..

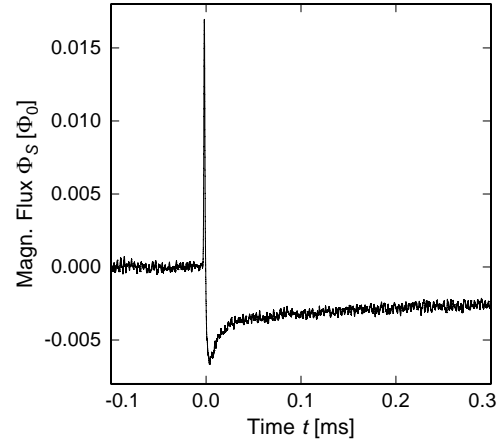


Figure 4.27 Averaged pulse at $T = 90$ mK with $I = 35$ mA showing bipolar signal shape.

Therefore this additional flux change seems not to originate from the Au:Er sensor but from some other source and it is suspected to be the superconductor itself. The magnetic field originating from the meander gets pushed out of the superconductor due to the Meissner-Ochsenfeld effect during the transition. But this effect occurs just until a critical magnetic field B_c is reached and if B_c is exceeded the superconductivity breaks down again (see chapter 2.3.3). And since B_c shows a temperature dependency (eq. 2.20) the expulsion of the magnetic field is temperature dependent as well and this effect can be measured as flux change in the pickup coil below the superconductor.

5. New Sensor Design

5.1 Principle of Magnetic Transition Edge Sensors

As already said in chapter 2.1 the heart of a calorimeter is the temperature sensor. In Metallic Magnetic Calorimeters the temperature dependence of the magnetisation of a paramagnetic sensor, read out by a SQUID, is used to monitor the temperature of the calorimeter. Due to the Curie-law, $M \sim 1/T$, the sensitivity to temperature change increases drastically towards low temperature.

However, in the experiments with superconducting absorbers that were discussed in the last chapter, it was observed, that the Meissner-Ochsenfeld effect, i.e. the expelling of magnetic flux of a superconductor, when it is cooled below T_c , leads to a temperature dependent flux in a nearby pick-up coil, which can be as steep and even steeper than the one caused by the paramagnetic sensor. The idea how the additional steep flux change occurs should be explained in the following simplified example.

Lets imagine a superconducting dice in an external magnetic field and assume the absolute value of the field decreases rapidly along the z -direction $dB/dz < 0$. At some height the magnetic field will be lower than B_c and a flat normal-conducting-to-superconducting boundary will form at this point (not taking into account the field deformation caused by the Meissner effect). If the critical field is changing, the boundary will move slightly up or down, too.

If a pick-up coil is positioned close to the superconductor, a change of flux would be detected. Therefore this magnetic flux is a function of critical field, $\Phi = \Phi(B_c)$. Since the critical field depends on temperature (eq. 2.20) the flux change depends on temperature, too $\Phi(B_c(T))$. Therefore it is possible to calculate what is the change of flux, corresponding to a known change of temperature

$$\Delta\Phi \simeq \frac{\partial\Phi}{\partial B_c} \frac{\partial B_c}{\partial T} \Delta T \quad (5.1)$$

However, if this change of temperature is caused by the release of energy ΔE in a heat capacity C_{tot} (which is meant to be the detector's heat capacity), the change of flux is directly proportional to the energy ΔE

$$\Delta\Phi \simeq \frac{\partial\Phi}{\partial B_c} \frac{\partial B_c}{\partial T} \frac{\Delta E}{C_{\text{tot}}}. \quad (5.2)$$

5.2 Superconductors suitable for the New Sensor Concept: The Case of Hafnium

There were some considerations to make while choosing the superconducting sensor material for this new type of detector. A superconductor with a low transition temperature was chosen, since far below T_c the slope of $\partial B_c/\partial T$ would be too small. On the other hand the critical field B_c should be small as well (which usually goes along with a low transition temperature), so that the magnetic field originating from the available meander structure can exceed the critical field close to the meander.

Hafnium ($T_c = 0.13$ K) and iridium ($T_c = 0.11$ K) fulfill the named prerequisites. Among these two candidates hafnium has the advantage of having stable isotopes without nuclear spin (0.16 % ^{174}Hf , 5.3 % ^{176}Hf , 27 % ^{178}Hf and 35 % ^{180}Hf in the natural isotope abundance) and using enriched hafnium of one of these isotopes in some future detector setup would prevent a possible additional heat capacity due to hyperfine splitting as described in chapter 2.2.4 in the case of ^{167}Er . Because of this possible advantage for future detector setups hafnium was chosen.

Some general properties of hafnium are shown in table 5.1.

Atomic number	72
Density	13310 kg m ⁻³
Molar volume	13.44 cm ³ /mole
Electronic configuration	[Xe]4f ¹⁴ 5d ² 6s ²
Crystal structure	hcp
Debye temperature Θ_D	252 K
Transition temperature T_c	0.13 K
Critical field $B_c(0)$	1.27 mT
Energy gap 2Δ	0.044 meV
El. resistance (300 K)	340 nΩm
Average RRR^1	30 [Des84]
Melting point	2506 K
Sommerfeld coefficient γ	2.2 mJ/(mole K ²)
Absorption length $\lambda(6 \text{ keV})$	2.32 μm

Table 5.1 Some general data about hafnium. Data from [Poo95] or [Win] if not stated otherwise.

5.3 Prototype Setup

To test the new type of temperature sensor a prototype detector was built. For this purpose a MagCal Nr. 14 was used, which is structured in the same way as a MagCal Nr. 15 described in chapter 3.4.1 but has an additional layer of 350 nm SiO₂ as insulation layer on top of the anodised niobium structures.

¹Residual Resistance Ratio

A foil of $25\ \mu\text{m}$ thick hafnium was sawn into $200 \times 200\ \mu\text{m}^2$ squares with a wafer saw. One of these squares was glued on the meander opposing the heater with epoxy glue² and mechanically pressed onto the chip with a ceramic tip, for about 16 hours until the glue was dried, to ensure the lowest possible distance between foil and meander.

The next steps for preparing the complete detector are the same as for the MMCs with Al and Al:Mn absorber (see chapter 3.4.2) and therefore not described further in this place.

5.4 Simulations for Magnetic Transition Edge Sensors

With the theoretical knowledge of chapter 2.3 and the detector principle (chapter 5.1) one can estimate the behaviour of a detector using a superconducting material as temperature sensor. As described above, the detector prototype discussed here makes use of a meander shaped pick-up coil, which provides a magnetic field that decreases exponentially with increasing distance from the meander. The calculation of the magnetic field distribution can only be done numerically and was carried out by the finite element methods³.

The simulations are all done for the actual detector setup (see chapter 5.3) and executed for different persistent currents in the meander.

5.4.1 $B(H)$ relation

To simulate the behaviour of a superconductor in a magnetic field a non-linear flux density \vec{B} to \vec{H} relation was used. Because the capabilities of the software were limited, the theoretical behaviour

$$B = 0 \quad H < H_c = \frac{B_c}{\mu_0\mu_r} \quad (5.3)$$

$$B = \mu_0\mu_r \cdot H \quad H > H_c = \frac{B_c}{\mu_0\mu_r} \quad (5.4)$$

was not used but the relations were smeared out in the following way:

- for $H < H_c$ B is linearly increasing according to $B(H_c) = 0.01 \cdot B_c$,
- the jump at H_c is smeared out by a Fermi function by 5 %,
- $\mu_r = 1$, which is a good approximation for most normal metals

²STYCAST 1266 A/B by Emerson & Cuming

³Software: FEMM 4.0: Finite Element Method Magnetics 4.0 by David Meeker (dmeeker@ieee.org)

leading to the following relation (plotted in figure 5.1):

$$B(H) = \left(1 - \frac{0.99}{1 + \exp\left(\frac{\mu_0 H - B_c}{0.05 \cdot B_c}\right)} \right) \mu_0 H \quad (5.5)$$

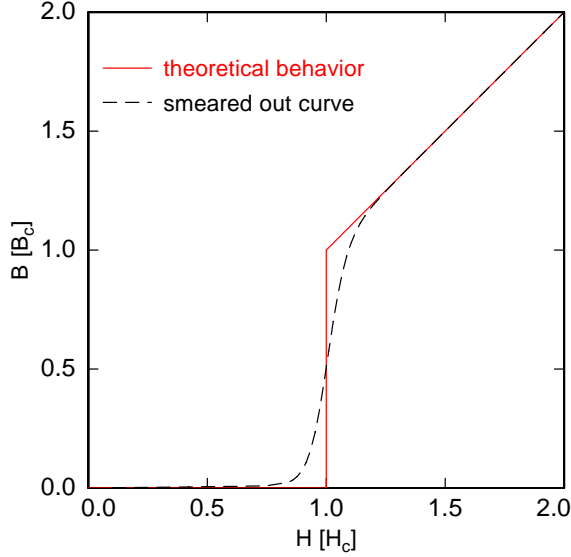


Figure 5.1 The theoretical behaviour of the $B(H)$ relation (—) and the smeared out curve used in the simulations (- - -) after equation 5.5

5.4.2 Flux change

With this simplified and approximated $B(H)$ relation the simulations were carried out for a range of critical fields B_c . Two exemplary results for two different critical fields are shown in figure 5.2.

The simulation results can provide most of the necessary information to get an estimate of the detector behaviour.

By integrating the magnetic field over the area that is enclosed by the meander, i.e. every other gap between the meander stripes in figure 5.2, the magnetic flux in the meander can be evaluated:

$$\Phi(T) = \iint \vec{B}(T) d\vec{S} \quad (5.6)$$

$$\Rightarrow \frac{\partial \Phi}{\partial T} = \frac{\partial}{\partial T} \iint \vec{B}(T) d\vec{S}. \quad (5.7)$$

The results of the integration for $B_c(0) = 1.27$ mT, $T_c = 130$ mK and the arbitrarily chosen persistent currents of $I_1 = 50$ mA, $I_2 = 100$ mA and $I_3 = 150$ mA are shown in figure 5.3.

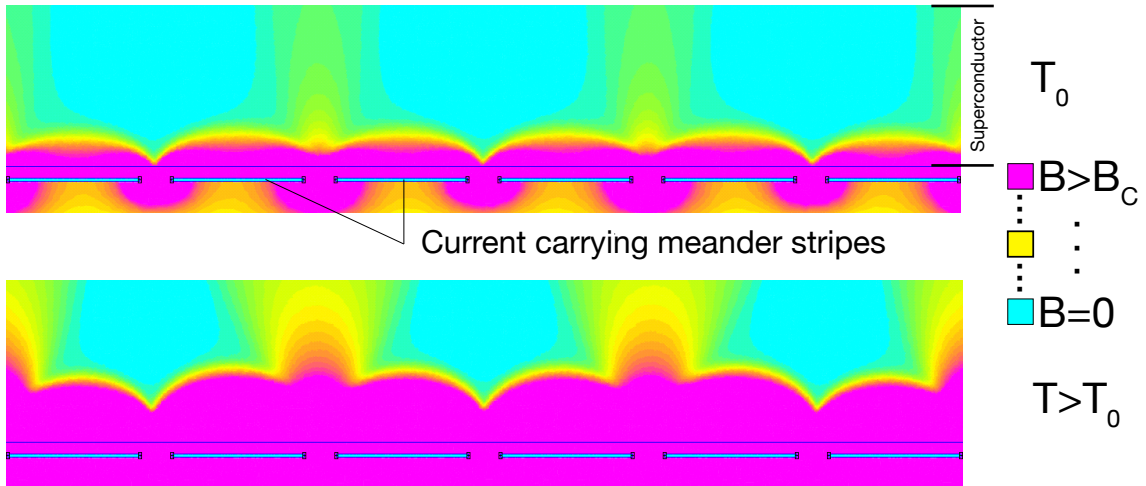


Figure 5.2 Exemplary results of the FEMM simulations showing the meander stripes carrying current with alternating directions and the B -field distribution in the superconducting sensor material.

Top: Result of FEMM simulation for high B_c corresponding to a low temperature.

Bottom: Result for a low B_c or a high temperature.

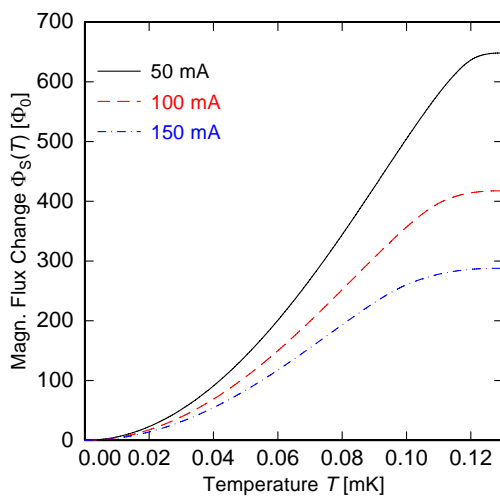


Figure 5.3 The simulated flux in the meander plotted against the temperature for the setup described in chapter 5.3 for $B_c(0) = 1.27$ mT, $T_c = 130$ mK and three persistent currents of 50 mA, 100 mA and 150 mA in the meander.

5.4.3 Heat Capacity

The next step is to estimate the heat capacity of the superconducting sensor. At first it is necessary to determine the volume of the superconducting and normal conducting regions. Since the fraction P_{sc} of the superconducting material depends only on the magnetic field distribution we need to determine this distribution from the result of the FEMM simulation by taking the magnetic field values at many points with a random distribution within the volume of the superconductor. Doing this leads to a histogram (fig. 5.4) and summing over the bins with $H < H_c$ and $H > H_c$ gives the wanted fraction. Using the theoretical equations of chapter 2.3.2 (eq. 2.15 and 2.18) the heat capacities can be calculated as

$$C_{tot}(T) = V \cdot (P_{sc}(T) \cdot C_{sc}(T) + (1 - P_{sc}(T)) \cdot C_{nc}(T)). \quad (5.8)$$

Results are shown in figure 5.5.

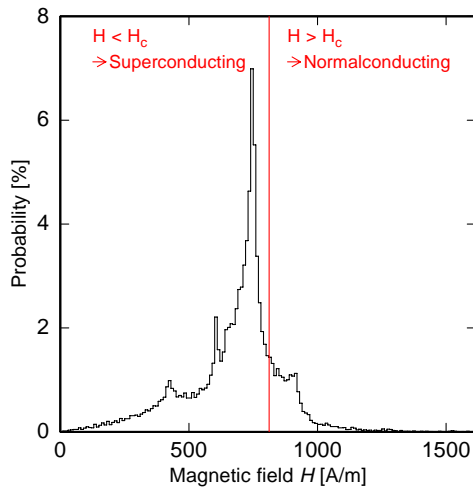


Figure 5.4 Distribution of the magnetic field H in the sensor volume for $I = 50$ mA and $B_c = 1$ mT. The red vertical line determines the border of superconducting to normal conducting volume at the value H_c .

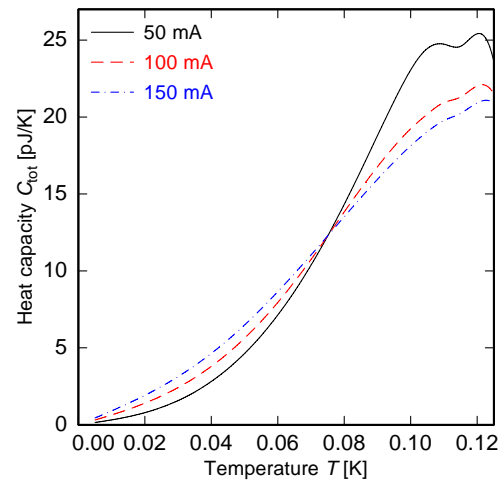


Figure 5.5 The simulated heat capacity of the prototype detector for different currents in the meander

5.4.4 Detector Signal

Now the detector signal generated by an energy deposition E can be calculated:

$$\Delta\Phi = \underbrace{\frac{\partial\Phi}{\partial B_c} \frac{\partial B_c}{\partial T}}_{\partial\Phi/\partial T} \frac{E}{C_{\text{tot}}} \quad (5.9)$$

Here, the latent heat required to actually change the fraction of normal conducting volume and therefore move the phase boundary were neglected, assuming that it is significantly smaller than the heat required to warm up the already existing normal and superconducting volumes.

For the calculation of the signal size $\Delta\Phi$ a deposited energy of 5.9 keV is assumed, since the characterisation measurements were done with x-rays from an external ^{55}Fe source, which emits x-ray fluorescence photons of ^{55}Mn including the dominating K_α -line at 5.9 keV. The results for different currents in the meander are shown in figure 5.6.

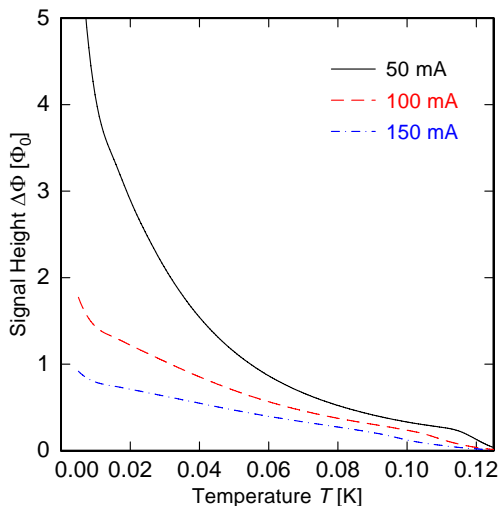


Figure 5.6 The simulated flux change in the SQUID upon the absorption of 5.9 keV photons for different currents in the meander.

5.5 Experimental Results

The built prototype of a magnetic transition edge sensor, described in section 5.3, was characterised with respect to several different aspects. Four different currents were injected into the meander and different properties were measured. The flux change in the SQUID was measured as a function of temperature, similar to the magnetisation measurements of MMCs, and the pulse height and noise at different temperatures for each current were investigated. The achieved data will be shown and discussed in the following sections.

5.5.1 Magnetic Flux Noise at Low Temperatures

As already discussed in the context of MMCs, the noise of a detector is similarly important as the signal size itself, since the signal-to-noise ratio determines its energy resolution. The theoretical understanding of the new sensor type is not far enough developed that the noise is fully understood, but a few experimental observations can be shown.

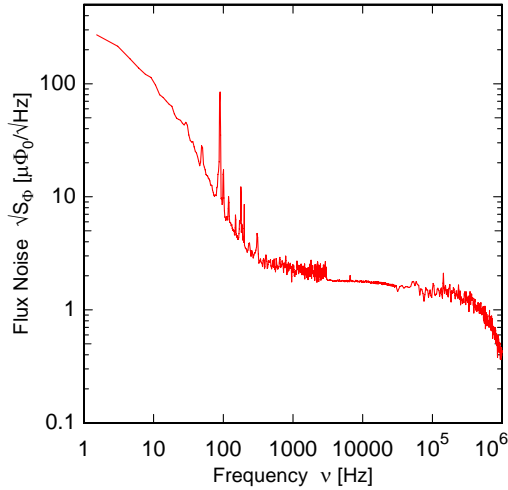


Figure 5.7 Spectrum of the magnetic flux noise in the detector SQUID for injected current of $I_0 = 160$ mA and a temperature of $T = 17$ mK.

Figure 5.7 shows the noise spectrum with an injected current of $I_0 = 160$ mA at a bath temperature of $T = 17$ mK. Above about 1 kHz the noise shows a white noise level of about $\sqrt{S_\Phi} = 1.5 \mu\Phi_0/\sqrt{\text{Hz}}$ with a cut off around 1 MHz which can be interpreted as a combination of white noise sources already described for the MMCs in section 4.1, mainly consisting of flux noise of the SQUID. The observation that this white noise level hardly changes with detector temperature suggests that the Johnson noise contribution of the normal conducting part of the sensor is of minor importance. Below 1 kHz the flux noise rises steeply, following an approximate proportionality $S_\Phi \propto f^{-2}$. At frequencies below about 30 Hz the slope of the noise gets more flat, approaching $S_\Phi \sim 1/f$, and the flux noise reaches a value of $\sqrt{S_\Phi} = 500 \mu\Phi_0/\sqrt{\text{Hz}}$ at a frequency of 1 Hz. This behaviour is qualitatively like the sum of the spectra of thermodynamic fluctuations of energy (section 2.5.2) and of a $S_\Phi \sim 1/f$ noise, similar to the situation in MMCs discussed in section 2.5.2. It is worth to mention,

that the cut-off frequencies of about 30 Hz for the thermodynamic fluctuations of energy that is obtained in this interpretation, is in good agreement with the one expected from the decay time of the pulses, that will be discussed in section 5.5.4.

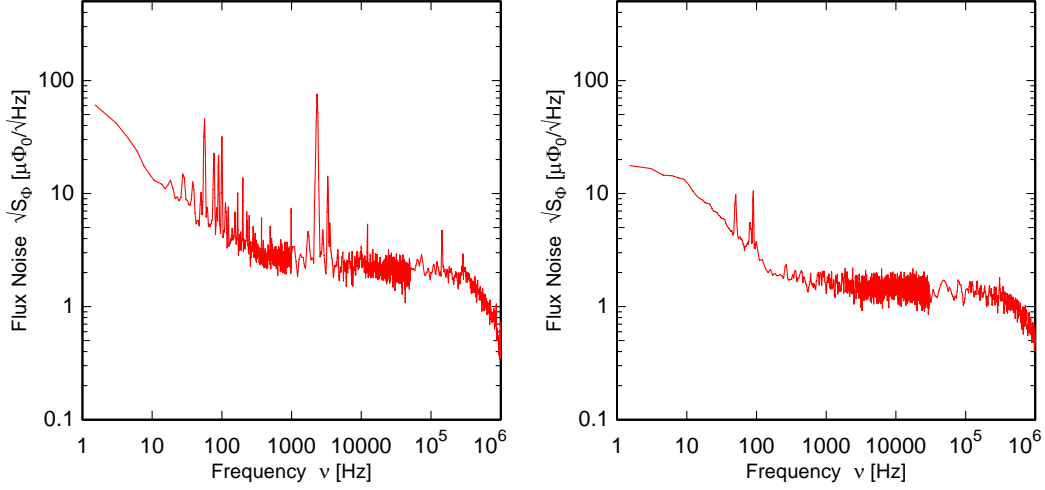


Figure 5.8 Left: Noise spectrum for an injected current of $I_0 = 160$ mA at a temperature of $T = 120$ mK.

Right: Noise spectrum for an injected current of $I_0 = 20$ mA at a temperature of $T = 17$ mK

For different combinations of current and temperature this low frequency noise changes, as displayed in figure 5.8, while the white noise level changes only marginal due to the temperature dependant magnetic Johnson noise. At higher temperatures with the same current (figure 5.8 left) the low frequency noise becomes about one order of magnitude smaller ($\sqrt{S_\Phi} \approx 80 \mu\Phi_0/\sqrt{\text{Hz}}$) showing almost a pure $S_\Phi \sim 1/f$ behaviour. For a smaller current in the meander (fig. 5.8 right) the low frequency plateau becomes lower and reaches about $\sqrt{S_\Phi} = 18 \mu\Phi_0/\sqrt{\text{Hz}}$ at 1 Hz and the $1/f$ noise contribution seems to be smaller.

5.5.2 Magnetic Flux Change

For the detector characterisation four different currents were injected into the meander (20 mA, 50 mA, 100 mA and 160 mA). Figure 5.9 shows the four flux change measurements measured from a temperature of about 150 mK, which is above the transition of Hf, down to the base temperature of the cryostat at about 17 mK.

While the measurements for 20 mA, 50 mA and 100 mA scale approximately linearly with the injected current, the measurement for 160 mA seems to be too small. On the one hand this can be explained by the uncertainty of the actually frozen current in a MagCal No. 14 (see chapter 3.4.1). On the other hand observations during the measurements following the 160 mA measurements suggest some parasitic external magnetic field contribution that could cause such a lowering of the signal. It is more likely that the second effect is mainly responsible for the decreased signal

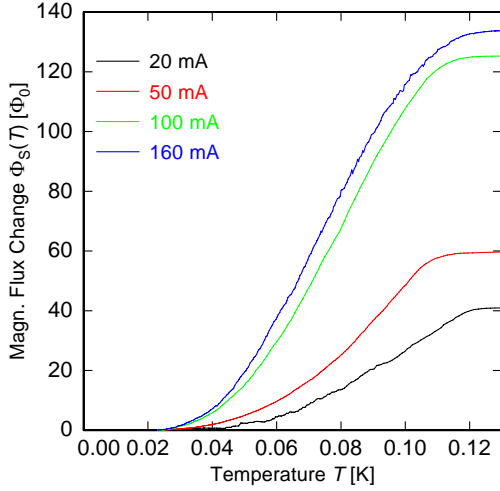


Figure 5.9 The measured flux change in the detector SQUID of the Hf detector for four different currents in the meander.

since all injected currents are affected by the reduction of actual frozen current.

If compared to the simulations in figure 5.3, evidently the weak point of the simulations is found in the simulation of the flux change. First of all the simulated flux change is about a factor of 5 larger than the measured one. Secondly, even the qualitative behaviour is different, since the largest flux change is simulated for $I = 50$ mA and it becomes less for higher currents. Instead, in the experiment the magnetic flux increases monotonically with magnetic field.

A fact that can not be taken into account in the comparison of simulations and experimental data is the parasitic heating of the chip because there is no reliable theoretical curve to compare the data to. As already described in chapter 4.2 the parasitic heating of the chip can and will lead to a higher base temperature on the chip compared to the bath temperature. Since the setup was not additionally connected to the thermal bath with gold bonding wires as done for the MMCs (see chapter 3.4.2) the lowest temperature might be much higher than achieved with the MMCs. By comparing the setup to earlier experiments on a MagCal Nr. 14/15 without additional thermalisation the end temperature can be estimated to about 50 mK [Sch07, Por07].

But even this thermal de-coupling would not explain the observed discrepancies, leading to the conclusion that the simulation of the $\Phi(T)$ based on the $B(H)$ relation of equation 5.5 was oversimplifying the problem. Of course the existence of the London penetration depth was ignored in this approach, but also this should not be responsible for the observed discrepancies. The discrepancies between theory and experiment might, instead, result from the rather complex pattern of magnetic flux lines in a superconductor that is cooled down through T_c in an external magnetic field. Both, a trapping of flux lines causing an imperfect Meissner-Ochsenfeld effect, as well as a complex flux texture in the mixed state might be responsible for the observed discrepancy. Both effects have clearly not been captured by the simulations.

5.5.3 Signal Height and Heat Capacity

The pulse height upon the absorption of 5.9 keV photons was also determined at different temperatures and for different persistent currents in the meander. The result is shown in figure 5.10. As expected from the flux change measurement (figure 5.9) the highest pulses are observed for the highest current in combination with lowest temperature and become smaller for higher temperatures according to the expected behaviour of the heat capacity (fig. 5.5).

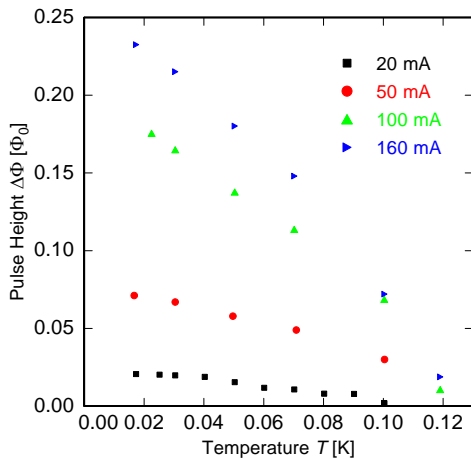


Figure 5.10 The measured pulse heights for four different currents injected into the meander.

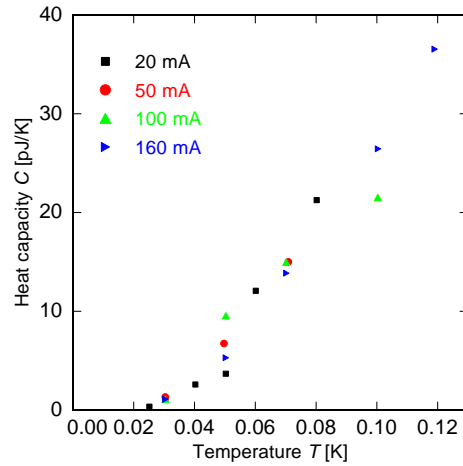


Figure 5.11 The heat capacity of the Hf sensor for different persistent currents in the meander calculated using eq. 4.3.

The measured pulse heights are by far not as large as expected by the simulations (section 5.4.4). This is basically due to the overestimated flux change with temperature, but the pulse heights are still quite large with a maximum of about $0.23 \Phi_0$ if compared to observations with MMCs.

Following equation 4.3 the total heat capacity can be determined from the pulse heights and the measured $\Phi(T)$ dependence from figure 5.9 and is shown in figure 5.11. Even though the calculated heat capacities scatter quite much the results agree rather well with the simulated values shown in figure 5.5. In average, the measured heat capacity might be about 25% larger than simulated before. This discrepancy might very well be explained by an error in the assumed geometry of the sensor and pickup coil.

Therefore, the theory for the heat capacity of superconducting and of normal conducting regions seem to fit well to the experimental data. A possible conclusion is, that the magnetic field distribution (section 5.4.3) and the determination of normal conducting volume and superconducting volume are in the expected range and the error in the signal height simulations probably due to other reasons.

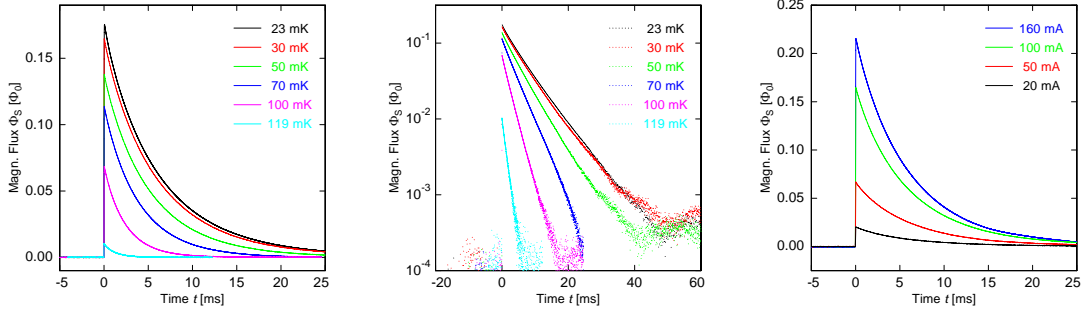


Figure 5.12 Different depictions of pulses of the Hf detector
Left: Pulses with $I = 100$ mA at different temperatures linearly plotted.
Middle: The same in a logarithmic plot.
Right: Pulses at $T = 30$ mK plotted for different currents I .

5.5.4 Signal Shape and Thermal Link

An other characteristic tested was the dependence of the pulse shape on temperature and current in the meander. The qualitative behaviour agrees with the expectation of faster and smaller pulses towards higher temperatures as shown in figure 5.12(left) for a persistent current of $I = 100$ mA. In the plot in the middle of the figure 5.12 the same pulses are plotted on a logarithmic scale. The decay of the pulses seems to be almost linear in this plot meaning that only one decay time can be observed. This in turn means that the detector behaves very similar to the simple calorimeter model introduced in chapter 2.5.1. The figure on the right shows pulses at a temperature of $T = 30$ mK for different currents injected into the meander. Scaled by the maximum of the pulses the time evolution seems to be the same for all of the displayed pulses, as expected if the heat capacity changes only marginal with persistent current in the meander.

To check the similarities to the simple model, the thermal link G to the bath can be determined, as done in chapter 4.5.3 for the Al detector following eq. 4.4. The result is shown in figure 5.13 and has, as expected for a dominating Kapitza resistance, a T^3 dependence with $g_0 = 12 \pm 1 \mu\text{W}/\text{K}^4$, which is very close to the value obtained for the aluminium detector of $g_{0,\text{Al}} = 11.3 \pm 0.2 \mu\text{W}/\text{K}^4$. The T^3 dependence by itself supports the many assumptions made in the thermal model of the detector. This agreement of the prefactor with the one of the MMC with Al absorber is also plausible as the acoustic mismatch between Hf and Si might be very similar to the one between Au:Er and Si.

Now the expected decay time of the detector can be determined following eq. 2.39, $\tau = C/G$, with the experimentally obtained values for heat capacity C and thermal conductivity G leading to figure 5.14. This can be compared to the actually observed time constants obtained by fitting averaged pulses by a single or the sum of two exponential decays (eq. 4.1). By plotting the decay time of the single exponential decay or, in case of the sum of two exponential functions, the decay time corresponding to the by far larger amplitude A_i , figure 5.15 was achieved. As can be seen the exper-

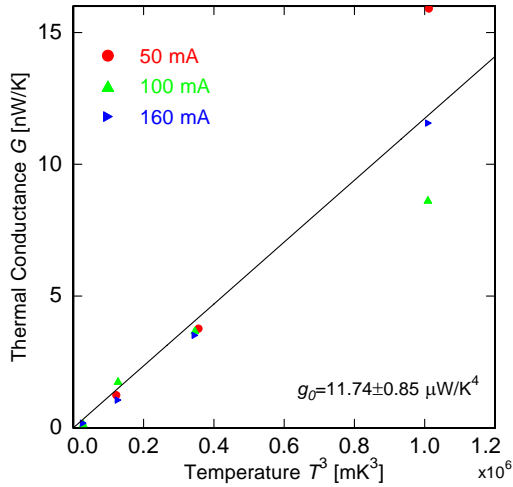


Figure 5.13 The measured thermal conductivity G to the bath for the hafnium detector plotted against T^3 proving the expected T^3 dependency.

experimental values fit well to the expected values showing the same linear temperature dependency. In figure 5.15 only the values for $I_0 = 160$ mA are shown and the decay time of the pulses seems to be independent of the frozen current.

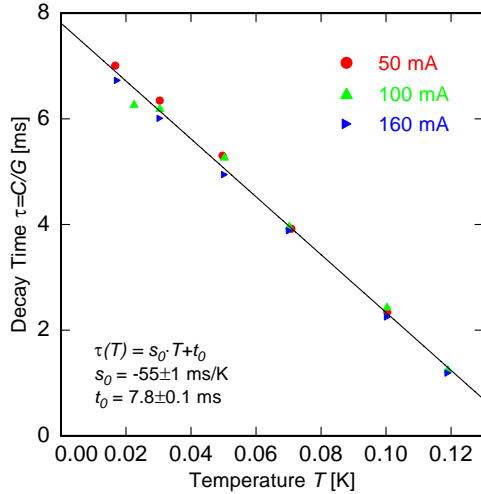


Figure 5.14 The expected values of the decay time following eq. 2.39 with the experimentally determined values for C and G from above. The solid line shows a linear fit with the values written in the graphic.

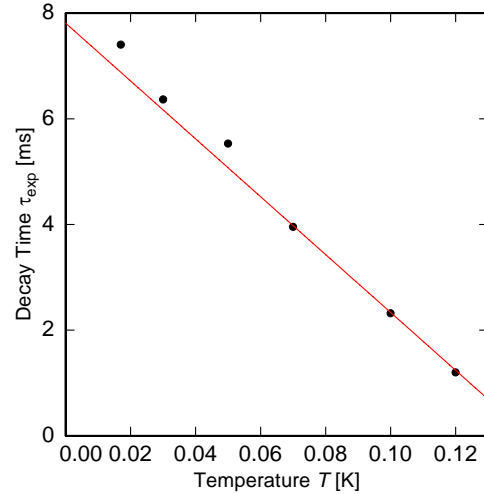


Figure 5.15 The main decay times determined by fitting a single or the sum of two exponential decays. The solid line shows the linear function obtained by a fit to the data of figure 5.14.

5.5.5 Energy resolution

The energy resolution was determined for the Hf detector in a separate measurement with higher statistics as well. The highest achieved injected current of $I_0 = 160$ mA and the base temperature of the cryostat at $T = 17$ mK were chosen for this measurement.

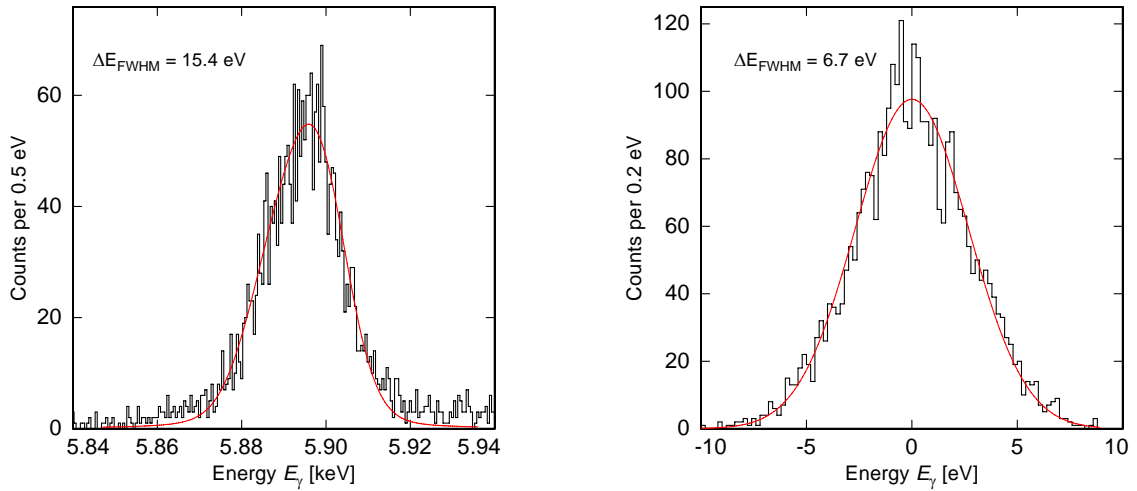


Figure 5.16 Energy spectra obtained with $I_0 = 160$ mA and $T = 17$ mK. **Left:** Spectrum of the K_α line of ^{55}Mn with an energy resolution of $\Delta E_{\text{FWHM}} = 15.4$ eV. **Right:** Energy spectrum at 0 keV photon energy, as derived from untriggered detector signals showing a resolution of $\Delta E_{\text{FWHM}} = 6.7$ eV.

Figure 5.16 shows the measured spectra. For the K_α line of ^{55}Mn an energy resolution of $\Delta E_{\text{FWHM}} = 15.4$ eV were obtained while the distribution of the baselines shows a broadening of $\Delta E_{\text{FWHM}} = 6.7$ eV. The quite big difference between baseline and x-ray events can on the one hand be explained by the reasons earlier given for the Al detector (chapter 4.4) since there is again a superconductor involved. On the other hand the cryostat was at its base temperature and not stabilised to a fixed temperature and therefore showed a temperature variation of about ± 0.5 mK. Such a temperature variation influences the signal height quite strongly because of the changing heat capacity while the baselines are not much influenced by this effect.

The temperature fluctuations of the cryostat were accepted in this measurement as they seemed to be the smaller of two evils, because by disconnecting the stabilisation electronics it was possible to get rid of strong external noise contributions. For clarification, the noise spectrum in figure 5.7 was measured at base temperature with all possible electronics disconnected while figure 5.8(left) was measured with stabilised temperature and shows therefore by far larger noise.

6. Summary and Outlook

During this work two, except for the absorber identical, Metallic Magnetic Calorimeters (MMCs) with superconducting absorber material were built and characterised. The x-ray absorbers of both detectors were about $50 \mu\text{m}$ thick. One absorber was made of high purity aluminium, the other of aluminium doped with about 2000 ppm of manganese, which are both superconducting at the working temperature of about $T = 30 \text{ mK}$. The doping with magnetic impurities has some severe effects on the superconducting properties of the host material. In case of the 2000 ppm of manganese in aluminium, the transition temperature dropped by a factor of four to $T_c \simeq 300 \text{ mK}$ and the energy gap 2Δ is expected to be greatly reduced or even zero.

MMCs consist of a particle absorber to stop particles with a high quantum efficiency and a paramagnetic sensor made of an alloy of gold and a small concentration of the rare earth metal erbium positioned in a weak magnetic field. Therefore the sensor shows a steep change of magnetisation with temperature. The sensor is weakly coupled to the thermal bath and the signal is read out by a low noise flux-to-voltage transducers called SQUIDs. Energy deposited in the absorber and sensor, e.g. by an absorbed x-ray photon, leads to a temperature rise of the calorimeter causing the change of magnetisation of the paramagnetic sensor to change.

Two things were planned to investigate. First, how the different thermalisation behaviour of 5.9 keV x-rays in superconducting Al and Al:Mn is influenced by a smaller absorber thickness in comparison to [Wel08], where absorbers with $500 \mu\text{m}$ thickness, made of the same materials, were used.

The absorption length in Al for the used 5.9 keV x-rays, originating from an ^{55}Fe source, is about $\lambda = 32 \mu\text{m}$ leaving a probability of about 20% for the x-rays to cross the absorber and to be absorbed underneath. If the photons are absorbed in the Au spacer layer underneath the superconducting absorber, the deposited energy is transferred to the superconductor mainly by low energetic thermal phonons and electrons. After absorption in the superconductor all down conversion processes take place in the superconductor which possibly leads to a different thermalisation behaviour. This difference in thermalisation was the second question to be investigated.

Both detectors were characterised at different temperatures and in different magnetic fields and intriguing results were achieved. As expected from the observations in [Wel08] no significant influence by the Mn impurities in Al on the thermalisation processes in superconductors on long time scales were noticed. However, all transport processes were faster than in [Wel08], which can be accounted to the smaller absorber thickness. In fact, rise times just below $0.5 \mu\text{s}$ were observed.

In [Cos93] “missing energy” had been observed in low temperature calorimeters using superconducting absorbers, which was confirmed by the detector with Al absorber. On the contrary this behaviour was not observed with the detector with Al:Mn absorber, leading to the conclusion that this “missing energy” is strongly influenced by the presence of magnetic impurities within a superconductor.

The observed line width of the Al detector was $\Delta E_{\text{FWHM}} = 9.5 \text{ eV}$ for the K_α line of ^{55}Mn at 5.9 keV, which is a little higher than the intrinsic line width of $\Delta E_{\text{FWHM,Base}} = 7.3 \text{ eV}$, which was obtained by the analysis of untriggered detector signals, so-called baselines. While these energy resolutions were obtained by the events absorbed in the superconducting absorber, the line width of the events absorbed in the gold spacer was as good as $\Delta E_{\text{FWHM}} = 7.1 \text{ eV}$ at 5.9 keV and $\Delta E_{\text{FWHM,Base}} = 6.6 \text{ eV}$ for the baseline distribution.

The reached energy resolution and the achieved rise times lead to the conclusion that the application of MMCs with superconducting absorbers for high resolution and high count-rate x-ray spectroscopy will be possible in future detector setups.

During the data analysis of the detector with Al:Mn absorber another unexpected effect was seen. Above about 100 mK the pulses changed direction and grew larger to higher temperatures, reaching pulse heights as high as $\Delta\Phi_S = 0.12 \Phi_0$. This could be explained by the change of magnetic flux in the pick-up coil in the superconducting transition of the superconducting absorber, originating from the expulsion of the magnetic field from the superconductor because of the Meissner effect.

The idea of using this effect to determine the temperature of the micro-calorimeter was later picked up and further examined. A theoretical model to describe such a detector was introduced and a prototype based on this new detector principle was built on a SQUID with integrated meander-shaped pick-up coil (MagCal No. 14) using $25 \mu\text{m}$ thick hafnium as sensor and absorber material.

The model consisted of finite element simulations of the detector geometry and basic properties of type I superconductors. The outcome was quite promising, resulting in pulse heights as high as several flux quanta.

The experimental results of the prototype characterisation damped the enthusiasm a little, since the observations were about a factor of 4-5 smaller than expected from the simulations. However, the pulses were still quite large, compared to MMCs, reaching pulse heights of $\Delta\Phi_S = 0.23 \Phi_0$.

But there were good agreements between model and experiment. The measured heat capacity agrees well with the calculation. The bottom line was that the simulations of the magnetic field distribution within the sensor reproduce the real behaviour quite well, since the distribution has great impact on the heat capacity calculation.

The pulse shape of most of the detector signals was described well by one exponential rise and one decay, which supports a very simple thermodynamic model of this detector type. The decay times for example can be well described by the relation $\tau = C/G$, with the sensor's heat capacity C and the thermal conductance to the bath G . Being the first and non-optimised detector prototype the achieved energy resolution is quite impressive, too. While the instrumental line width at 5.9 keV reached $\Delta E_{\text{FWHM}} = 15.4 \text{ eV}$, an intrinsic energy resolution of $\Delta E_{\text{FWHM}} = 6.7 \text{ eV}$ was achieved for the baselines.

Apart from the disagreements of theoretical model and experimental observations, the new sensor type seems very encouraging. There are already a few starting points, theoretical as well as experimental, to improve the understanding of the device and bring theory and experiment to better consistency.

Bibliography

- [Ban93] S. R. Bandler, C. Enss, R. E. Lanou, H. J. Maris, T. More, F. S. Porter, und G. M. Seidel, Metallic Magnetic Bolometers for Particle Detection, *Journal of Low Temperature Physics*, **93**(3/4), 709–714, 1993.
- [Bar57] J. Bardeen, L. N. Cooper, und J. R. Schrieffer, Theory of Superconductivity, *Physical Review*, **108**(5), 1175–1204, 1957.
- [Bey09] Jörn Beyer, PTB SQUIDs for readout of magnetic microcalorimeters: single detectors and MMC arrays, Talk at the Kirchhoff-Institute for physics, University of Heidelberg, 2009.
- [Ble09] Nadine Bleach, *Characterisation of a Single Pixel Metallic Magnetic Calorimeter for High Energy X-ray Spectroscopy*, Diplomarbeit, Kirchhoff-Institut for physics, University of Heidelberg and Imperial College London, 2009.
- [Boa64] G. Boato, G. Gallinaro, und C. Rizzuto, Effect of Transition Metal Impurities on the Critical Temperature of Nontransition Metals, *Reviews of Modern Physics*, **36**(1), 162–164, 1964.
- [Boa66] G. Boato, G. Gallinaro, und C. Rizzuto, Effect of Transition Metal Impurities on the Critical Temperature of Superconducting Al, Zn, In and Sn, *Physical Review*, **148**(1), 353–361, 1966.
- [Bro28] Robert Brown, A brief account of microscopical observations made in the months of June, July and August, 1827, on the particles contained in the pollen of plants; and on the general existence of active molecules in organic and inorganic bodies, *Phil. Mag.*, **4**, 161–173, 1828.
- [Büh88] M. Bühler und E. Umlauf, A Magnetic Bolometer for Single-Particle Detection, *Europhysics Letters*, **5**(4), 297–301, 1988.
- [Bur04] Andreas Burck, *Entwicklung großflächiger magnetischer Kalorimeter zur energieaufgelösten Detektion von Röntgenquanten und hochenergetischen Teilchen*, Diplomarbeit, Kirchhoff-Institut for physics, University of Heidelberg, 2004.
- [Bur08] Andreas Burck, *Entwicklung großflächiger mikrostrukturierter magnetischer Kalorimeter mit Au:Er- und Ag:Er-Sensoren für den energieaufgelösten Nachweis von Röntgenquanten und hochenergetischen Teilchen*, Dissertation, Kirchhoff-Institut for physics, University of Heidelberg, 2008.

- [Cla04] John Clarke und Alex I. Braginski (Ed.), *The SQUID Handbook: Vol. I Fundamentals and Technology of SQUIDs and SQUID Systems*, Wiley-VCH, 2004.
- [Cos93] E. Cosulich, F. Gatti, und S. Vitale, Further Results on μ -Calorimeters with Superconducting Absorber, *Journal of Low Temperature Physics*, **93**(3/4), 263–268, 1993.
- [Cur03] Pierre Curie und Albert Laborde, Sur le chaleur dégagée spontanément par les sels de radium, *Comptes rendus de l'Academie des Sciences*, **136**, 673–675, 1903.
- [Dan05] Talgat Daniyarov, *Metallische magnetische Kalorimeter zum hochauflösenden Nachweis von Röntgenquanten und hochenergetischen Molekülen*, Dissertation, Kirchhoff-Institut for physics, University of Heidelberg, 2005.
- [Des84] P. D. Desai, T. K. Chu, H. M. James, und C. Y. Ho, Electrical Resistivity of Selected Elements, *Journal of Physical and Chemical Reference Data*, **13**(4), 1069–1096, 1984.
- [Dor08] W.B. Doriese et al., Toward a 256-Pixel Array of Gamma-Ray Microcalorimeters of Nuclear-Materials Analysis, *Journal of Low Temperature Physics*, **151**(3/4), 754–759, 2008.
- [Ens00] C. Enss, A. Fleischmann, K. Horst, J. Schönefeld, J. Sollner, J. S. Adams, Y. H. Huang, Y. H. Kim, und G. M. Seidel, Metallic Magnetic Calorimeters for Particle Detection, *Journal of Low Temperature Physics*, **121**(3/4), 137–176, 2000.
- [Ens05] Christian Enss und Siegfried Hunklinger, *Low-temperature physics*, Springer-Verlag Berlin Heidelberg New York, 2005.
- [Fle03] Andreas Fleischmann, *Magnetische Mikrokalorimeter: Hochauflösende Röntgenspektroskopie mit energiedispersiven Detektoren*, Dissertation, Kirchhoff-Institut for physics, University of Heidelberg, 2003.
- [Fle05] Andreas Fleischmann, Christian Enss, und G. M. Seidel, *Cryogenic Particle Detection*, volume 99 of *Topics in applied physics*, chapter Metallic Magnetic Calorimeters, 151–216, Springer-Verlag Berlin Heidelberg, 2005.
- [Frö50] H. Fröhlich, Theory of the Superconducting State. I. The Ground State at the Absolute Zero of Temperature, *Physical Review*, **79**(5), 845–856, 1950.
- [Gin50] V. L. Ginzburg und L. Landau, On the theory of superconductivity, *Zh. Èksper. Teoret. Fiz.*, **20**, 1064–1082, 1950.

-
- [Hah92] W. Hahn, M. Loewenhaupt, und B. Frick, Crystal field excitations in dilute rare earth noble metal alloys, *Physica B*, **180–181**(1), 176–178, 1992.
- [Hau06] Daniel Haug, *Entwicklung eines magnetischen Kalorimeters zur Neutrinomassenbestimmung aus dem Endpunkt des Beta-Spektrums von ^{187}Re* , Diplomarbeit, Kirchhoff-Institut for physics, University of Heidelberg, 2006.
- [Höh08] Christian Höhn, *Investigation of the Thermalisation in a Metallic Magnetic Calorimeter with a Superconducting Rhenium Absorber*, Diplomarbeit, Kirchhoff-Institut for physics, University of Heidelberg, 2008.
- [Höl97] G. Hölzer, M. Fritsch, M. Deutsch, J. Härtwig, und E. Förster, $K\alpha_{1,2}$ and $K\beta_{1,3}$ x-ray emission lines of the 3d transition metals, *Physical Review A*, **56**(6), 4554–4568, 1997.
- [Hor99] Karsten Horst, *Hochauflösende Röntgenspektroskopie mit kalorimetrischen Tieftemperaturdetektoren basierend auf ^{166}Er -dotiertem Gold*, Diplomarbeit, Kirchhoff-Institut for physics, University of Heidelberg, 1999.
- [Hub96] J. H. Hubbell und S. M. Seltzer, Tables of X-Ray Mass Attenuation Coefficients and Mass Energy-Absorption Coefficients, <http://physics.nist.gov/PhysRefData/XrayMassCoef/>, 1996.
- [Joh28] J. B. Johnson, Thermal Agitation of Electricity in Conductors, *Phys. Rev.*, **32**(1), 97–109, 1928.
- [Jos62] B. D. Josephson, Possible new effects in superconductive tunneling, *Physics Letters*, **1**(7), 251–253, 1962.
- [Kap76] S. B. Kaplan, C. C. Chi, und D. N. Langenberg, Quasiparticle and phonon lifetimes in superconductors, *Physical Review B*, **14**(11), 4854–4873, 1976.
- [Kas56] Tadao Kasuya, A Theory of Metallic Ferro- and Antiferromagnetism on Zener’s Model, *Progress of Theoretical Physics*, **1**, 45–57, 1956.
- [Kir10] Andrea Kirsch, *title unknown (to be published 2010)*, Diplomarbeit, Kirchhoff-Institut for physics, University of Heidelberg, 2010.
- [Koz00a] A. G. Kozorezov, Kinetics of interacting quasiparticles and phonons in non-equilibrium superconductors, *Nuclear Instruments and Methods in Physics Research A*, **444**(1–2), 3–7, 2000.
- [Koz00b] A. G. Kozorezov, A. F. Volkov, J. K. Wigmore, A. Peacock, A. Poelaert, und R. den Hartog, Quasiparticle-phonon downconversion in nonequilibrium superconductors, *Physical Review B*, **61**(17), 11807–11819, 2000.

-
- [Lin07] Markus Linck, *Entwicklung eines metallischen magnetischen Kalorimeters für hochauflösende Röntgenspektroskopie*, Dissertation, Kirchhoff-Institut for physics, University of Heidelberg, 2007.
- [Lon35] F. London und H. London, The Electromagnetic Equations of the Superconductor, *Proceedings of the Royal Society A*, **149**, 71–88, 1935.
- [Max50] Emanuel Maxwell, Isotope Effect in the Superconductivity of Mercury, *Physical Review*, **78**(4), 477, 1950.
- [Mei33] W. Meissner und R. Ochsenfeld, Ein neuer Effekt bei Eintritt der Supraleitfähigkeit, *Naturwissenschaften*, **21**(44), 787–788, 1933.
- [Mon06] A. Monfardini et al., The microcalorimeter arrays for a rhenium experiment (MARE): A next-generation calorimetric neutrino mass experiment, *Nuclear Instruments and Methods in Physics Research A*, **559**(2), 346–348, 2006.
- [Nyq28] H. Nyquist, Thermal Agitation of Electric Charge in Conductors, *Phys. Rev.*, **32**(1), 110–113, 1928.
- [Onn11] H. Kamerlingh Onnes, The Superconductivity of Mercury, *Comm. Phys. Lab. Univ. Leiden*, **122**, **124**, 1911.
- [Pab08] Andreas Pabinger, *Entwicklung eines vollständig mikrostrukturierten magnetischen Kalorimeters für die hochauflösende Röntgenspektroskopie*, Diplomarbeit, Kirchhoff-Institut for physics, University of Heidelberg, 2008.
- [Pie08] Christian Pies, *Entwicklung eines Detektor-Arrays basierend auf magnetischen Kalorimetern für die hochaufgelöste Röntgenspektroskopie an hochgeladenen Ionen*, Diplomarbeit, Kirchhoff-Institut for physics, University of Heidelberg, 2008.
- [Poo95] Charles P. Poole, Jr., Horacia A. Farach, und Richard J. Creswick, *Superconductivity*, Academic Press San Diego New York, 1995.
- [Por07] Jan-Patrick Porst, *Towards MARE: Development of a Metallic Magnetic Calorimeter with Superconducting Rhenium Absorber*, Diplomarbeit, Kirchhoff-Institut for physics, University of Heidelberg, 2007.
- [Rey50] C. A. Reynolds, B. Serin, W. H. Wright, und L. B. Nesbitt, Superconductivity of Isotopes of Mercury, *Physical Review*, **78**(4), 487, 1950.
- [Rud54] M. A. Ruderman und C. Kittel, Indirect Exchange Coupling of Nuclear Magnetic Moments by Conduction Electrons, *Physical Review*, **96**(1), 99–102, 1954.

-
- [Sch00] Jan Schönefeld, *Entwicklung eines mikrostrukturierten magnetischen Tieftemperatur-Kalorimeters zum hochauflösenden Nachweis von einzelnen Röntgenquanten*, Dissertation, Kirchhoff-Institut for physics, University of Heidelberg, 2000.
- [Sch07] Sönke Schäfer, *Development of a Fully Microfabricated Two Pixel Magnetic Calorimeter*, Diplomarbeit, Kirchhoff-Institut for physics, University of Heidelberg, 2007.
- [Sha49] Claude E. Shannon, Communication in the Presence of Noise, *Proceedings of the Institute of Radio Engineers*, **37**(1), 10–21, 1949.
- [Sim35] Franz Simon, Application of Low Temperature Calorimetry to Radioactive Measurements, *Nature*, **135**, 763, 1935.
- [Sta94] C. K. Stahle et al., Delayed Thermalization of X-rays Absorbed in Tin Films Far Below the Superconducting Transition Temperature, *Physica B*, **194–196**, 127–128, 1994.
- [Swa89] E. T. Swartz und R. O. Pohl, Thermal boundary resistance, *Reviews of Modern Physics*, **61**(3), 605–668, 1989.
- [Tao71] L. J. Tao, D. Davidov, R. Orbach, und E. P. Chock, Hyperfine Splitting of Er and Yb Resonances in Au: A Separation between the Atomic and Covalent Contributions to the Exchange Integral, *Physical Review B*, **4**(1), 5–9, 1971.
- [Tes77] Claudia D. Tesche und John Clarke, dc SQUID: Noise and Optimization, *Journal of Low Temperature Physics*, **29**(3/4), 301–331, 1977.
- [Wel08] Richard Weldle, *Untersuchung des Effekts magnetischer Verunreinigungen auf das Thermalisierungsverhalten von supraleitenden Teilchenabsorbieren*, Diplomarbeit, Kirchhoff-Institut for physics, University of Heidelberg, 2008.
- [Win] Mark Winter, WebElements: the periodic table on the web, <http://www.webelements.com>.
- [Yos57] Kei Yosida, Magnetic Properties of Cu-Mn Alloys, *Physical Review*, **106**(5), 893–898, 1957.

Acknowledgments – Danksagung

Es gibt so einige Leute die direkt oder indirekt zum Gelingen dieser Arbeit beigetragen haben, die hier erwähnt werden sollen.

Als erstes soll hier Professor Christian Enss gedankt werden ohne dessen unkomplizierte Art ich wohl nie längere Zeit nach Heidelberg und an das faszinierende Gebiet der Tieftemperaturphysik gelangt wäre.

An zweiter Stelle aber mindestens ebenso wichtig ist Loredana Gastaldo, die immer eine gewisse Faszination an jedem noch so langweilig scheinenden Plot findet und deren Tür jeder Zeit offen steht, sei es für nicht- oder physikalische Fragen. Anerkannt soll auch werden, dass sie trotz eines anderen Philipps in der Endphase Zeit für Diskussionen und das Korrekturlesen dieser Arbeit gefunden hat.

Andreas Fleischmann sei gedankt für sein ständiges Interesse für alles was in der Arbeitsgruppe passiert und allerlei Diskussionen zu denen er mit seinem physikalischen Wissen und seiner Intuition immer konstruktiv beitragen kann. Auch seine Korrekturen zur vorliegenden Arbeit sollen nicht unerwähnt bleiben, die ihn kurz vor Fertigstellung gefühlt genau so viel Zeit gekostet haben, wie mich selbst.

Nun sollen meine Kollegen bei den „Bolos“ oder „Detektoren“ erwähnt werden, mit denen ich das Jahr dieser Diplomarbeit verbracht habe.

Als erstes soll hier Richard Weldle erwähnt werden, dessen gute Vorarbeit und das Aufbauen meiner ersten Detektoren für den Erfolg meiner eigenen Arbeit einen maßgeblichen Beitrag geleistet hat.

Als nächstes seien meine mit-Diplomanden genannt, nämlich Falk von Seggern, mit dem ich von den Einführungen in alles Mögliche (Kryoflüssigkeiten, Chemieraum,...) bis zur Abgabe auf einem Stand war und Andrea Kirsch ohne deren Diskussionen über Gott und die Welt (und gelegentlich auch Detektoren) und ihre etwas andere, doch sehr weibliche, Art es in unserem Büro sicher anders zugegangen wäre. Auch wenn sie in dieser Arbeitsgruppe ihre Master- und nicht Diplomarbeit gemacht hat, zählt auch Nadine Bleach in diesen Kreis.

Wenn ich schon bei unserem Büro bin seien die Doktoranden Sebastian Kempf und Christian Pies erwähnt mit ihren Tipps, ihren Antworten oder einfach ihrer Erfahrung bezüglich Kryostaten, Detektoren, oder was sonst alles zu Problemen führen kann, immer eine Hilfe waren. Gleiches gilt auch für die weiteren Doktoranden Jan-Patrick Porst, Sönke Schäfer und den ewigen „HiWi“ Andreas Pabinger.

Gedankt sei auch den „Gläsern“, mit denen ich die Zeit zwar weniger auf physikalische Art und Weise verbracht habe, aber sie doch immer genießen konnte. Sei es vor allem auf der DPG-Tagung oder während unserer täglichen Kaffeepause. Namentlich sind dies Masoomeh Bazrafshan, David Dähn, Gudrun Fickenscher, Tobit Gamp, Angela Halfar, Marius Hempel, Gernot Kasper, Daniel Rothfuß, Manfred von Schickfus und Jens Schindele. Unter anderem auch zu den Gläsern gehörend ist Andreas Reiser, der seinem guten physikalischen auch ein enormes technisches Verständnis, auch im Bereich der Kryotechnik, mit bringt und mit Rudi Eitel zusammen immer für ausreichend flüssiges Helium sorgt. Auch dafür sei gedankt.

Mein Dank gilt auch der Brigitte und Manfred Rehner Förder-Stiftung und im speziellen Professor Manfred Rehner, die durch ihre bereitwillige Unterstützung einen entscheidenden Beitrag zur sorgenfreien Durchführung dieser Arbeit geleistet haben.

„Last, but not least“, wie es so schön immer heißt, möchte ich auch meiner Familie danken. Zum einen danke ich meinem Bruder, Frederick Ranitzsch, der auch nicht unwesentlich zu meinem Ortswechsel nach Heidelberg beigetragen hat und mich durch seine Art das ein oder andere Mal aus einem Motivationsloch während des Studiums heraus holen konnte. Als nächstes möchte ich auch meinem Vater, Karl Heinz Ranitzsch, danken, der durch sein enormes Wissen, auch der Physik, immer für eine Diskussion zu haben ist und neben ständigen Anregungen auch durch eine Korrektur dieser Arbeit beigetragen hat. Ein großer Dank gilt auch meiner Mutter, Ok-Su Ranitzsch, die durch ihre fürsorgliche Art und ihre Anrufe immer wieder für etwas Ruhe in die zum Teil hektischen Arbeitsphasen gesorgt und mich so auf den Boden der Tatsachen zurück gebracht hat.